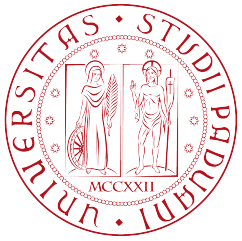

Università degli studi di Padova

Dipartimento di Fisica e Astronomia

Corso di Laurea Magistrale in Fisica

Tesi di Laurea Magistrale

Study of direct reaction channels for the system ^{7}Be+^{208}Pb at Coulomb barrier energies

Relatore

Dott. Marco Mazzocco

Correlatore

Dott. Emanuele Strano

Controrelatore

Prof. Santo Lunardi

Laureando

Claudio Stefanini

Anno Accademico 2014/2015

Alla mia famiglia,
ai miei compagni di viaggio,
grazie per la vicinanza e la pazienza!

To my family,
to my fellow travelers,
thanks for beeing close and patient!

Contents

Introduction

In this thesis work, we studied for the first time the reaction ^{7}Be+^{208}Pb at Coulomb barrier energies.

^{7}Be is an unstable isotope ($T_{1/2} = 53.24\ d$) belonging to the large class of *Radioactive Ion Beams* (RIBs) that acquired more and more interest in recent years in the study of nuclear structure phenomena and possibly new reaction mechanisms and decay modes in regions of the nuclide chart far from the valley of β-stability.

Weakly bound isotopes, sometimes called "exotic nuclei", are unstable nuclear systems with large neutron or proton excess and, consequently ,very low binding energies, so that they are close to the particle emission thresholds. Due to their peculiar structures, exotic nuclei might have extremely different properties from those reported for nuclei along the valley of stability and, therefore, reactions involving such nuclei are expected to behave differently from well-bound nuclei, especially at Coulomb barrier energies. In this energy range, the most relevant process, besides the scattering, is the fusion of the two colliding nuclei. In reactions with loosely bound nuclei, besides the projectile or target inelastic excitations, some new degrees of freedom come into the play:

- *halo structure*: rarified nuclear matter surrounding an internal core; this implies an r.m.s. radius larger than what obtained from the systematics of stable nuclei and a longer exponential tail of matter distribution (see Fig. 1, left panel);
- *neutron skin structure*: proton and neutron have different spatial distributions; the last neutrons are mostly orbiting in the outer part of the nucleus in a skin-like structure (see Fig. 1, right panel);
- *weak binding energy*: typical separation energies of the last nucleons ($< 1.0\ MeV$) well below the binding energies for nuclei close to stability valley; typical binding energies are about one order of magnitude smaller than for nuclei close to the stability valley.

All these phenomena are not independent from each other and might generate opposite and even conflicting effects, as we will see.

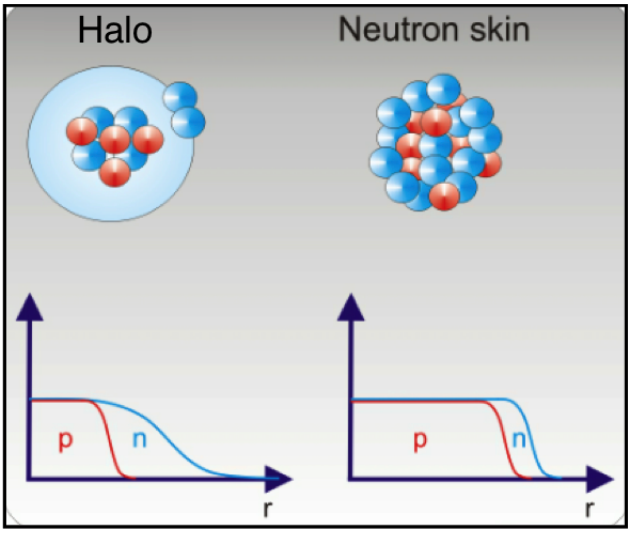

Figure 1: Schematic description of two nuclei exhibiting a halo (left) and neutron skin (right) structure. Figure taken from [5].

Despite the efforts carried out so far, the understanding of nuclear reaction mechanisms in collisions involving exotic and weakly bound nuclei is still a very challenging task. In order to perform an experiment with radioactive projectiles, a primary nuclear reaction is necessary to produce them and a high efficiency beam transport system is needed to separate the selected ions from spurious reaction products and to focus them on a secondary target. Therefore measurements performed with nowadays RIBs typically suffer of limited statistical accuracy.

In the last decade the EXOTIC collaboration of the Laboratori Nazionali di Legnaro (LNL) of the Istituto Nazionale di Fisica Nucleare (INFN) studied the elastic scattering process and the (inclusive) α-particle production cross section for the system ^{9}Be ($S_n = 1.665\ MeV$) + ^{209}Bi in the energy range $40 - 48\ MeV$. The fusion and elastic scattering processes for the reaction ^{11}Be ($S_n = 0.504\ MeV$) + ^{209}Bi were subsequently measured in a series of experiments performed at RIKEN in the years 1996-2004. The ^{9}Be and ^{11}Be breakup processes both involve the emission of a loosely-bound neutron, which is rather difficult to be detected with high efficiency. Thus for both systems, whenever a complete kinematics reconstruction of the breakup events is needed, a critical piece of information is often missing.

More recently the focus has been moved towards the study the reaction dynamics induced by ^{7}Be ($S_\alpha = 1.586\ MeV$). The first ^{7}Be-induced reaction dynamics at Coulomb barrier energies has been investigated for the system ^{7}Be+^{58}Ni [10]. This projectile has a well pronounced ^{3}He + ^{4}He cluster structure and represents, among all light nuclei, the cleanest case where the breakup/transfer interplay in the reaction dynamics can be investigated in detail. In fact, the two ^{7}Be inner clusters are very stable fragments with similar masses, while all breakup studies previously performed always involved the complicated and low-efficiency detection of neutrons (like in the case of the ^{6}He and ^{9,11}Be breakup processes), the emission of a weakly-bound fragment (e.g., the deuteron emission in the ^{6}Li breakup), the emission of a radioactive fragment (as for the triton emission in the ^{7}Li breakup) or a very small breakup probability, as in the case of the ^{17}F breakup process into ^{16}O + p.

For the reaction ^{7}Be+^{208}Pb that we analyze here, the ^{7}Be secondary beam was produced with

the facility EXOTIC [2], by using a high intensity ^{7}Li ($150 - 200$ pnA) primary beam delivered from the LNL-XTU Tandem accelerator impinging on a gas target, which consists of a $5 - cm$ long gas cell doubly walled with $2.2 - \mu m$ thick Havar foils. The cell was filled with H_2 gas up to a pressure of about 1 bar at cryogenic temperature (90 K), which corresponds to an H target density of about 1.35 mg/cm^2. The ^{7}Be secondary beam was separated from the ^{7}Li scattered beam and from other contaminations by means of a 30°-bending magnet, a Wien Filter and adequate slit sets and collimation systems located at suitable positions along the beam-line.

The target of ^{208}Pb was chosen to maximize the effect of the Coulomb field and because it is a doubly magic isotope and so particularly stable. Therefore its excitation is very unlikely and we will not have to take into account the proliferation of energy levels with different angular momenta.

The thesis is organized as follows:

- Chapter 1 provides a general overview of the scientific motivation and the physical case involved;
- Chapter 2 describes the facility EXOTIC at LNL-INFN: the production target, the beam line, the ion optical elements, the beam diagnostic, the secondary ^{7}Be beam production technique and the optimization of the magnets and of the slits;
- Chapter 3 describes the high granularity and large solid angle detection array EXPADES [1]: the design and the ΔE and E_{res} readout electronics;
- Chapter 4 presents the kinematics of 2-body reactions: the elastic, inelastic and transfer cases and the dependencies of the energies with respect to the detection angles for the reaction we are investigating;
- Chapter 5 presents the data analysis. We explain how we calibrated the spectra and how we applied the selection gates to the original data in order to remove non-physical events. First we analyze the ΔE stage and then we consider also the E_{res} stage. Finally, we show how to identify the isotopes using the ΔE-E_{res} technique and the angular distributions for ^{7}Be, ^{3}He and ^{4}He;
- Chapter 6 presents some theoretical analysis with the optical model and a comparison of the reaction cross sections obtained for our system with other similar ones;
- In Chapter 7 we summarize the work and we draw some conclusions.

Chapter 1

Scientific motivation

The reason why nowadays Nuclear Physics, and Nuclear Astrophysics in particular, is largely interested in the study of the properties of nuclei far from stability and on the reaction mechanisms that these exotic nuclei can induce, can easily be understood by taking a quick look at the nuclide chart, which shows on a grid of proton number versus neutron number the distribution of the stable nuclei (half-lives longer than 10^9 years, black squares in Fig. 1.1) and the presently known radioactive nuclides.

The existence of an atomic nucleus is firstly related to the binding energy of the specific system of protons and neutrons. The binding energy B is defined as the difference in mass energy between a nucleus ${}^{A}_{Z}X_N$ and its constituents Z protons and N neutrons and can be written by using atomic masses (given in atomic mass units) as:

$$B = [Zm_p + Nm_n - m({}^{A}X)]c^2$$

with m_p the proton mass and m_n the mass of neutron and $A = N + Z$. Next to the binding energy which is a measure of how much energy has been gained through the strong force by forming the nucleus out of its bare constituents, one also has to consider particle and cluster binding energies of which the neutron and proton binding energies are the most important for delineating the limits of nuclear existence. The neutron (proton) binding energy B_n (B_p) (sometimes called separation energy) is the amount of energy needed to remove the last neutron (proton) from the specific nucleus. Negative binding energy means that the particle is energetically not bound anymore by the nucleus. However, Coulomb barriers (in case of charged particles), centrifugal barriers, and nuclear structure incompatibilities could hold the particle or cluster of particles in the nucleus for a longer time than a typical orbit time of the nucleons in a nucleus ($\sim 10^{-21}$ s).

The total number of stable nuclei sums up to 198. In case we consider as stable also metastable nuclei, i.e. those radioactive nuclei with half-lives comparable to the age of our planet, we do not exceed an overall sum of 284 nuclei. On the other hand, our knowledge of radioactive nuclei presently accounts for more than 3600 species, but the combinations of proton and neutrons of postulated existence within the boundaries of the proton and neutron drip lines (see Fig. 1.1) and the limits imposed to the existence of super-heavy systems, are more than 6000.

Thus the study of stable nuclei exhausts only one twentieth of the whole nuclear panorama. Moreover, the paths of the astrophysical nucleosynthesis $r-$ and $rp-$processes essentially involve unstable

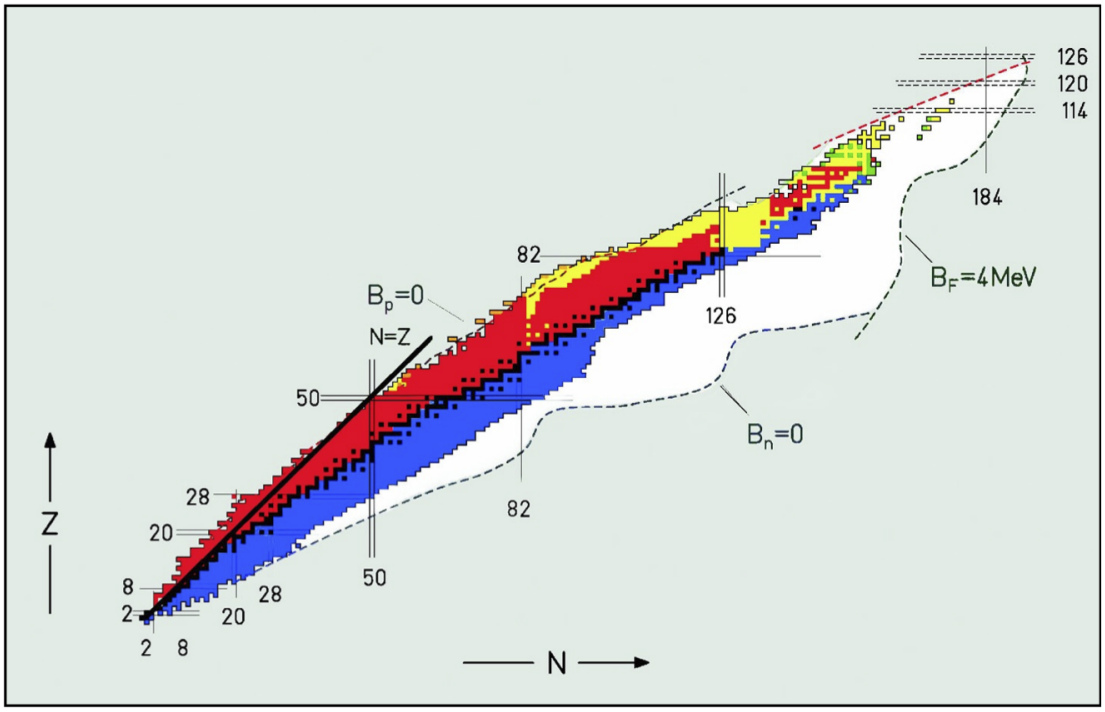

Figure 1.1: Chart of nuclides. The figure shows the decay modes with different colors: β^- decay is blue, β^+ decay is red, α decay is yellow and spontaneous fission is green. $B_p = 0$ and $B_n = 0$ are the proton and neutron drip-lines and B_F is the fission barrier of 4 MeV. Figure taken from [5].

nuclei. The measurements of masses, binding energies, life-times and reaction Q-values are fundamental pieces of information to predict the actual paths of these processes and the abundance of heavier elements. Therefore, present-day major worldwide projects in Nuclear Physics are devoted to the construction of large-scale Radioactive Ion Beams factories.

As we said in the introduction, for the interaction dynamics at energies around the Coulomb barrier of light RIBs there are some new features, absent with nearly all stable beams, that have to be taken into account. Typical binding energies range from 0.1 to 0.5 MeV, much smaller than the 8 MeV average nucleon separation energy for heavier nuclei close to the valley of stability.

The weakly bound valence nucleons may give rise to a halo structure as direct consequence (see Fig. 1.2) which leads the r.m.s. radius to be larger than what established for most of the stable nuclei by the well-known formula $R = r_0 A^{1/3}$ ($r_0 \sim 1.2\ fm$) and a longer exponential tail of matter distribution. A radius larger than the systematics might reduce the Coulomb barrier height and consequently increase the fusion probability. On the other side, a small binding energy could remove flux from the fusion channel, since the projectile could more easily break before the fusion process can take place.

The question whether the low binding energies of the valence nucleons as well as the halo properties of many of these nuclei could enhance or hinder the fusion probability has triggered quite some effort both from a theoretical and an experimental point-of-view. Despite early measurements, it is now rather clear that breakup related effects mainly enhance the reaction probability rather than the fusion cross section, especially in the sub-barrier energy regime. Several review papers have been recently published on this subject [11, 12, 13, 14].

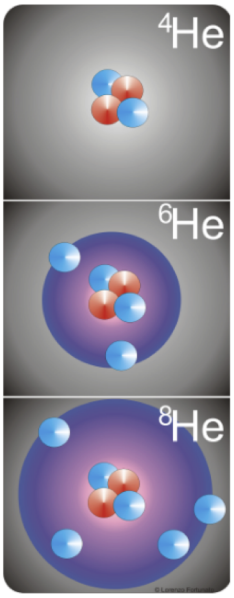

Figure 1.2: Example of nuclei with halo structure. Figure taken from [5].

The key question has now moved toward understanding in detail which process (inelastic scattering, transfer reactions or breakup process) is mainly responsible for the enhancement of the reaction cross section at Coulomb barrier energies. For instance, in a series of experiments performed at Notre-Dame in the first half of the last decade, it was found that for the system ^{6}He + ^{209}Bi at 21.5 MeV, the contribution of the 2n-transfer was $\sim$ 55% [15], that of the 1n-transfer ca. 20% [16] and about 25% of the enhancement was due to the breakup process ^{6}He $\rightarrow$ ^{4}He + 2n [17]. Similar results were obtained in the experiments carried out at GANIL for the systems ^{6}He + ^{63}Cu [18, 19] and ^{6}He + ^{197}Au [20]. Thus it is rather well-established that for the weakly-bound 2n-halo ^{6}He (S_{2n} = 0.972 MeV), the reaction cross section enhancement at near-barrier energies is mainly triggered by the 2n-transfer process.

More recently, new experimental data were published for the reaction dynamics induced by the 1p-halo ^{8}B (S_p = 0.1375 MeV) [21, 22] and by the 1n-halo ^{11}Be (S_n = 0.504 MeV) [23, 24]. In both cases, reaction cross sections up to a factor 2 larger than those observed for reactions induced by the corresponding stable (more bound) isotopes were observed. A tentative analysis indicates the breakup channel as the main responsible for the enhancement of the reaction probability for ^{8}B, while the origin of the large amount of ^{10}Be observed for the system ^{11}Be + ^{64}Zn is still under evaluation. If this scenario is confirmed, n-rich nuclei and p-rich nuclei would show different behaviors, with the predominance of transfer channels for the former and of the breakup process for the latter.

Among all light ions, we selected the radioactive and weakly-bound ^{7}Be as subject of our investigation. ^{7}Be has a quite low particle emission threshold ($S_\alpha = 1.586\ MeV$) and a very well pronounced ^{3}He–^{4}He cluster structure. Thus, while approaching a target nucleus, ^{7}Be has a large probability either to breakup into its constituent clusters or to transfer one of them to the target. The fact that two ^{7}Be clusters, i.e. ^{3}He and ^{4}He, are stable, well-bound, and have similar masses greatly simplifies life to experimentalists, since the same technique can be adopted for the simultaneous and unambiguous detection of both of them.

So far, the ^{7}Be-induced reaction dynamics at Coulomb barrier energies has been investigated

for the systems ^{7}Be+^{238}U [25] and ^{7}Be+^{58}Ni [21]. In the former reaction, the fusion–fission and transfer/breakup–fission cross sections were measured at five different bombarding energies. In the latter system, the scattering process was measured and the total reaction cross section extracted for five beam energies. Our experiment was able for the first time to unambiguously detect (and distinguish) ^{3}He and ^{4}He reaction products for the system ^{7}Be+^{58}Ni, providing new insights into the ^{7}Be-induced reaction dynamics at near-barrier energies.

Chapter 2

The facility EXOTIC

Experiments performed with light RIBs suffer of low statistics and while producing them, we have to fight against several technical and physical obstacles, especially against the weak interaction, which lets radioactive nuclei slide down along isobaric chains towards the bottom of the β-stability valley. The battle becomes stronger and stronger as we move apart from the stability line, since the β-decay half-lives get shorter and shorter.
Therefore, in a rather general RIB production scheme, we need to consider the following prescriptions:

- the production should be fast, due to the very short half-lives of the nuclear species under production;
- the chosen reaction mechanism should warranty the largest possible production cross section, by optimizing projectile-target combination, bombarding energy, primary beam intensity, power dissipation into the target;
- the production should be selective, because the contaminations might be several orders of magnitude larger than the nuclear species of interest.

The facility EXOTIC, developed at the INFN-LNL, provides the In-Flight production of light weakly-bound RIBs; it was commissioned in 2004 and the first beam for experiment was delivered in February 2006. The production mechanism employs inverse kinematics reactions induced by heavy ion beams delivered by the LNL-XTU Tandem accelerator on light gas targets.

The main features of the In-Flight separation are the following:

- the reaction products, i.e. the RIBs under production, are kinematically focused, due to linear momentum conservation, at small polar angles around the primary beam direction;
- the separation time from the primary beam and other possible contaminant reaction products is rather fast, in the order of a few μs, and independent of the chemical properties of the RIB under production;
- the RIBs retain a quite large fraction of the projectile initial velocity, therefore there is essentially no need of a further (expensive) re-acceleration stage;

- the RIB selection is carried out by proper combinations of magnetic and (sometimes) electrostatic fields and atomic interaction;
- the target station dissipates only a small fraction of the primary beam power;
- all ion-optical elements, especially those closer to the target station or to the places where the primary beam is stopped, are designed to properly work in a high radiation environment.

The In-Flight separation method used here employs inverse kinematics reactions, i.e. high intensity ($100 - 150\ pnA$) heavy ion beams impinging on light targets, such as for instance inverse (p,n), (d,n), (^{3}He,n) processes, preferably with negative Q-values. Reaction products are generally emitted in cones around the primary beam direction with narrow opening angles ($\theta_{lab} < 10°$) in the laboratory frame. Hydrogen and helium are the preferred target materials. Unfortunately there do not exist helium compounds, while hydrogen rich compounds, e.g. CH_2, cannot withstand the thermal stress induced by a very intense heavy ion primary beam. To circumvent these problems, gas targets with entrance and exit metal windows are used.

2.1 Production target

The production target is a 50 mm long double walled cylindrical cell with a 25 mm inner diameter. The entrance and exit windows consist of 2.2 μm thick Havar foils with a diameter of 14 and 16 mm, respectively. The cell volume can be filled with H_2, D_2, ^{3}He and ^{4}He gases.

Windows were tested up to an internal pressure of 1.4 bar and are standardly operated in experiments at up to $\sim 1.2\ bar$. The target station can be used either at room temperature or cooled down to liquid nitrogen temperature. The cooling procedure helps to improve the life-time of the windows and provides a higher density target for the same operational pressure.

The gain in secondary beam intensity at the EXOTIC final focal plane between the target operation at cryogenic ($\sim 90\ K$) and at room ($\sim 300\ K$) temperature is about 2.7. This value is slightly lower than the ratio between the two temperatures, due to the higher energy loss and angular straggling in the thicker target. The gas temperature is stable (within $\pm 1°$) during standard operation at cryogenic temperature. Small fluctuations (up to $+7°$) are observed while refilling the 100 l liquid nitrogen dewar. The overall dewar refilling procedure normally lasts 5 h, while the nitrogen consumption is about 12 l/h.

2.2 Beam line design

The beam line has been designed aiming at (i) a large solid angle acceptance and (ii) a high selectivity and purity of the secondary beam. A large secondary beam acceptance was achieved by placing the first quadrupole triplet very close ($\sim 200\ mm$ downstream) to the production target and using a beam pipe opening of 160 mm diameter. A high suppression capability of the unwanted nuclear species (scattered and spurious beams) has been reached by means of a 30°-bending dipole magnet (DM) and a Wien Filter (WF) combined with an adequate slits system.

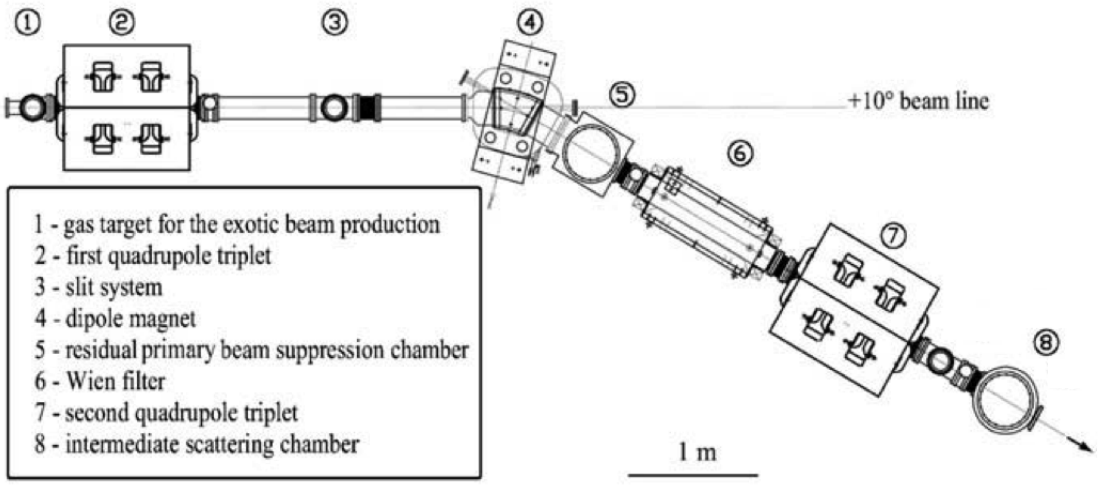

Figure 2.1: Layout of the EXOTIC beam line.

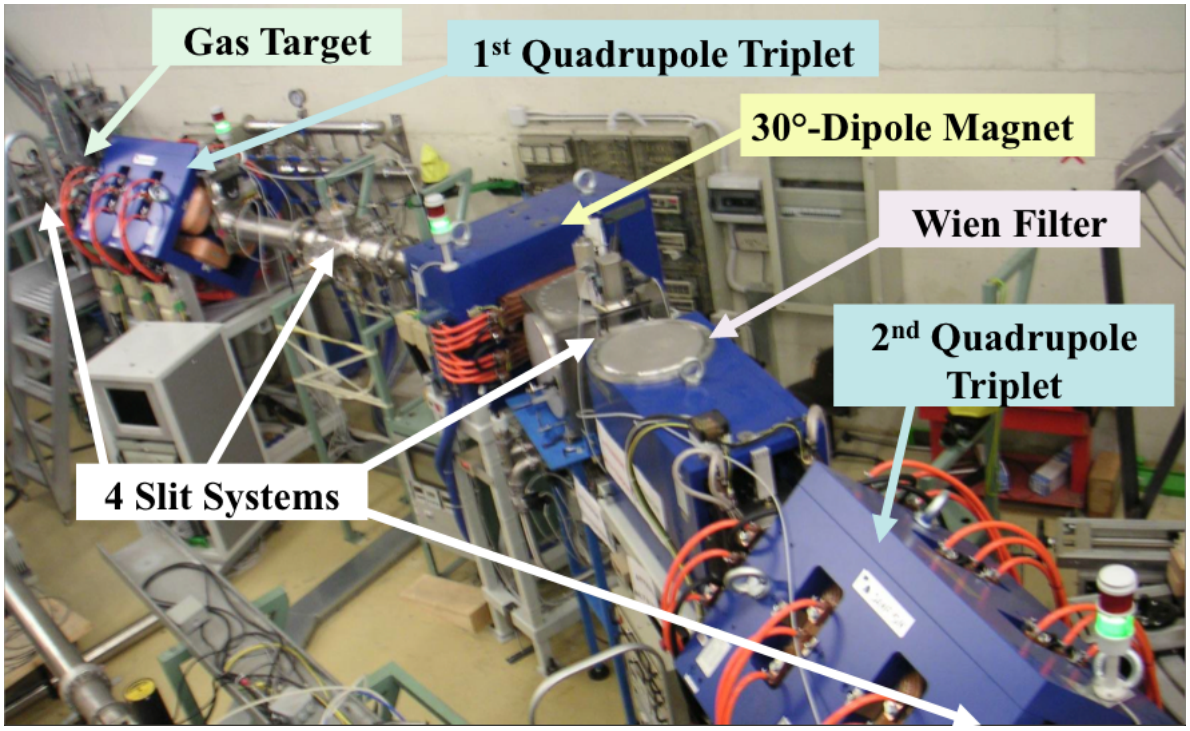

Figure 2.2: Picture of the EXOTIC beam line with its main elements.

The beam line, schematically drawn in Fig. 2.1, has an horizontal acceptance $\Delta\theta = \pm 50\ mrad$, a vertical acceptance $\Delta\phi = \pm 65\ mrad$, a solid angle coverage $\Delta\Omega = \pm 10\ msr$, a momentum acceptance $\Delta p/p = \pm 5\%$, an energy acceptance $\Delta E/E = \pm 10\%$ and a maximum magnetic rigidity $B\rho = 0.98\ Tm$. The beam line consists of the following elements:

1. S0 entrance four-jaw slit and gas target (standard opening: $\pm 1.5\ mm\ (x) \times \pm 1.5\ mm\ (y)$);
2. Q1, Q2, and Q3 first quadrupole triplet:
   –maximum field gradient $g = 7.5\ T/m$;
   –maximum field at the pole tip $B_0 = 0.6\ T$;
   –effective length $l_{eff} = 0.3\ m$;
   –aperture diameter $d = 0.16\ m$;
3. S1 intermediate four-jaw slit (standard opening: $\pm 50\ mm\ (x) \times \pm 20\ mm\ (y)$);
4. dipole magnet (DM):
   –maximum field $B = 1.4\ T$;
   –bending radius $\rho_0 = 0.7\ m$;
   –bending angle $\Phi = 30°$;
   –entrance angle $\epsilon_1 = 0°$;
   –exit angle $\epsilon_2 = 0°$;
   –pole gap $d = 0.07\ m$;
   –pole width $W = 0.294\ m$;
5. F1 intermediate focal plane and S2 slit system (standard opening: $\pm 5.0\ mm\ (x) \times \pm 12.5\ mm\ (y)$);
6. Wien filter (WF):
   –maximum magnetic field $B = 0.08\ T$;
   –effective magnetic field length $l_m = 1.0\ m$;
   –pole gap $d_m = 0.2\ m$;
   –pole width $W_m = 0.4\ m$;
   –maximum electrical field $E = 20\ kV/cm$;
   –maximum voltage $V = \pm 50\ kV$;
   –effective electric field length $l_e = 1.0\ m$;
   –electrode gap $d_e = 0.05\ m$;
   –electrode width $W_e = 0.15\ m$;
7. Q4, Q5, and Q6 second quadrupole triplet with the same characteristics as the first triplet.
8. Fourth slit system at the exit of the quadrupole Q6 (standard opening: $\pm 1.5\ mm$) and F2 final focal plane and reaction target.

2.3 Ion optics

The EXOTIC beam-line consists of eight ion-optical elements. After a first slit system S0 located $\sim 200\ mm$ upstream the production target in order to define the primary beam spot size, we have the

first quadrupole triplet (Q1–Q3). A second slit S1, $\sim 1\ m$ upstream the bending magnet prevents the particles from striking on the magnet walls. Then there is a 30°-dipole magnet (DM) which operates the selection in magnetic rigidity ($B\rho = \pm 5\%$) and suppresses the primary beam with the help of the slit S2, placed downstream the dipole magnet. Then there is the Wien filter which operates the selection in velocity and a second quadrupole triplet (Q4–Q6) is eventually employed to focus the RIB on the secondary target. The slit S3, at the exit of the second quadrupole triplet, stops the particles deflected from the Wien filter.

The setting values of the magnetic fields of the ion optical elements of EXOTIC are calculated with the program GICOSY [26]. The quadrupole triples are set in a configuration where the first and the third quadrupoles (Q1/Q3 and Q4/Q6) focus on the x-axis and the middle quadrupoles (Q2 and Q5) focus on the y-axis. The are three focal planes along the facility: the first one on the gas production target (provided by the accelerator), one on the slit S2 and at the very end of the facility, where the experiments take place. After a first estimate of the values with GICOSY, a more precise fine tuning is required at the beginning of each experiment to achieve the maximum transmission of the beam.

2.4 Beam diagnostics

The beam diagnostics is done by means of a monitor detector (surface barrier silicon detector) placed at final focal plane position and mounted on the target ladder. This detector has a thickness of 100 μm. It is used to measure the energy of the RIB under production which, combined to the magnetic rigidity filter of the dipole magnet, can provide a hint of the atomic number Z of the different produced nuclear species. There is also the possibility to use a telescope of silicon detectors ΔE $(10 - 30\ \mu m) - E_{res}$ $(100\ \mu m)$ for more complicated beams or to verify the contamination of the secondary beam.

Since a silicon detector cannot sustain a rate much larger than 10^3 *pps* for long periods, two 12% transparency grids were installed between the negative source and the entrance of the Tandem, that lower the rate of the beam by a factor ~ 80. A beam tracking system consisting of two $x \times y$ position sensitive Parallel Plate Avalanche Counters (PPACs) has been used (see Fig. 2.3).

The PPACs are installed along the beam line 909 mm and 365 mm upstream the secondary target. Each detector consists of a cathode plate between two anodes. Each anode is made up by 60 parallel wires at a distance of 1 mm from each other. The wires of the two anodes are oriented perpendicularly to each other, to achieve a 1.0 mm $(x) \times 1.0$ mm (y) position resolution. The cathode consists of a 1.5 μm thick Mylar foils with 30 nm of aluminum evaporated on each surface. The distance between the cathode and each anode is 1.9 mm and this gap is routinely filled with isobutane (C_4H_{10}) at a pressure of 20 $mbar$. The detector entrance and exit windows are made by 1.5 μm Mylar foils. The overall PPAC thickness, measured with α particles emitted from standard calibration sources, is about 7.7 μm Mylar equivalent. The cathodes of the PPACs are powered with a tension of $-865\ V$. The maximum counting rate sustainable by the detector is $\sim 3 \times 10^5$ *pps*. The efficiency varies with the atomic number of the incoming particles. Efficiencies up to 99% were observed for oxygen and fluorine isotopes and of about 90% for beryllium and boron isotopes. An overall position resolution of about 1.3 mm was obtained for the event-by-event position reconstruction provided by the two PPACs.

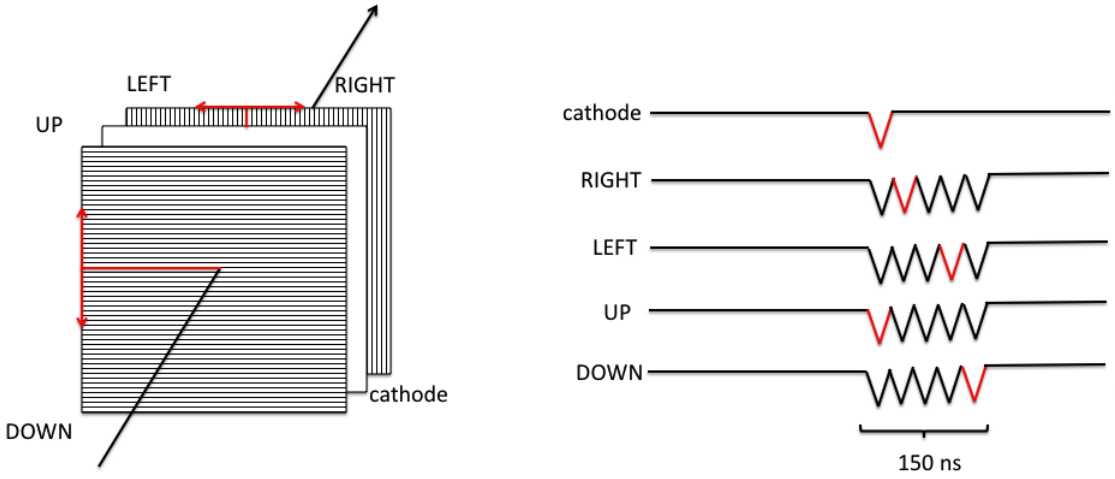

Figure 2.3: The working principle of a PPAC: when a particle crosses the detector electric signals are collected from the cathode and through horizontal and vertical wires by each end of the delay-line of the two anodes (UP, DOWN, LEFT and RIGHT, also known as y_1, y_2, x_1, x_2). The x and y positions are reconstructed by the time difference LEFT-RIGHT and UP-DOWN respectively.

2.5 ^{7}Be beam production

In this section we will describe how the production of the ^{7}Be beam was performed. We used a primary beam of $^7Li^{3+}$ coming from from the XTU-Tandem with an energy of 48.8 MeV, achieved by setting the accelerator to a voltage of 12.1 MV. The gas target was $^1H_2$ at a pressure of 1 bar and a temperature of 90 K.

The reaction used to obtain the secondary beam of ^{7}Be is

$$^7Li + ^1H \rightarrow ^7Be + n \tag{2.1}$$

2.5.1 Initial conditions

The initial conditions, i.e. the magnetic field at the pole-tips of the of the Q1-Q6 quadrupoles and of the dipole magnet (DM), are reported in Table 2.1. The Wien filter (WF) at this stage was still turned off.

The openings of the slits and the vacuum conditions were the following:

- S0: $\pm 1.5\ mm$, $6.8 \cdot 10^{-7}\ mbar$
- S1: $x = \pm 50\ mm$, $y = \pm 20\ mm$, $2.0 \cdot 10^{-6}\ mbar$
- S2: $x = \pm 5\ mm$, $y = \pm 12.5\ mm$, $2.8 \cdot 10^{5}\ mbar$
- S3: $x = \pm 20\ mm$, $5.2 \cdot 10^{-6}\ mbar$

The dipole magnet (DM) separates the particles with different magnetic rigidity $B\rho$ (where ρ is the curvature radius): equaling the Lorentz force F_L and the centrifugal force F_C we get

$$\vec{F_L} = q\vec{v} \times \vec{B} = m\frac{v^2}{\rho}\hat{u} = \vec{F_C}$$

	magnetic field (mT)
Q1	+339.70
Q2	-646.00
Q3	+384.00
DM	-888.98
WF	0
Q4	+335.80
Q5	-582.10
Q6	+355.80

Table 2.1: Initial values of the magnetic fields (mT) of the optical elements. The Wien filter was turned off.

$$F_L = qvB = m\frac{v^2}{\rho} = F_C$$
$$qB = m\frac{v}{\rho}$$
$$B\rho = m\frac{v}{q}$$

Fig. 2.4 and Table 2.2 show energy spectrum acquired by the monitor detector in this configuration. We can distinguish, from left to right, $^7Be^{2+}$, $^7Li^{2+}$, $^7Be^{3+}$, $^7Li^{3+}$, $^7Be^{4+}$. The first two couples of isotopes have approximately the same mass and the same charge but, since they reach the monitor detector after crossing two PPACs and being the energy loss (as we will see at the beginning of chapter 5) proportional to the square of the ion atomic charge (Z^2), Be isotopes ($Z = 4$) lose more energy in the PPACs than the Li ones ($Z = 3$).

	centroid (channel)	counts	purity
$^7Be^{4+}$	1863.3	36618	14.8%
$^7Li^{3+}$	996.2	207944	83.9%
$^7Be^{3+}$	809.1	1499	0.6%
$^7Li^{2+}$	449.6	1367	0.6%
$^7Be^{2+}$	307.9	319	0.1%

Table 2.2: Analysis of peaks displayed in Fig. 2.4. For every isotope we reported the centroid of the curve, the number of events and the purity defined as the percentage of these events with respect to the total event number.

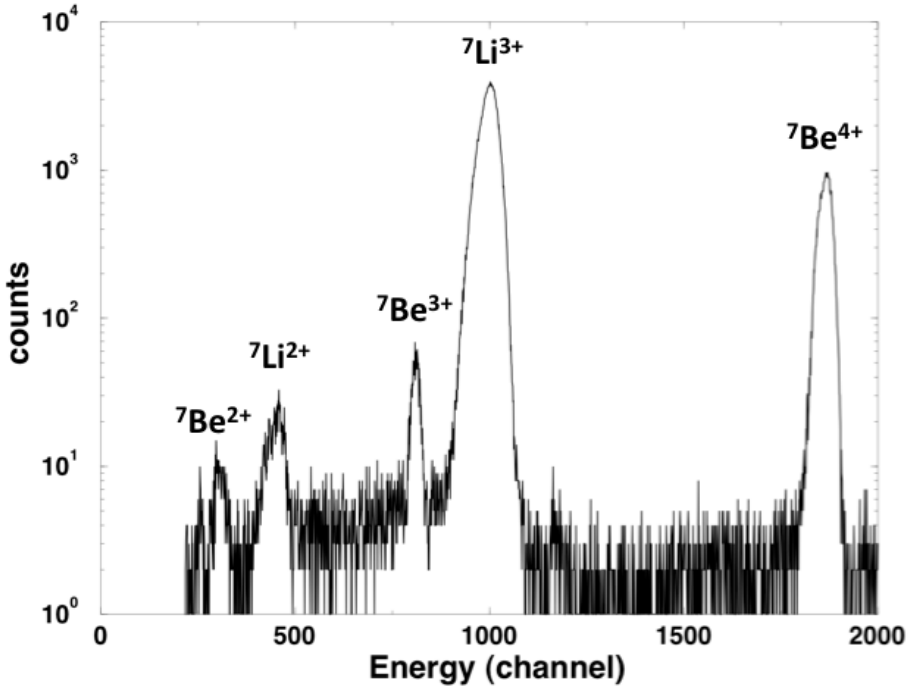

Figure 2.4: Energy spectrum acquired with the monitor detector. The Wien filter was off during the present measurement. The DM operates a selection in magnetic rigidity so we can see three groupings with the same mass and charge. The separation between the $^7Be^{2+}$-$^7Li^{2+}$ peaks and between the $^7Be^{3+}$-$^7Li^{3+}$ peaks is provided by the different energy loss through the PPACs.

2.5.2 Dipole magnet optimization

At this point we turned on the Wien filter with a voltage $\Delta V_{WF} = \pm 45\ kV$ and a magnetic field $B_{WF} = -54.63\ mT$. The opening of the slit S3 was reduced to $x = \pm 15\ mm$.

The Wien filter operates a selection in velocity: inside this optical element the magnetic and electric fields are perpendicular to each other, so the Lorentz force F_L is equal and opposite to the force generated by the electric field F_E:

$$\vec{F_L} = q\vec{v} \times \vec{B} = q\vec{E} = \vec{F_E}$$

$$F_L = qvB = qE = F_E$$

and so

$$vB = E$$

In this way, by properly setting the electric and magnetic fields, we select only a particular velocity $v = E/B$ and we were able to get only the $^7Be^{4+}$ particles.

The RIB optimization is a slightly recursive procedure, therefore after switching on the Wien filter (which may alter the vertical deflection of the beam), we prefer to rescan first the magnetic field of the dipole to maximum the secondary beam rate in this new condition, then we scan the magnetic field of the Wien filter and, after its optimization, we scan again the magnetic field of the dipole. Here we briefly summarize the entire procedure.

At first, we set different values of the magnetic field of the dipole magnet and measured the number of counts in the $^7Be^{4+}$ peak (second column of Table 2.3), the total counts (third column), the purity

of the beam (fourth column, ratio of the second with the third), the current measured on the S2 left slit (position where the primary beam is mainly stopped, fifth column) and the intensity (sixth column, ratio of the second with the fifth).

DM (mT)	$^{7}Be^{4+}$ counts	total counts	purity	S2 left current (a.u.)	transmission (a.u.)
890.51	65476	66772	98.1%	13088	5.00
893.40	79661	81298	98.0%	13288	5.99
897.39	87436	89173	98.1%	13463	6.49
899.63	85632	82767	98.1%	13892	6.16
902.64	74622	76073	98.1%	14133	5.28

Table 2.3: Wien filter on: optimization of the DM. First column: values of the magnetic field of the DM; second column: counts of ^{7}Be particles; third column: total counts; fourth column: purity of the beam (ratio of the counts with respect to the total); fifth column: current measured on the S2 left slit; sixth column: transmission (ratio of the counts with respect to the current measured on the S2 left slit, where the primary beam is stopped). The last two columns are in arbitrary units.

Fig. 2.5 shows the values of the intensity reported in the previous table as function of the magnetic field of the DM. To achieve the best transmission of the secondary beam we chose to set the field at 897.39 mT. Fig. 2.6 shows the corresponding spectrum obtained with this value of magnetic field.

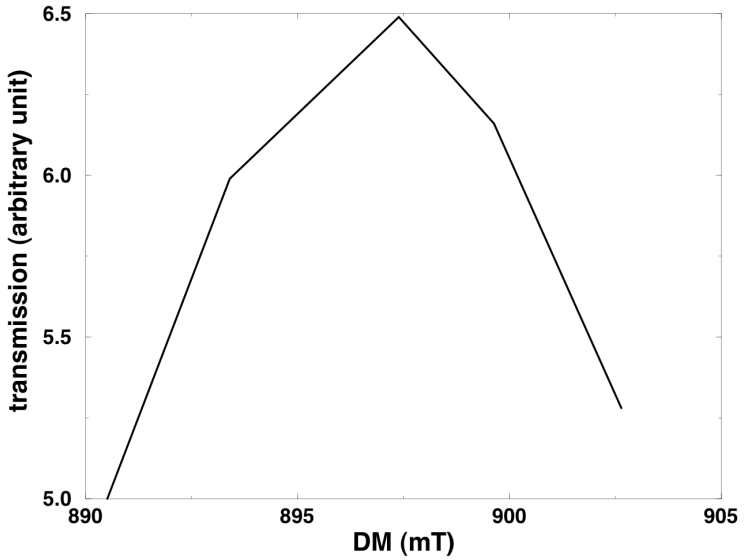

Figure 2.5: ^{7}Be beam transmission (number of counts divided by the current on slit S2) as a function of the magnetic field of the DM.

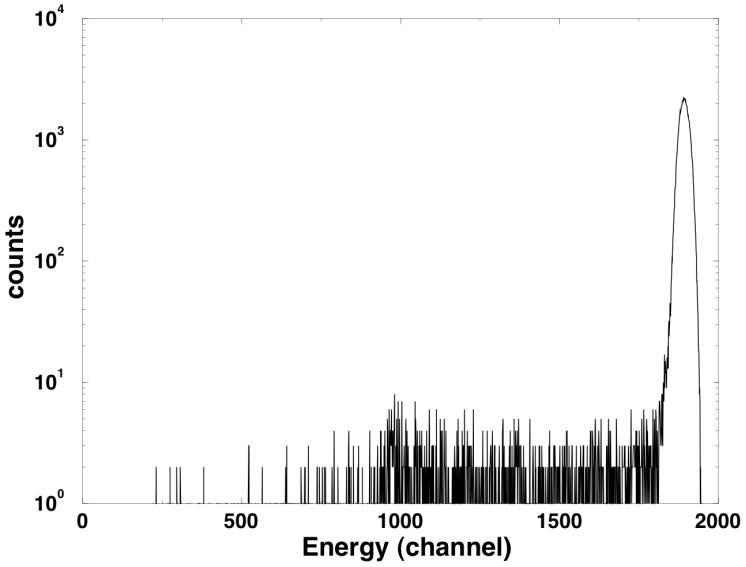

Figure 2.6: Energy spectrum collected by the monitor detector with the WF on and the magnetic field of the DM set to 897.39 mT.

2.5.3 Wien filter optimization

magnetic field of the Wien field, keeping the voltage difference across the electrodes to a constant value of $\pm 45\ kV$. In Table 2.4 we report the values of the magnetic field of the DM and the corresponding counts, total counts, the current on S2 and the intensity, as we made in the previous section for the DM. Figs. 2.7 shows the variation of the secondary beam transmission as a function of the WF magnetic field.

WF (mT)	^{7}Be counts	total counts	purity	S2 left current (a.u.)	transmission (a.u.)
54.77	88149	89933	98.0%	13717	6.43
55.79	88088	89744	98.2%	13501	6.52
56.66	84948	89744	98.1%	13501	6.27

Table 2.4: Optimization of the WF. First column: values of the magnetic field of the WF; the other columns are the same as Table 2.3.

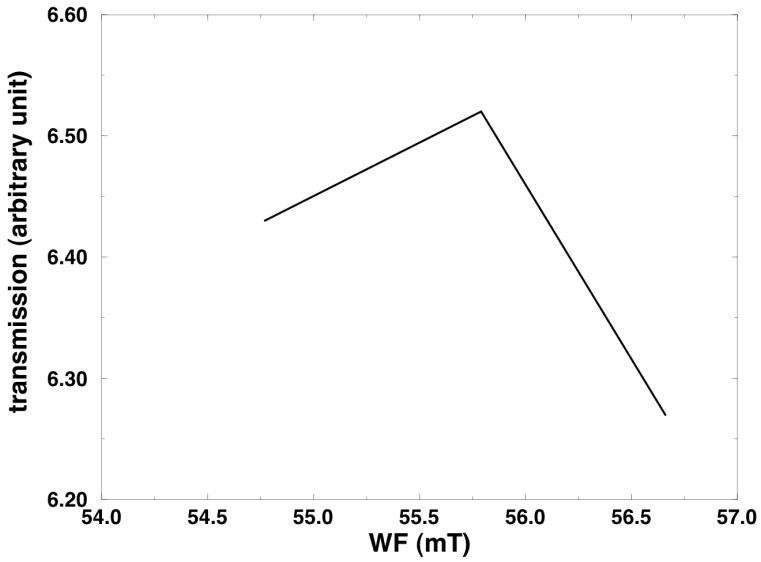

Figure 2.7: Transmission (^{7}Be counts divided by the current on slit S2) as function of the magnetic field of the WF.

2.5.4 Quadrupoles optimization

After the Wien filter we optimized the values of the magnetic fields of the two triplets of quadrupoles. The initial values were calculated by optical calculations, then we performed a scanning in steps of $10-15\ mT$ around the starting values to find the optimum configuration. We provide, as an example, the optimization of the quadrupoles Q4 and Q6.

Q4 optimization

Q4 (mT)	^{7}Be counts	total counts	purity	S2 left current (a.u.)	transmission (a.u.)
286.05	251184	254830	98.6%	13391	18.75
296.00	244823	248581	98.5%	13320	18.34
305.90	228261	231846	98.5%	13203	17.29
315.90	203914	207327	98.4%	13332	15.29
325.90	171374	174430	98.3%	13336	12.85
335.90	140266	142761	98.3%	13530	10.37
345.90	108521	110587	98.1%	13323	8.15
355.90	87436	89173	98.1%	13463	6.49
365.90	70782	72375	97.8%	13566	5.22
375.90	57845	59356	97.5%	13364	4.33

Table 2.5: Optimization of the quadrupole Q4. First column: values of the magnetic field of Q4; the other columns are the same as Table 2.3.

The maximum of the curve in Fig. 2.8 is far from the calculated value probably because of the *steering effect* (second order effect of the quadrupoles) related to the entrance angle of the beam in Q4.

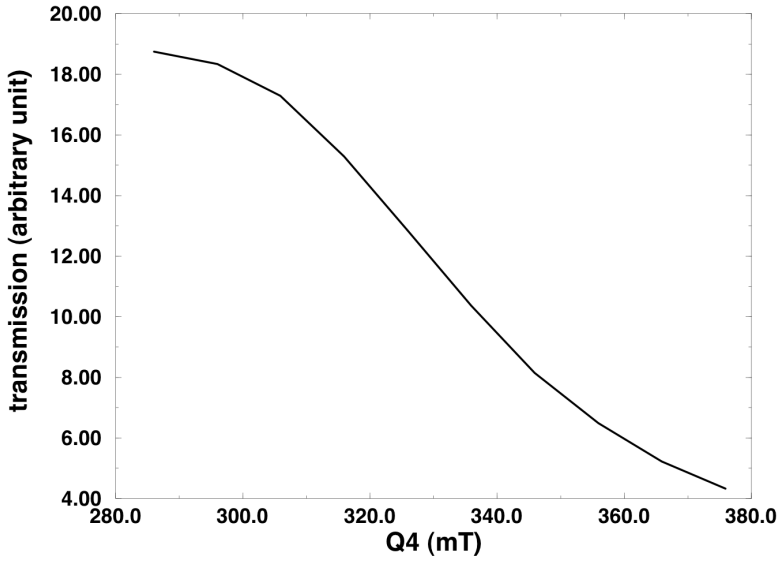

Figure 2.8: Transmission (^{7}Be counts divided by the current on slit S2) as a function of the magnetic field of the quadrupole Q4.

Q6 optimization

Q6 (mT)	^{7}Be counts	total counts	purity	S2 left current (a.u.)	transmission (a.u.)
355.8	231524	235281	98.4%	13534	17.11
370.9	242165	245921	98.5%	13390	18.08
386.0	249896	253822	98.5%	13389	18.66
401.0	243047	246632	98.6%	13540	17.95

Table 2.6: Optimization of the quadrupole Q6. First column: values of the magnetic field of Q6; the other columns are the same as Table 2.3.

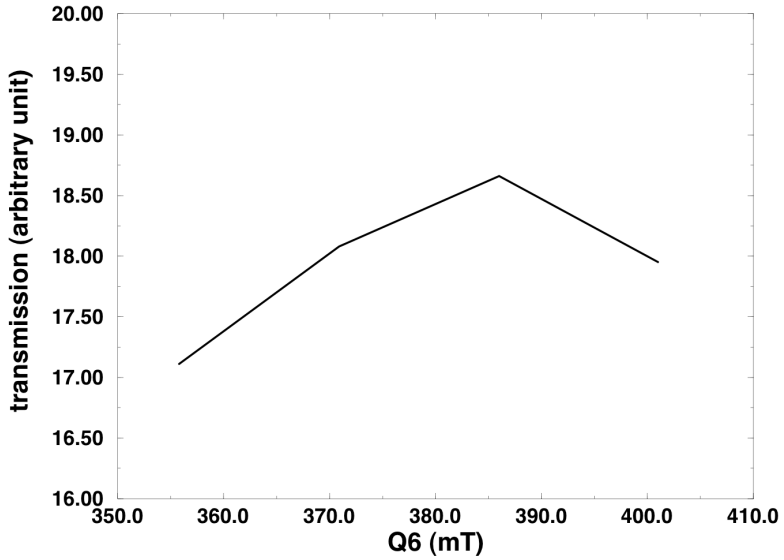

Figure 2.9: Transmission (^{7}Be counts divided by the current on slit S2) as a function of the magnetic field of the quadrupole Q6.

2.5.5 S2 slit optimization

Finally, we adjusted the opening of the slit S2, the values of the procedure of optimization are reported in Table 2.7.

S2 (mm)	^{7}Be counts	centroid (channel)	FHWM (channel)	total counts	purity
$\pm$5.0	328865	1892.8	47.12	334542	98.3%
$\pm$6.0	366195	1892.6	47.59	372861	98.2%
$\pm$7.0	395369	1892.1	47.81	402944	98.1%

Table 2.7: Optimization of the slit S2. First column: values of the opening; second column: counts of ^{7}Be particles; third column: centroid; fourth column: Full Width Half Maximum (FWHM); fifth column: total counts; sixth column: purity (ratio of the counts with respect to the total).

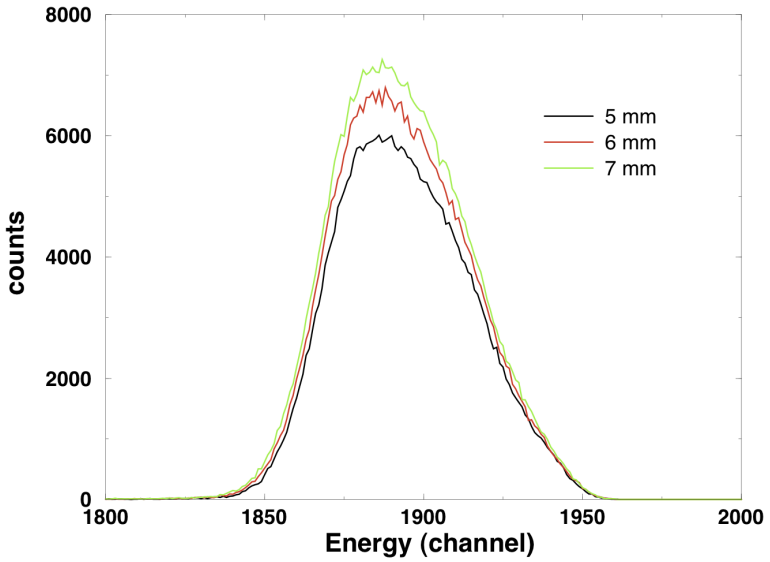

Figure 2.10: Energy spectra for the three openings of S2.

2.6 Running conditions

After this procedure of optimization of the optical elements a serious Wien filter discharge occurred and the electric field of the WF could not be restored to the original value. In fact the beam line was opened to replace a PPAC, that was damaged by a too high particle rate, and afterwards the vacuum conditions in this part of the line were not good enough to sustain the high voltage of the WF. The procedure of reconditioning the electrodes of the Wien filter (usually done well before the experiment) would have required too much time, so the fields were lowered to these values: $E = \pm 40\ kV$ and $B = 49.56\ mT$. The final values of the magnetic fields of the various optical elements are reported in

Table 2.8.

	magnetic field (mT)
Q1	+309.95
Q2	-648.80
Q3	+389.00
DM	-897.62
WF	-49.56
Q4	+286.00
Q5	-592.00
Q6	+386.10

Table 2.8: Final values of the magnetic fields of the optical elements.

To conclude, we report the rate of events seen by the PPAC A, PPAC B and a silicon detector placed on the ladder of the target. Using two grids on the exit of the Tandem to prevent damages to the monitor detector, we measured a counting rate of 4.85 kHz on PPAC A , 3.42 kHz on PPAC B and 2.65 kHz on the silicon. Thus we can define a *purification value*, i.e. the ratio between the counting rate on PPAC A and PPAC B, and its value is 70%, and a *transmission value*, i.e. the ratio between the counting rate on PPAC B and the silicon detector, and its value is 77%.

Figs. 2.11 and 2.12 show the spectra for the two energies E_1 and E_2. The second energy was obtained by the insertion of a aluminum beam degrader (13.77 mm thick).

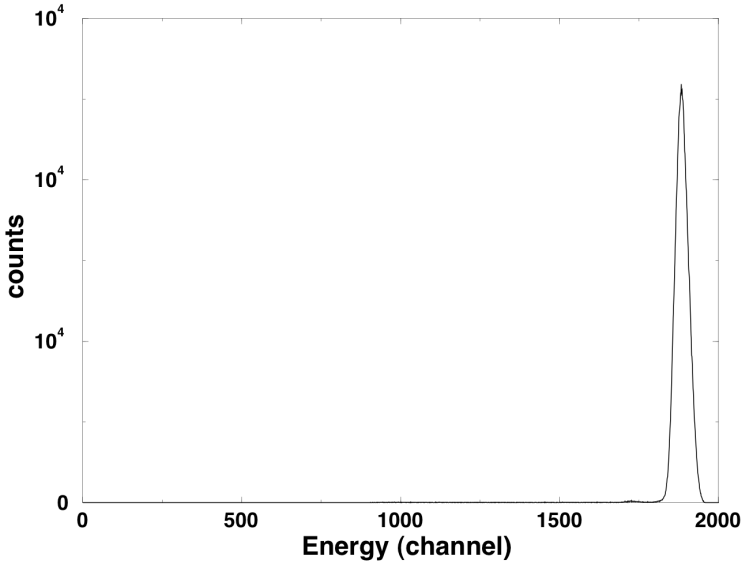

Figure 2.11: Energy spectrum for the first energy of the beam (E_1).

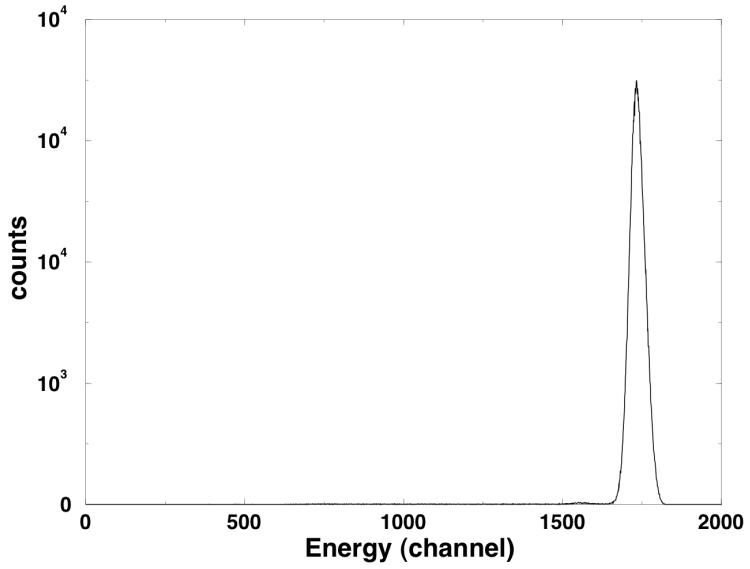

Figure 2.12: Energy spectrum for the second energy of the beam (E_2).

Chapter 3

The EXPADES detector array

This chapter describes the detection set-up used for the present experiment: the EXotic PArticle DEtection System (EXPADES). This detector array has been completely designed, developed, tested and commissioned by the collaboration EXOTIC. The experiment described in this thesis work is actually the first one performed with EXPADES. So far, other 6 experiments have been performed with EXPADES (5 at INFN-LNL, with ^{7}Be, ^{8}Li and ^{15}O RIBs) and 1 at CRIB (RIKEN, Japan with a ^{8}B RIB).

3.1 General overview

Since the typical intensity of RIB is about $10^4 - 10^6$ *pps*, the layout of a high-performance detection systems requires the following concepts:

- charge and mass identification of all reaction products with the highest achievable energy resolution;
- large solid angle coverage, to compensate the low RIBs intensities and to allow the detection in coincidence of particles simultaneously emitted at large relative angles;
- high segmentation, to increase the angular resolution of the detected particles;
- event-by-event beam tracking capabilities, to account for the typical RIB poor emittance and low energy resolution.

The first requisite can be fulfilled by using (at least) two-stage particle detector telescopes, since the energy deposition by a particle passing through a thin material layer strongly depends on its charge and mass. The second and third requirements can be matched by using large area high granularity Double Sided Silicon Strip Detectors (DSSSDs) in a closely-packed configuration around the target. Finally, the last condition can be achieved by the displacement at suitable positions along the beam line of specifically designed high transparency tracking detectors, providing an event-by-event reconstruction of the position hit on the reaction target.

3.2 Conceptual design

EXPADES consists of 8 two-stage $\Delta E - E_{res}$ telescopes of *Double Sided Silicon Strip Detectors* (DSSSDs). There is also the possibility to use 8 ionization chambers as an additional ΔE stage for more complex triple telescopes. The telescopes are arranged in a cylindrical configuration around the target (minimum target-detector distance is about 105 mm) and cover a total solid angle of about 20% of 4π sr. The detectors have active areas of 64×64 mm^2 with 32 strips on front side orthogonally oriented with respect to the 32 strips on back side in order to define 1024 pixels 2×2 mm^2 wide. We use 40/60 μm thick BB7(DS)-40/60 DSSSDs and 300 μm thick BB7(DS)-300 DSSSDs for the ΔE stage and E_{res} layer, respectively (elements "B" and "A" in Fig. 3.1). The detectors are manufactures by Micron Semiconductor Ltd. (UK) [27].

In the original configuration the 8 telescopes are located at the following mean polar angles (with respect to the beam direction): θ_{lab}=27°, 69°, 111° and 153°. However, EXPADES is mounted on a rotatable aluminum disk, therefore different configurations can easily be achieved by properly turning the entire support and, in case, removing one or more modules. The distance of the detectors from the target can be varied with continuity in the range $105 - 225$ mm. Fig. 3.2 shows the EXPADES polar angle coverage in the original configuration for five detector distances from the target and Table 3.1 summarizes the ranges of polar angles θ spanned by each telescope.

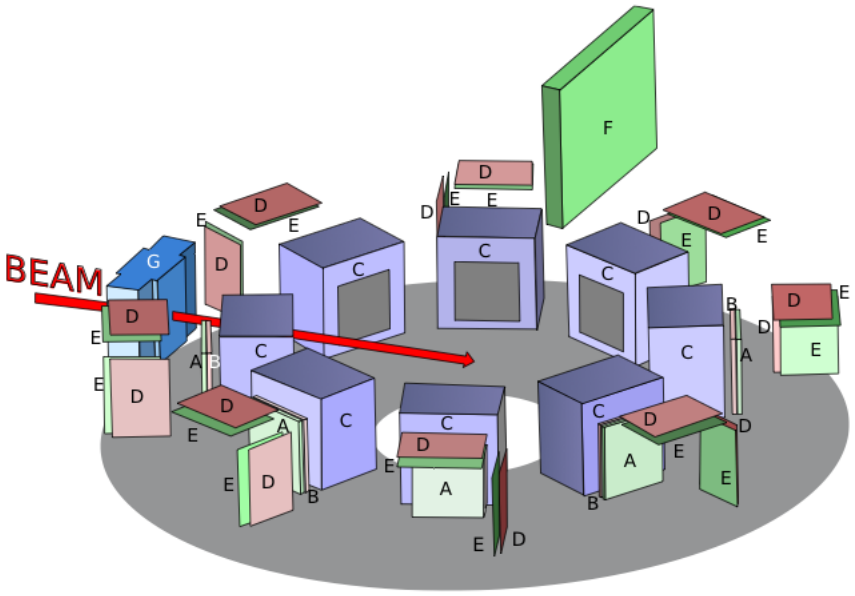

Figure 3.1: Schematic view of the whole detection array EXPADES. A) 300 μm DSSSDs (E_{res} stage). B) 40 μm DSSSDs (ΔE layer). C) Ionization chambers (alternative ΔE stage). D) Charge preamplifier boards for ΔE detectors. E) Electronic boards for the E_{res} stage. F) Motherboard for the E_{res} stage electronics. The beam enters in the detection area from the left passing through the second PPAC of the event-by-event beam tracking system (G).

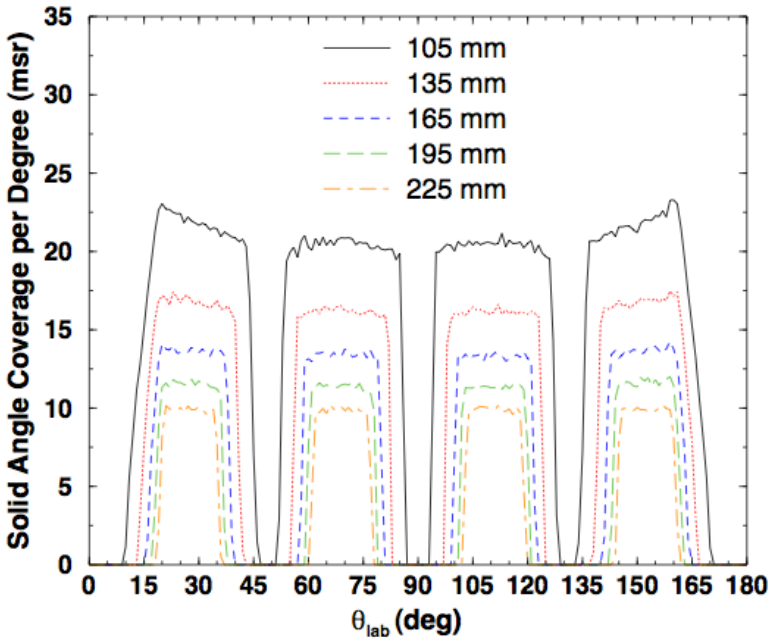

Figure 3.2: EXPADES polar angle coverage for five detector-target distances ($105 - 225$ mm).

distance (mm)	105	135	165	195	225
Telescope 1	$[13°, 44°]$	$[15°, 41°]$	$[17°, 38°]$	$[19°, 36°]$	$[20°, 35°]$
Telescope 2	$[53°, 86°]$	$[52°, 82°]$	$[59°, 80°]$	$[60°, 78°]$	$[61°, 77°]$
Telescope 3	$[94°, 127°]$	$[98°, 124°]$	$[100°, 121°]$	$[102°, 120°]$	$[103°, 119°]$
Telescope 4	$[136°, 167°]$	$[139°, 165°]$	$[142°, 163°]$	$[144°, 161°]$	$[145°, 160°]$
$\Delta\Omega$ (sr)	2.72	1.70	1.16	0.84	0.64

Table 3.1: Ranges of polar angles θ_{lab} spanned by the telescopes of EXPADES for five detector-target distances ($105 - 225$ mm). Last row indicates the overall solid angle coverage, computed with a Monte-Carlo simulations for a point-like source.

3.3 ΔE readout electronics

The ΔE electronics readout includes two homemade modules: (i) a charge sensitive pre-amplifier and (ii) a spectroscopy amplifier with internal Constant Fraction Discriminator (CFD) and Time to Amplitude Converter (TAC). To reduce complexity and costs, the number of the DSSSD strips has been lowered to 16, by short-circuiting at the entrance of the charge preamplifier the signals coming from two adjacent strips.

3.3.1 Charge preamplifiers

Each detector side is connected through a $54 - mm$ kapton cable to a custom Printed Circuit Board (PCB), shown in Fig. 3.3, containing 16 charge sensitive preamplifiers, generating a differential output signal. The main features of the developed charge sensitive preamplifier are the following:

- Number of channels: 16;
- Size: $78 \times 47\ mm^2$;
- Noise: $<$ 3.3 keV at 0 pF; 15 keV at 600 pF;
- RiseTime: $<$ 3.3 ns at 0 pF; 28 ns at 600 pF;
- Sensitivity: 45 mV/MeV;
- Power Consumption: $<$ 900 mW.

Figure 3.3: Preamplifier board for the ΔE stage electronics. Each board handles 16 lines. In the upper side there are the biasing connector (left) and the signal connector (central). Board dimension: $78 \times 47\ mm^2$.

3.3.2 Spectroscopy amplifier MEGAMP

The preamplifier outputs are sent to a specifically developed 16 channel NIM module "MEGAMP". Each MEGAMP channel consists of two units: a) a (standard) spectroscopic amplification unit and b) a timing unit. The timing unit contains two Constant Fraction Discriminators set, respectively, at 30% and 80% of the signal leading edge. These time signals are translated into an analogue signal by an internal Time-to-Analog Converter, that uses as start signal the 30%-CFD signal and as stop signal the 80%-CFD signal, providing a pulse-shape information by measuring the input signal rise–time. Alternatively, an external signal can be used as stop signal for Time-Of-Flight (TOF) measurements.

The block diagram of the circuital implementation of the two units described above is shown in Fig. 3.4. All parameters of the module are remotely set by a serial communication port.

The differential input allows to use an unshielded interconnection for the input signals without picking up noise: the signal is sent to two cables referred to each other (one of them is inverted), so if some noise is present it would hit the two cables in the same way, therefore when the signals are eventually collected, the difference between the signals will not be affected by the noise.

After a polarity inversion, the input signal is split and sent to the spectroscopic amplification unit and to the timing unit. In the first unit the signal is initially processed by two derivative RC (resistor-capacitor) filters and a pole-zero compensation circuit. Alternatively, a fast signal unipolar shaping amplifier can be used, i.e. an integrator with a time constant of 500 ns. The output is subsequently amplified by a user settable gain, and conveniently shaped. In the time unit a leading–edge discriminator enables the entire unit by a threshold set through the output of a 12-bit Digital-to-Analog Converter (DAC). The signal is conveniently shaped and then used as input for the two CFDs, both with automatic walk compensation. The output of the 30% CFD is used as start for the TAC, whereas the stop/reset signal can be either an external ECL signal or alternatively the 80% CFD output. Both outputs are directed to the MEGAMP front panel and the output of the 30% CFD is also used in the logic OR and multiplicity module. We measured an intrinsic time resolution of a single MEGAMP CFD channel of 85 ps (FWHM) for a $500 - mV$ and $20 - ns$ rise time input pulse.

The MEGAMP module provides 16 output signals (one for each input channel) and also a multiplexed output, where the 16 amplitude information and the 16 time information are merged in only one sequential stream of 32 analogue signals. This signal is eventually acquired by a custom 8-channel 12-bit multi-sampling Analogue-to-Digital Converter (ADC).

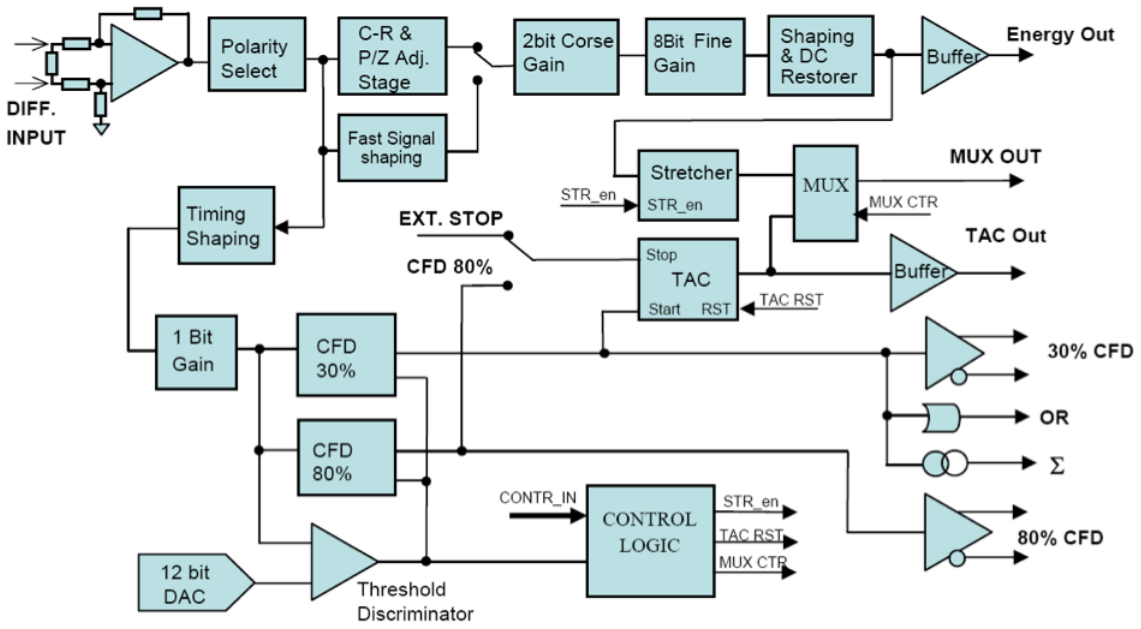

Figure 3.4: Block diagram of one channel of the MEGAMP module.

3.4 E_{res} readout electronics

3.4.1 VA-TA boards

Regarding the E_{res} stage, each side of the DSSSD is connected to a "VA–TA" board through a $54-mm$ long custom kapton cable with low capacitance and ground shielding. This cable was properly designed to reduce noise pick-up and cross-talk between adjacent strips and its shortness ensures the realization of a closely-packed and portable detector set-up. Each VA–TA board houses two 32-channel chips the use of which allows an individual treatment for the 32 strips of each detector side, thus achieving a position resolution of $2 \times 2\ mm^2$ for the E_{res} stage of EXPADES.

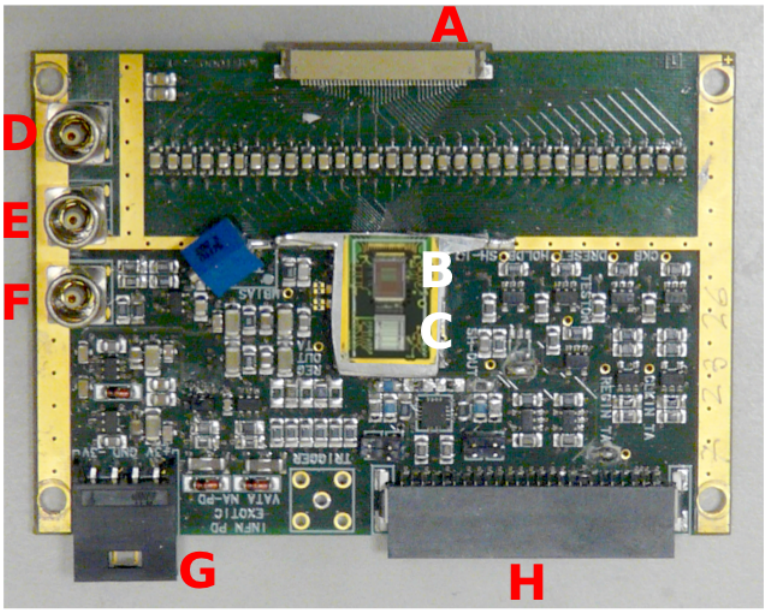

Figure 3.5: A VA–TA board. The various labels indicate: A) ERNI 36-pole connector for the kapton cable, B) VA chip, C) TA chip, D) LEMO connector for the detector bias, E) LEMO connector for VA test input signal, F) LEMO connector for the TA trigger threshold signal, G) 4-pole connector for the VA–TA power supply and H) 48-pole communication port with the EXPADES motherboard. The board dimensions are: $85\ mm \times 60\ mm$.

Fig. 3.5 shows a picture of a VA–TA board. Label "A" indicates the ERNI 36-pole connector (32 signal lines and 4 ground connections), where the kapton cable is inserted into the board. "B" and "C" label the chip VA and TA, respectively, located approximately at the center of the board. On the left-hand side of the VA–TA board there are three LEMO connectors used for the following signals (from top to bottom): detector bias (label "D"), VA test input signal (label "E") and TA trigger threshold signal (label "F"). In the lowest portion of VA–TA board we have a 4-pole connector (label "G") for the power supply of the board itself and a 52-pole port for the communication with the EXPADES motherboard (label "H"). The LEMO connector "D" is connected, through an output flange, to an external NIM power supply module. Connectors "E", "F", "G" and the port "H" of each VA–TA board are instead connected to an EXPADES motherboard, also located under vacuum inside the scattering chamber.

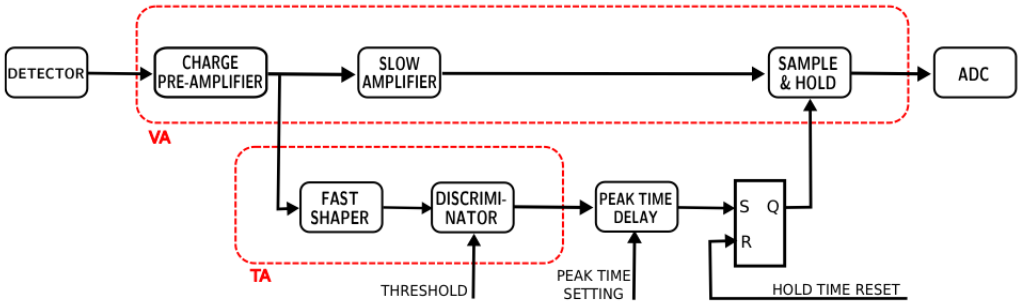

Figure 3.6: Schematic block diagram of the VA–TA board. The chip VA is essentially used as charge preamplifier and slow shaping amplifier, while the chip TA is used as leading edge discriminator for the fast-shaped output signal of the charge preamplifier.

Fig. 3.6 illustrates the block diagram of the VA–TA board. The chip VA essentially consists of a charge preamplifier followed by a slow amplifier (2 μs peaking time) and by a sample-and-hold circuit. The amplification gain can be set, by a proper displacement of four jumpers on the VA–TA board itself, to match approximately the following full-scale ranges: 30, 52, 90 and 113 MeV. The chip TA schematically consists of a fast shaper (75 ns peaking time) and a leading edge discriminator.

Fig. 3.7 shows the generation of the output data stream for a single detector strip. Panel **a** displays the output signal from the VA charge preamplifier and the horizontal red line represents the threshold for the TA leading-edge discriminator. This threshold is externally settable and is common to all the strips of the same VA–TA board. The discriminator output signal (shown in panel **b**) is used as triggering signal for the "peak-time delay" circuit. After a digitally programmable delay (typically 2 μs), a Set–Reset (SR)–latch (panel **d**) is enabled and the VA sample-and-hold circuit is active until the readout sequence is ended (typically after 7 μs). Panels **c** and **e** finally display the output signal of the VA slow amplifier and of the sample-and-hold circuit, respectively.

The outputs of the 32 detector strips is multiplexed in one single signal stream and delivered as input to the ADC. Hence the custom ADC measures a total of 512 samples at 50 MHz for each stream. Consequently 16 samples are collected for each strip.

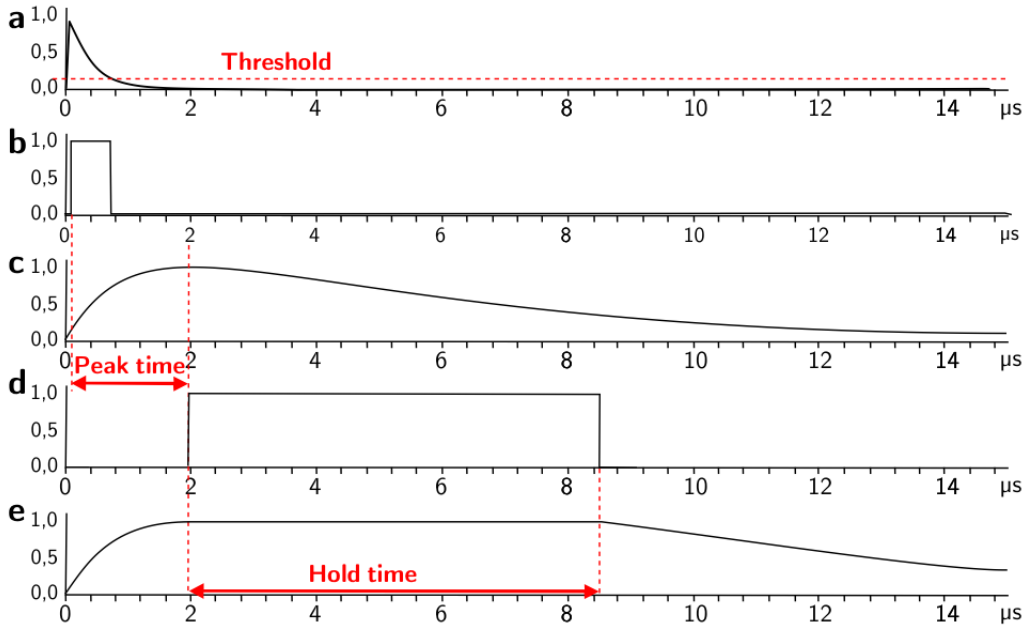

Figure 3.7: Schematic description of the output data stream generation for a single detector strip. Panel **a** sketches the output signal of the VA charge preamplifier, while the corresponding output signal of the TA leading-edge discriminator is illustrated in panel **b**. After a digitally programmable delay a SR–latch is activated (panel **d**). Panel **c** and **e** represent the output of the VA slow amplifier and the output of the the VA sample-and-hold circuit, respectively. Ordinate scales are in arbitrary units.

3.4.2 Motherboard

Each detector side requires the use of one VA–TA board, thus the treatment of all electronic signals coming from the 8 DSSSDs of the E_{res} layer needs 16 chipboards. An additional PCB, called EXPADES motherboard (shown in Fig. 3.8), was designed to handle simultaneously 8 VA–TA boards. The motherboard contains a Field Programmable Gate Array (FPGA) and superintends several different functions, such as VA and TA chip configuration, temperature monitoring, input/output communication with the chips, the I2C module, the EXPADES ADC and the Trigger Supervisor Interface (TSI) board. The motherboard also provides the power supply to the VA–TA boards and contains a DAC unit for the conversion of the (externally settable) TA thresholds and their subsequent delivery to the TA chips.

Referring to Fig. 3.8 for the letters, we have

- **A**) 10-pole connector for the FPGA configuration;
- **B**) 68-pole connector for the input/output digital communication with the ADC;
- **C**) 28-pole connector for the analogue output signal to the ADC;
- **D**) 10-pole connector for the motherboard power supply;
- **E1-E8**) 8 4-pole connectors for powering the VA–TA boards;

- **F**) LEMO connector for the test input signal;
- **G1-G8**) 8 LEMO connectors for delivering the test signals to the VA–TA boards;
- **H**) 10-pole connector for the input/output communication with the I2C module;
- **I1-I8**) 8 LEMO connectors for delivering the threshold signals to the VA–TA boards;
- **J1-J8**) 8 48-pole connectors for input/output communication with the VA–TA boards;
- **K**) 28-pole connector for the communication with the TSI board;
- **L**) 10-pole connector for TSI testing purposes.

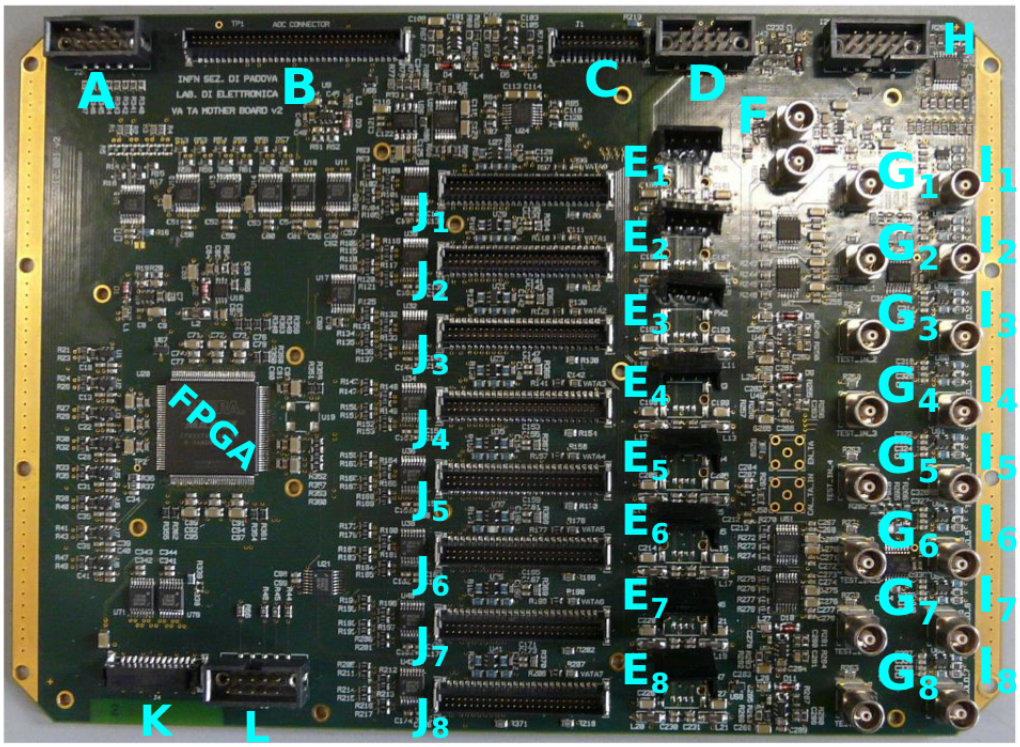

Figure 3.8: Image of an EXPADES Motherboard. Letters label the connectors located on the PCB, see text for details.

3.5 ADC

A custom 12-bit ADC was developed for the EXPADES detector array. The main ADC features are the following:

- Input Channels: 8;
- Noise: < 0.5 LBS RMS;
- Integral non linearity: $< \pm 0.025\%$;
- Differential non linearity: $< \pm 2\%$;

The ADC input range is $[-1, +1]$ V, so that both positive and negative polarity signals can be acquired at the same time. This feature is particularly useful for the treatment of the signals from the E_{res} layer, since the same layout was employed for the VA–TA boards connected to both the detector front and rear side and, therefore, the corresponding multiplexed output signals have opposite polarities (so the baseline is located around channel 2048 of the 12–bit ADC range). Positive and negative polarity signals will approximately populate the ADC range [2049-4095] and [0-2047], respectively. All signals coming from the ΔE stage have the same (positive) polarity, since an additional inversion stage is added for negative polarity signal at the entrance of the MEGAMP module. In this case the ADC input range is shifted towards the interval $[0, +2]$ V, the baseline is located close to the ADC channel 0 and recorded events can span the entire 12-bit ADC range.

3.6 DAQ

The custom ADCs and the TSI board are housed in a VERSA-Module Eurocard (VME) crate connected to the acquisition computer. Data monitoring and acquisition software consists of:

- the XDAQ [28] application which handles the communication between the acquisition computer and the VME boards and executes the readout procedures, by storing data on disk and simultaneously sending them through a Transmission Control Protocol (TCP) socket for on-line visualization;
- the Run Control and Monitoring System (RCMS [29]), a net platform that can be remotely handled by the user through an internet connection and it is used for configuring the different VME modules and the programmable registers of the EXPADES motherboards, for the acquisition run control and for displaying relevant on-line information.

On-line spectra are visualized by means of the computer program CRACOW [30].

3.7 Running configuration

In november 2013, 6 (out of 8) DSSSD telescopes of EXPADES were installed at the final focal plane of the In-Flight RIB facility EXOTIC. The telescope arrangement around the ^{208}Pb target can be seen in Fig. 3.9. Table 3.2 presents the distances and the mean polar angles of the telescopes with

respect to the target. The telescope F was placed farther than the others to prevent the secondary beam to hit the electronics boards.

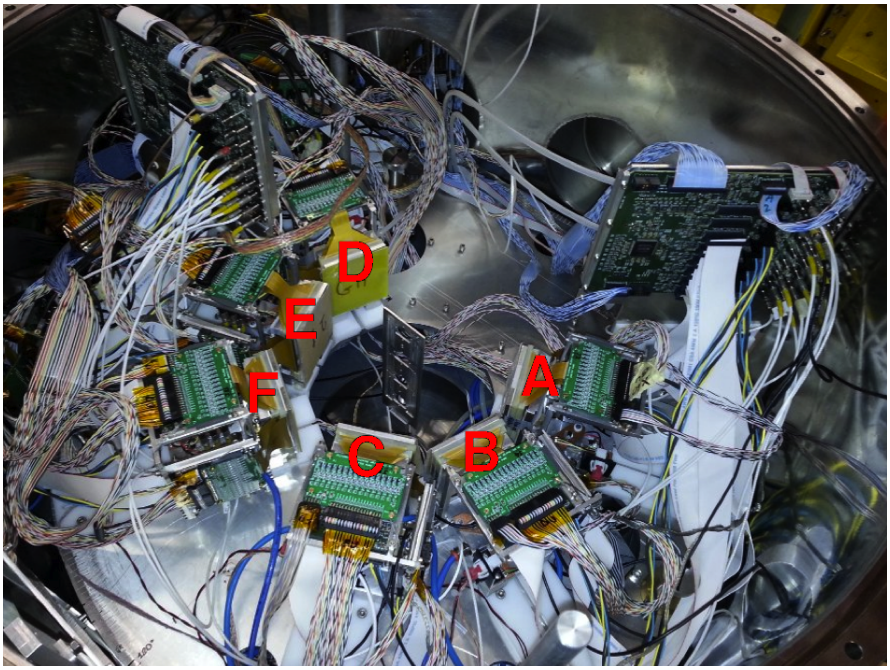

Figure 3.9: Picture of the EXPADES array as used during the experiment. Letters A, ..., F identify the six telescopes. The target ladder can be seen in the middle; the beam comes from the bottom-left part of the picture and passes through telescopes C and F.

Telescope	distance (mm)	angle (deg)
A	111.0	69.0
B	113.5	111.0
C	111.5	153.0
D	112.5	-69.0
E	109.5	-111.0
F	141.5	-153.0

Table 3.2: Distances and the mean polar angles of the telescopes of the EXPADES array with respect to the target as used during the experiment. We used negative values for the telescopes placed on the left side of the beam line.

Chapter 4

Kinematics of 2-body reactions

4.1 General description

In this chapter we review the kinematical properties of 2-body reactions, which are routinely employed at EXOTIC for the RIBs production and that we plan to study in this thesis work with the detector array EXPADES.

We can write a 2-body nuclear reaction in this form

$$a + X \rightarrow b + Y \tag{4.1}$$

where a is the projectile and X the target b and Y are the reaction products. If the incident and outgoing particles are the same it is a *scattering* process, *elastic* if b and Y are in their ground states and *inelastic* if b or Y is in an excited state (from which it will generally decay quickly by γ emission).

In *direct reactions*, for example the *transfer reactions* where one or two nucleons are transferred between projectile and target, only very few nucleons take part in the reaction, while the remaining nucleons of the target are not involved. In the *compound nucleus* mechanism, the incoming and target nuclei merge briefly for a complete sharing of energy and angular momentum before one or more outgoing nucleons are ejected. Between these two cases are the *resonance reactions*, in which the incoming particle forms a "quasibound" state before the outgoing particle is ejected.

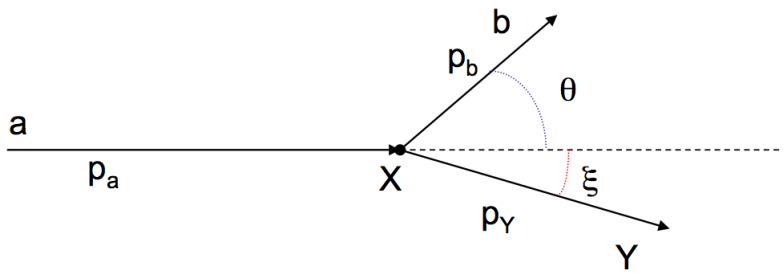

Figure 4.1: Reaction geometry for $a + X \rightarrow b + Y$.

Conservation of total relativistic energy in our basic reaction gives

$$m_X c^2 + T_X + m_a c^2 + T_a = m_Y c^2 + T_Y + m_b c^2 + T_b \tag{4.2}$$

where T's are kinetic energies (for which we can use the nonrelativistic approximation $T = \frac{1}{2}mv^2$ at low energy) and m's are the rest masses. We define the *reaction Q-value* as the difference between initial mass energy and the final mass energy:

$$Q = (m_{in} - m_{fin})c^2 \tag{4.3}$$

$$= (m_X + m_a - m_Y - m_b)c^2 \tag{4.4}$$

or equivalently:

$$Q = T_{fin} - T_{in} \tag{4.5}$$

$$= T_Y + T_b - T_X - T_a \tag{4.6}$$

The Q-value may be positive, negative or zero. If $Q < 0$ the reaction is *endothermic*, and initial kinetic energy is converted into nuclear mass or binding energy. When $Q > 0$ the reaction is said to be *exothermic*; in this case nuclear mass or binding energy is released as kinetic energy of the final products.

We can apply the previous equations in the laboratory reference frame, where the target nuclei are considered to be at rest: conserving linear momentum along and perpendicular to the beam direction gives (see Fig. 4.1)

$$p_a = p_b \cos\theta + p_\gamma \cos\xi \tag{4.7}$$

$$0 = p_b \sin\theta - p_\gamma \sin\xi \tag{4.8}$$

Regarding Q as a known quantity and T_a (and therefore p_a) as a parameter that we control, we can eliminate ξ and T_Y from the equations 4.6-4.8 to find a relationship between T_b and θ:

$$T_b^{1/2} = \frac{(m_a m_b T_a)^{1/2}\cos\theta \pm \{m_a m_b T_a \cos^2\theta + (m_Y + m_b)[m_Y Q + (m_Y - m_a)T_a]\}^{1/2}}{m_Y + m_b} \tag{4.9}$$

If $Q < 0$, there is a minimum value of the energy of the incident particle (T_a^{th}) below which the reaction is not possible:

$$T_a^{th} = (-Q)\frac{m_Y + m_b}{m_Y + m_b - m_a} = (-Q)\frac{m_X + m_a}{m_X} \tag{4.10}$$

In the previous sections we specified that the negative Q-value 2-body reactions are preferred for the RIB production at EXOTIC, since they bring an additional forward focusing to the reaction products. However, the main drawback related to the use of these reactions is the fact that they introduce a threshold condition to the projectile energy, which sometimes may exceed the capability of the LNL Tandem accelerator. Table 4.1 summarizes the main RIB production reactions at EXOTIC, their Q-values, threshold energies in the laboratory frame and the maximum projectile energies E_{max} deliverable by the Tandem.

The actual production scheme is a little more complicate since one has to consider also all the energy losses in the gas target Havar window, through the gas region and the exit window.

On the other side, if $Q > 0$, there is no threshold condition and the reaction will proceed even for very small energies, although we may have to overcome the Coulomb barriers not considered here and which will tend to keep a and X outside the range of each other's nuclear force.

Reaction	Q-value (MeV)	T_a^{th} (MeV)	E_{max} (MeV)
p(^{7}Li^{3+}, ^{7}Be)n	-1.64	13.09	58.0
p(^{15}N^{5+}, ^{15}O)n	-3.54	56.17	87.0
p(^{17}O^{7+}, ^{17}F)n	-3.54	63.30	116.0
^{3}He(^{6}Li^{3+}, ^{8}B)n	-1.97	5.91	58.0
d(^{7}Li^{3+}, ^{8}Li)p	-0.19	0.86	58.0

Table 4.1: Main RIB production reactions at EXOTIC. The maximum energy was calculated considering the maximum voltage (14.5 MV) sustainable by the LNL Tandem accelerator.

There is a maximum angle θ_m function of T_a such that for $0 < \theta < \theta_m$ we have two values of T_b (θ_m can be obtained putting the expression that gives T_b equals to zero):

$$\cos^2\theta_m = -\frac{(m_Y + m_b)[m_Y Q + (m_Y - m_a)T_a]}{m_a m_b T_a} \tag{4.11}$$

Table 4.2 shows the maximum angles θ_m for each reaction reported in Table 4.1.

Reaction	θ_m [deg]
p(^{7}Li^{3+}, ^{7}Be)n	7.3
p(^{15}N^{5+}, ^{15}O)n	2.3
p(^{17}O^{7+}, ^{17}F)n	2.4
^{3}He(^{6}Li^{3+}, ^{8}B)n	13.8
d(^{7}Li^{3+}, ^{8}Li)p	10.9

Table 4.2: θ_m for the main RIB production reactions at EXOTIC.

4.2 Elastic scattering

Let us now consider the case of an elastic scattering reaction whose Q-value is zero and equation 4.9 becomes:

$$T_b^{1/2} = \frac{(m_a^2 T_a)^{1/2}\cos\theta \pm \{m_a^2 T_a \cos^2\theta + (m_X + m_a)[(m_X - m_a)T_a]\}^{1/2}}{m_X + m_a} \tag{4.12}$$

The black lines in Figs. 4.2-4.3 represent the calculated T_b as a function of the scattering angle θ_{lab} for the reaction ^{7}Be+^{208}Pb at $E_1 = 40.65\ MeV$ and $E_2 = 37.55\ MeV$, respectively. The blue dots in Figs. 4.2-4.3 are the simulated events obtained considering a non-zero thickness of the target. Since the minimum energy is larger than the energy corresponding to a range in 50 μg of silicon, our set-up allows us to identify unambiguously the elastic scattering process through the ΔE-E_{res} technique.

4.3 Inelastic scattering

The inelastic scattering occurs when in the final state the ^{7}Be emerges in its first excited state (the only bound excited state below the breakup threshold) with energy $E_x = 0.429\ MeV$ or when the

target of ^{208}Pb gets excited (octupole excitation) with energy $E_x = 2.615\ MeV$. Due to secondary beam energy resolution and to the target thickness, our detection system cannot distinguish between the elastic and quasi-elastic processes as can be seen Figs. 4.2-4.3.

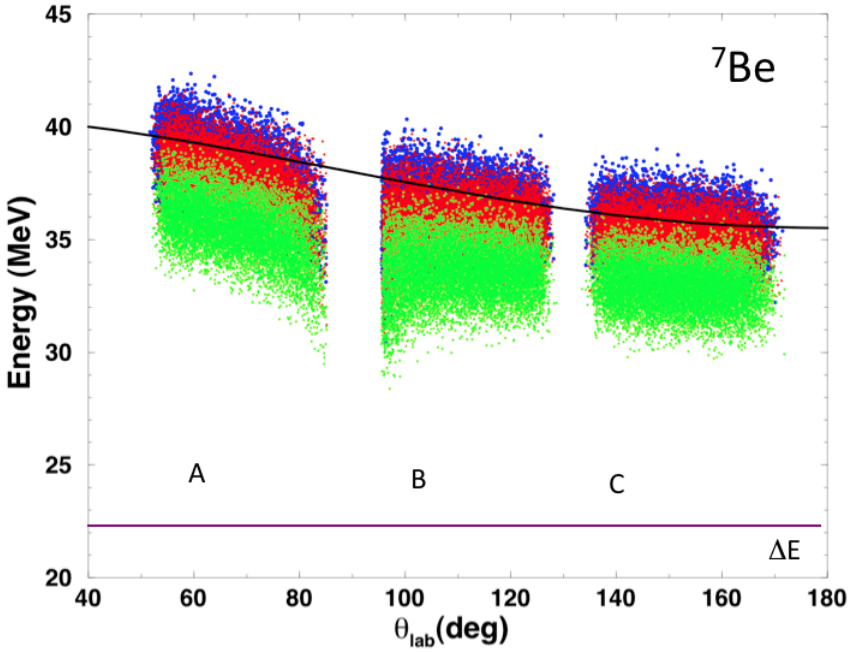

Figure 4.2: ^{7}Be energy vs. laboratory angle for the energy $E_1 = 40.65\ MeV$: the black curve is Eq. 4.10 while the colored dots are the simulated events taking into account the target thickness, the beam spot on the target, geometry of EXPADES, the energy resolution of the beam; in blue we reported the elastic case, while the inelastic excitation of the projectile ($E_x = 0.429\ MeV$) is shown in red, and the inelastic case with excitation of the target ($E_x = 2.615\ MeV$) is shown in green; the purple line represents the minimum ^{7}Be energy needed by the particles to cross the first detector stage. The energy loss in the $\Delta E + E_{res}$ stages, not shown, is 74.8 MeV.

4.4 Transfer reactions

According to the semiclassical model of Brink [9], transfer channels should preferably populate final states with excitation energies around $E_x = Q_{gg} - Q_{opt}$, Q_{gg} being the ground-state-to-ground-state Q-value and Q_{opt} the optimum Q-value, defined by the formula

$$Q_{opt} = \left(\frac{Z_b Z_Y}{Z_a Z_X} - 1\right) E_{c.m.} \tag{4.13}$$

where Z_a and Z_A are the atomic numbers of the two particles in the initial state, Z_b and Z_B those of the two particles in the final state, and $E_{c.m.}$ the bombarding energy in the center-of-mass frame.

The transfer processes are the following

$$^{7}Be +^{208} Pb \rightarrow^{3} He +^{212} Po \tag{4.14}$$

$$^{7}Be +^{208} Pb \rightarrow^{4} He +^{211} Po \tag{4.15}$$

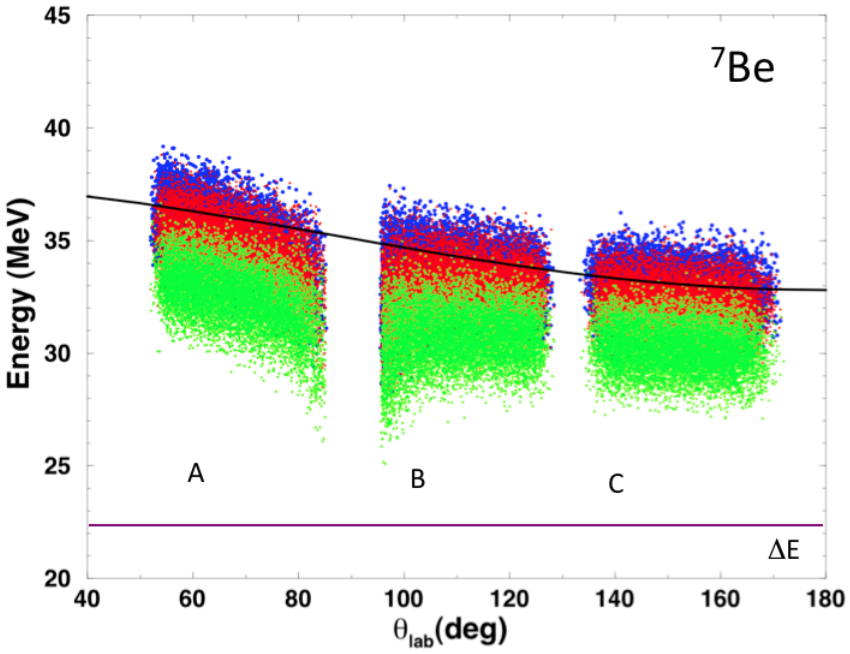

Figure 4.3: Same as Fig. 4.2 for energy of the beam $E_2 = 37.55\ MeV$.

We considered ^{4}He, ^{3}He as ejectiles, and we performed the calculations of Q_{gg}, Q_{opt} and E_x, reported in Table 4.3-4.4.

Ejectile	Q_{gg} (MeV)	Q_{opt} (MeV)	E_x (MeV)
^{3}He	-10.54	-20.50	9.96
^{4}He	4.029	-20.50	24.53

Table 4.3: List of the ejectiles considered for the calculations performed with the simulation program. For each ejectile we indicated the ground- state-to-ground-state Q-value (Q_{gg}), the optimum Q-value (Q_{opt}), and the final-state excitation energy ($E_x = Q_{gg} - Q_{opt}$) for the energy of the beam $E_1 = 40.65\ MeV$.

Ejectile	Q_{gg} (MeV)	Q_{opt} (MeV)	E_x (MeV)
^{3}He	-10.54	-18.94	8.39
^{4}He	4.029	-18.94	22.96

Table 4.4: Same as in Table 4.3 for the energy of the beam $E_2 = 37.55\ MeV$.

Similarly to Figs. 4.2-4.3, Figs. 4.4-4.7 display the calculated kinetic energies for the ^{3,4}He ejectiles for the two already considered bombarding energies of $E_1 = 40.65\ MeV$ and $E_2 = 37.55\ MeV$: the black curve is the expression 4.9 while the colored dots are the simulated events taking into account the thickness of the target; as we can see, in all cases these points lie between the purple lines, that represent the minimum energy needed by the particles to cross the first detector stage and the second one, so our array system is well suitable to detect these kind of events.

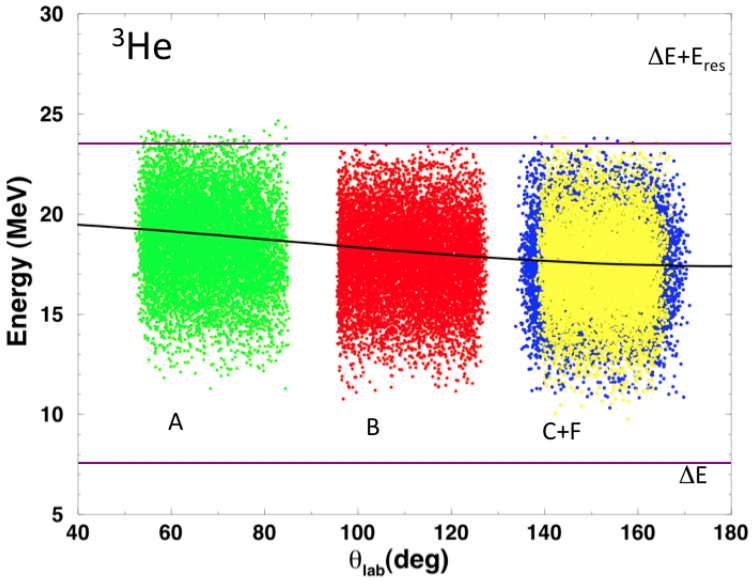

Figure 4.4: ^{3}He energy vs. laboratory angle. The reaction considered is ^{7}Be+^{208}Pb $\rightarrow$ ^{3}He+^{212}Po at $E_1 = 40.65\ MeV$. The black curve is Eq. 4.10 while the colored dots are the simulated events taking into account the target thickness, the beam spot on the target, geometry of EXPADES, the energy resolution of the beam; the purple lines represent the minimum energy needed by the particles to cross the first detector stage and the second one. We reported only the events seen by the detectors placed on the right side, A (green), B (red), C (blue) because the others telescopes would have seen mainly the same pattern; we decide to show the events seen by the telescope F because it is placed at a different distance to the target with respect to the others. We used $\sigma_{E_x} = 2.0\ MeV$, as experimentally observed for the ^{3}He production in the reaction ^{7}Be+^{58}Ni at 22 MeV [21].

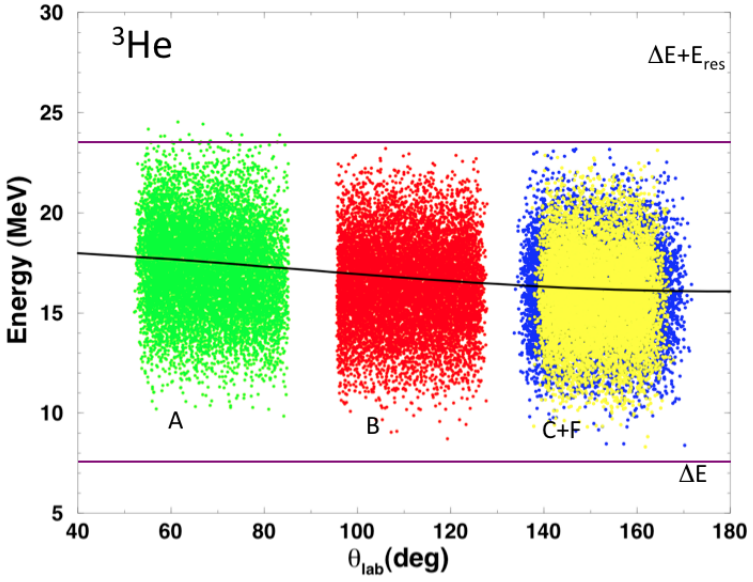

Figure 4.5: Same as Fig. 4.4 for energy of the beam $E_2 = 37.55\ MeV$.

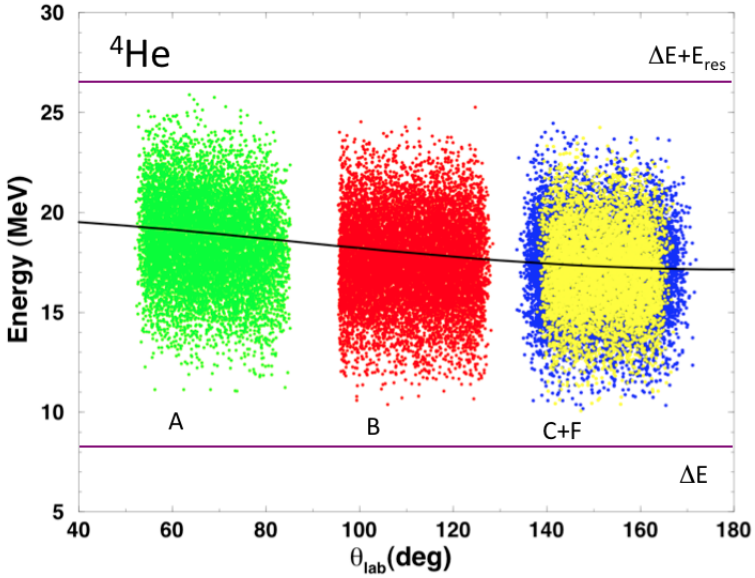

Figure 4.6: ^{4}He energy vs. laboratory angle. The reaction considered is ^{7}Be+^{208}Pb $\rightarrow$ ^{4}He+^{211}Po at $E_1 = 40.65\ MeV$. The color references are the same as Fig. 4.4.

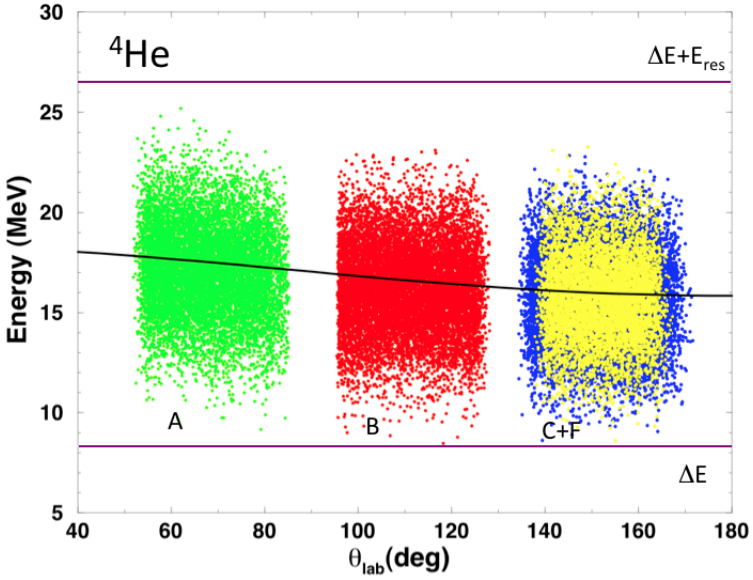

Figure 4.7: Same as Fig. 4.6 for energy of the beam $E_2 = 37.55\ MeV$.

Chapter 5

Data Analysis

In this chapter we schematically describe all the steps followed in the data reduction procedure from the raw data stored in disk during the experiment to the evaluation of the ^{7}Be, ^{3}He and ^{4}He angular distributions.

5.1 $\Delta E - E_{res}$ technique

With the $\Delta E - E_{res}$ technique we can distinguish different isotopes in a rather easy way. A particle with energy E_{tot} entering the first detector stage deposits an energy ΔE and then, depending on its initial kinetic energy, either stops in the second detector stage or passes through it. Following the schematic drawing of Fig. 5.1, a particle with velocity $v = \beta c$ passing through a thin material layer looses energy according to the well-known *Bethe-Bloch formula* [4]:

$$-\frac{dE}{dx} = \frac{4\pi}{m_e c^2}\frac{nz^2}{\beta^2}\left(\frac{e^2}{4\pi\epsilon_0}\right)^2\left[\ln\frac{2m_e c^2\beta^2}{I(1-\beta^2)} - \beta^2\right] \tag{5.1}$$

where v is the velocity of the particle, z its charge, E its energy, n the material electron density, I the mean excitation potential; c is the speed of light, ϵ_0 the vacuum permittivity, e and m_e the electron charge and the rest mass respectively. n is given by:

$$n = \frac{N_A \cdot Z \cdot \rho}{A \cdot M_u}$$

where ρ is the density of the material, Z its atomic number, A its atomic mass, N_A the Avogadro number and M_u the Molar mass constant.

So a greater velocity of the traveling particle leads to a smaller specific energy loss into the material. Considering particles 1-3 in Fig. 5.1 we can see that a smaller energy is lost in the ΔE stage as the initial energy E_{tot} increases, and the remaining part is deposited in the E_{res} stage. Particle 4 has enough energy E_{tot} to travel across the whole second stage, but not to escape it, so it loses the maximum possible energy (E_{max}) in the E_{res} stage.

Particles 5-6 have even greater initial energies, so they lose a smaller amount of energy in the detectors as they pass through them. This explains the characteristic shapes of the so-called "bananas" in the 2D correlation plots $\Delta E - E_{res}$ (see right panel of Fig. 5.1).

According to the Bethe-Bloch formula, different isotopes occupy different places in the $\Delta E - E_{res}$

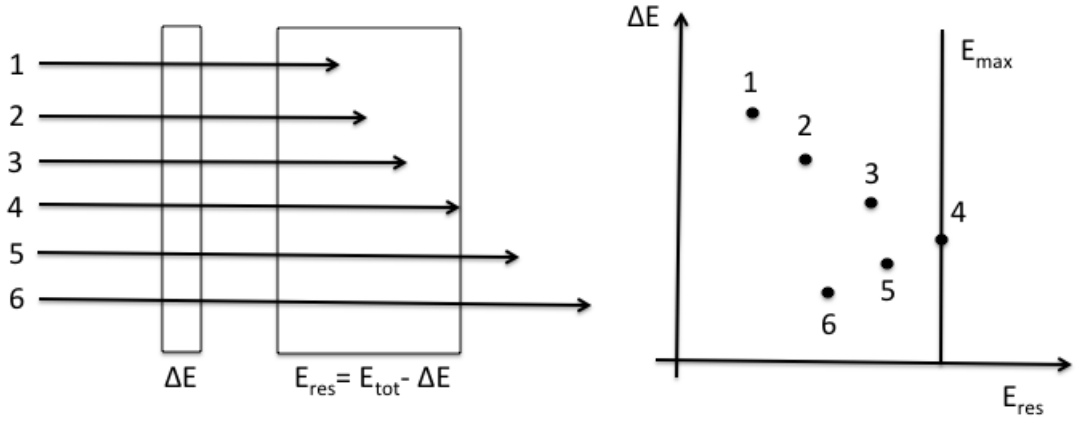

Figure 5.1: Building of the 2D correlation plots $\Delta E - E_{res}$.

plots, in particular the isotopes with low A are located on the bottom left part of the chart.
Since these curves do not intersect each other, although a certain spread of the points could be present due to the detector energy resolution, we can identify the nuclear species involved in the exit channel of the reaction.

5.2 Trigger of the experiment

The master trigger of the experiment was a logical coincidence ("AND") between a signal from the cathode of PPAC A and the "OR" signal of all DSSSDs. The beam encounters at first PPAC A and then, after in case the nuclear reaction with the target, reaches EXPADES. The time difference (i.e. the time of flight) between the two signals is several tens of ns, therefore the signal from the cathode of PPAC A was delayed (by 200 ns) in order to match properly the coincidence window with the "OR" signal of the DSSSDs.

The master trigger signal is also used as *Commom START* for the TDC module used for acquiring the PPAC time signals. The stop signals to the TDC channels were provided individually by the cathode and the coordinate signals (all delayed by 400 ns) of the two gas detectors.

On the other side, the TACs internal to the MEGAMP modules and used for measuring the time signals from the EXPADES ΔE strips, were operated in *Common STOP* with the stop signals provided by the master trigger itself. In this case, it is indeed impracticable to delay all 192 time signals (16 strips $\times$ 2 detector side $\times$ 6 telescopes) from the EXPADES ΔE stage. See Fig. 5.2.

Moreover, during the experiment a fixed-amplitude and fixed-frequency (2 Hz) pulser signal was artificially sent to the inputs of the preamplification stages of all telescopes and acquired in (random) coincidence with a signal from cathode of PPAC A. The pulser signal is employed for monitoring amplification gain instabilities and the DAQ dead-time and it generally appears as a sharp peak in the energy spectra.

The PULSER signal was also used before and after the experiment to determine the position of zero energy: different amplitude values in the range $0.5 - 3.5$ V were acquired, then a linear extrapolation permitted to extract the 0 V corresponding to the 0 MeV energy. This procedure is needed because the energies of the α particles from standard calibration sources are quite close to

each other ($5.157 - 5.806\ MeV$) therefore an additional point is useful to compute the regression line. We used the PULSER peaks also to evaluate the efficiency of the electronic chain during the experiment by analyzing the integrals of the peaks for every strip. Actually two peaks, instead of just one, were observed for all the strips, however since the shift in energy happened simultaneously for all strips, it is more probable that the problem was related to a sudden change in the amplitude of the pulser signal itself than to a variation of the gain amplification for all strips at the same time. We concluded that there was no amplification drift, it was a problem related to the PULSER signal itself and the event-by-event analysis showed that the shift in energy happened simultaneously for all strips, and therefore might be correlated to a shift in the amplitude of the PULSER signal rather than to a variation of the gain amplification for all strips.

When the DAQ is enabled, all signals from all ΔE and E_{res} strips are recorded. We usually have a very limited numbers (1-2) of ΔE and E_{res} strips fired per event, all other strips detect a "zero-signal" which contributes to the so-called BASELINE. The position of this particular signal should be identical (within the errors) with the offset (zero energy) obtained by interpolating the PULSER signals as mentioned above.

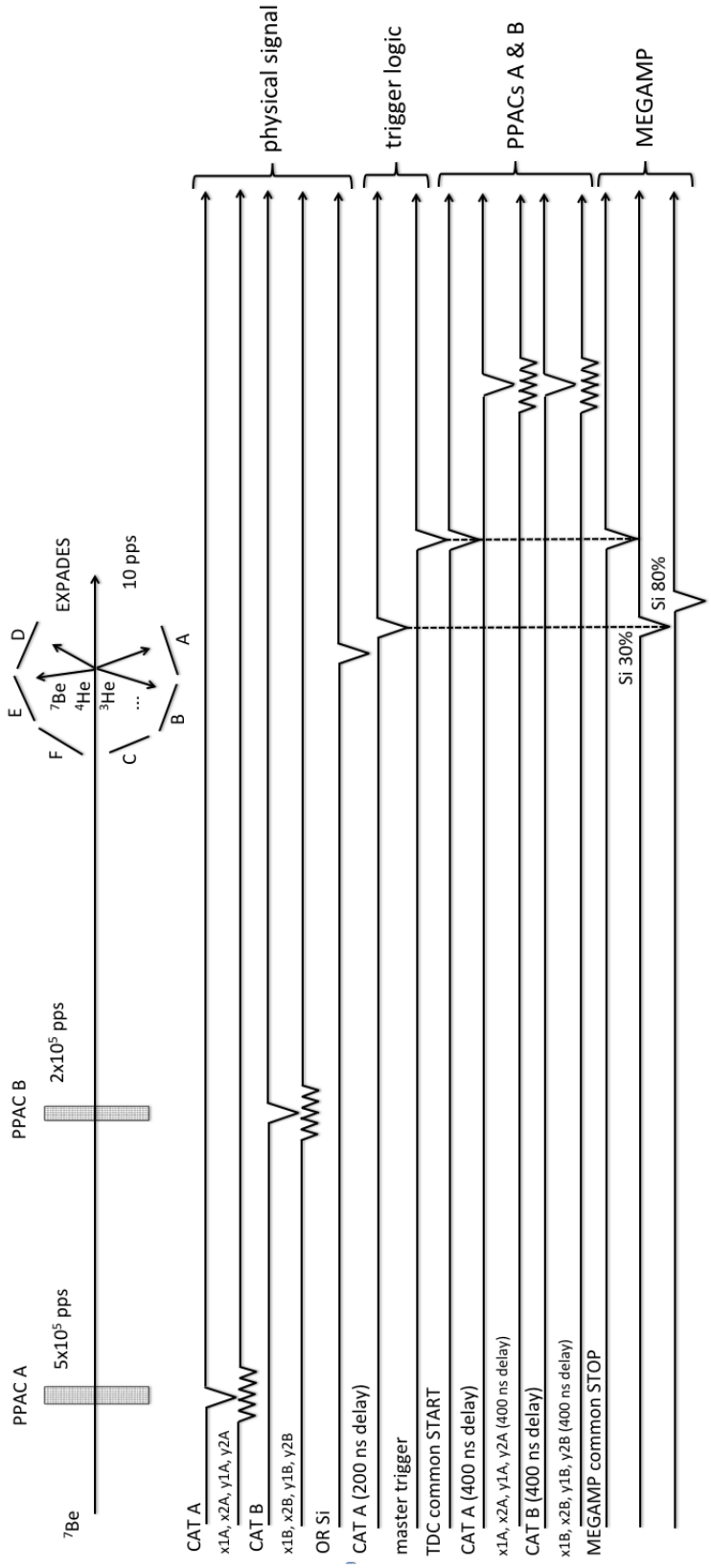

Figure 5.2: Trigger scheme of the experiment. See text for details.

5.3 Energy calibration with α sources

The ΔE energy calibration was performed with standard triple α sources: ^{239}Pu (5.157 MeV), ^{241}Am (5.486 MeV), ^{244}Cm (5.805 MeV) just after the completion of the experiment. For the E_{res} stage the energy calibration was performed prior to the experiment (see Figs. 5.3-5.4 for two examples of these spectra).

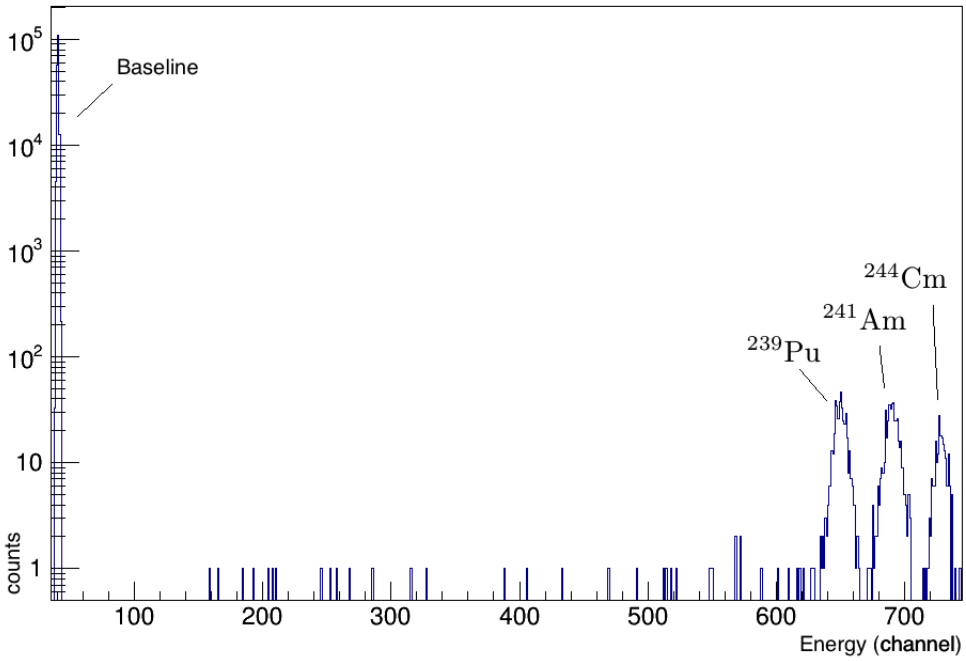

Figure 5.3: Example of spectrum of the triple source, visible on the right side, as detected by a ΔE strip.

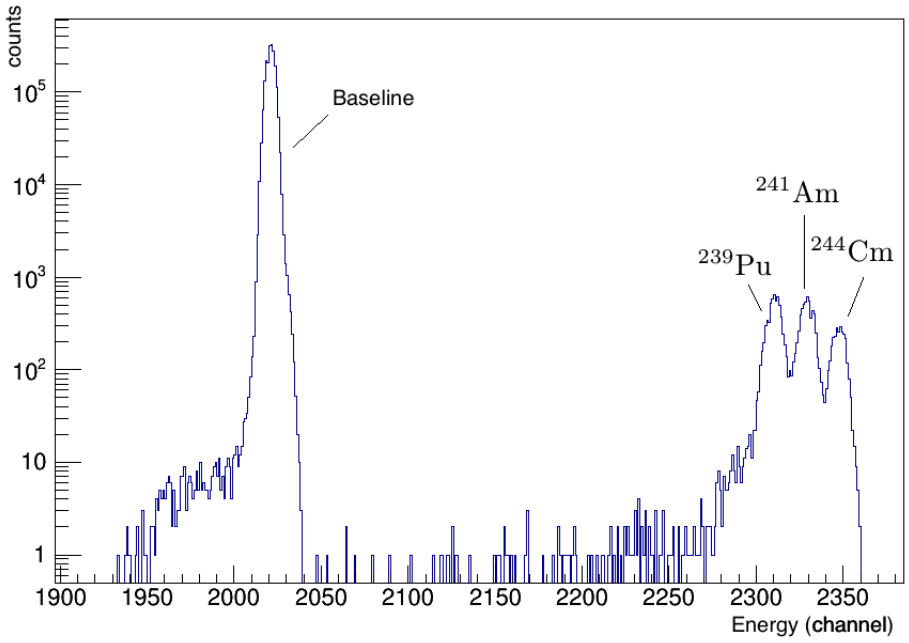

Figure 5.4: Example of spectrum of the triple source, visible on the right side, as detected by a E_{res} strip.

The calibration, made individually for each strip of every telescope (192 strips for the ΔE and 384 for the E_{res}), consists in calculating the three centroids of the source peaks and of the baseline

(assumed to be at 0 MeV). A linear regression is then calculated:

$$E\ (MeV) = m \cdot x\ (channel) + q$$

where m, q are the angular coefficient and the intercept of the regression line respectively. Knowing the width of the peak (σ_x) and m, the energy resolution (FWHM=Full Width Half Maximum) can be obtained in this way:

$$\sigma_E = m \cdot \sigma_x \cdot 2\sqrt{2 \ln 2}$$

The mean values of the resolution for every telescope of the two stages are summarized in Table 5.1 and 5.2.

	baseline	^{239}Pu	^{241}Am	^{244}Cm
A x	0.012	0.171	0.164	0.157
A y	0.016	0.176	0.171	0.164
B x	0.016	0.154	0.150	0.143
B y	0.023	0.163	0.149	0.146
C x	0.018	0.165	0.159	0.150
C y	0.017	0.170	0.161	0.152
D x	0.018	0.152	0.147	0.142
D y	0.019	0.156	0.149	0.145
E x	0.016	0.167	0.161	0.155
E y	0.024	0.159	0.154	0.147
F x	0.017	0.185	0.167	0.155
F y	0.020	0.179	0.164	0.150
whole ΔE stage	0.018	0.166	0.158	0.151

Table 5.1: Mean values of the resolutions for every ΔE telescope (MeV).

	baseline	^{239}Pu	^{241}Am	^{244}Cm
A x	0.082	0.193	0.177	0.168
A y	0.078	0.130	0.130	0.127
B x	0.099	0.171	0.165	0.161
B y	0.090	0.120	0.115	0.114
C x	0.106		0.264	0.194
C y	0.113		0.134	0.128
D x	0.076		0.114	0.113
D y	0.079		0.104	0.103
E x	0.087	0.147	0.147	0.149
E y	0.087	0.122	0.122	0.117
F x	0.070	0.116	0.119	0.122
F y	0.121	0.149	0.145	0.134
whole E_{res} stage	0.091	0.144	0.144	0.136

Table 5.2: Mean values of the resolutions for every E_{res} telescope (MeV). For the telescopes C and D a source without ^{239}Pu was used.

5.4 Time spectra of the PPACs

In this section we report some time spectra coming from the PPACs and their physical meanings.

5.4.1 Cathode A

Fig. 5.5 shows the self-coincidence peak of cathode A of the first PPAC. It is very narrow, just 3 channels, because the same signal triggers the acquisition and, after being delayed, is revealed by the TDC.

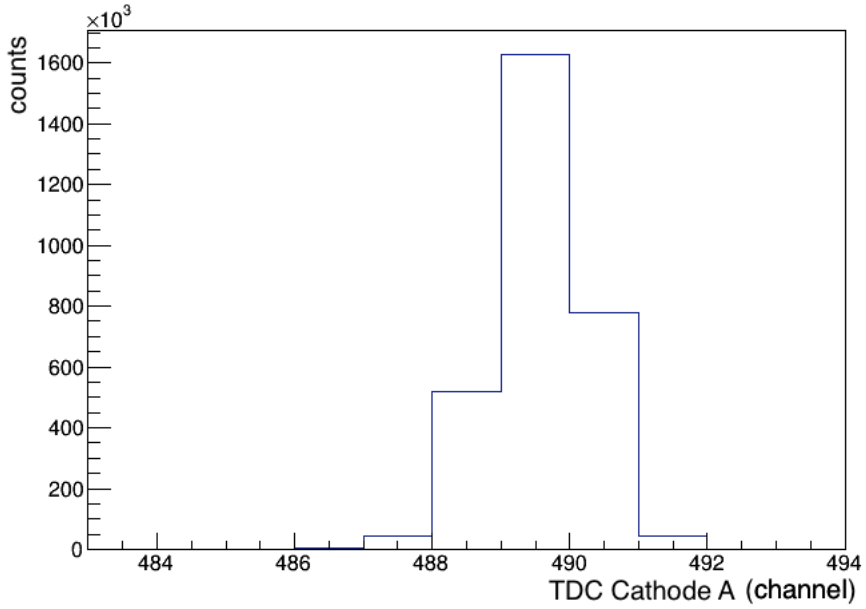

Figure 5.5: TDC Cathode A spectrum for the energy E_1.

5.4.2 Cathode B

Fig. 5.6 shows the time spectrum of cathode B of the second PPAC. Its width is much larger than the previous one, ∼40 channels, because of the difference in time of flight of the particles. The distance between the two PPACs is 544 mm and the particles have a velocity of $\beta \sim 0.1$, so the time of flight is of the order of 10 ns. The width of this peak reflects the energy resolution of the secondary beam produced.

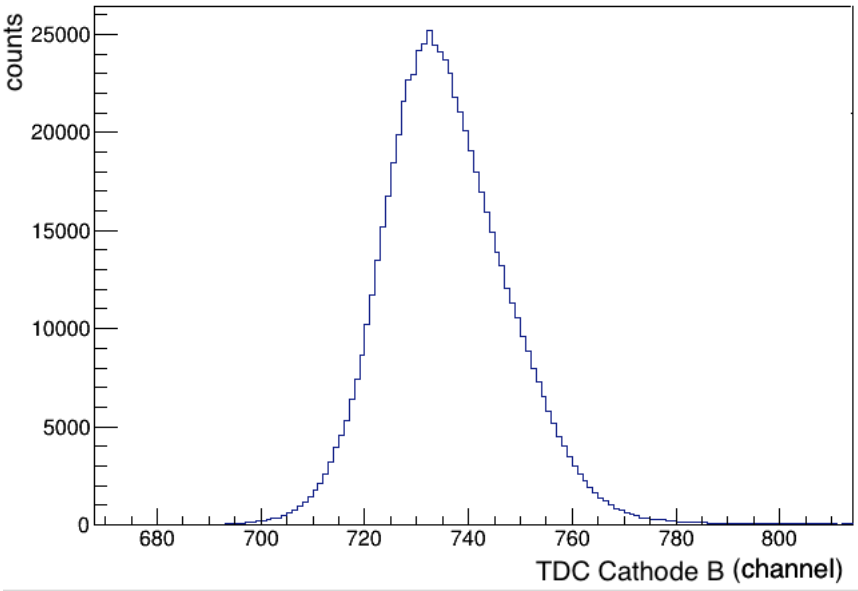

Figure 5.6: TDC Cathode B spectrum for the energy E_1.

5.4.3 Cathodes A-B correlation plot

Before being calibrated, the data collected during the experiment have to be sorted, i.e. we have to remove all non-physical events (pulser signals on the ΔE and E_{res} detector, noise, ...). At first we put a gate on the cathodes A and B of the two PPACs (see Fig. 5.7): we have to select only the events that show a correlation between the time signal seen by the two detectors. However, setting

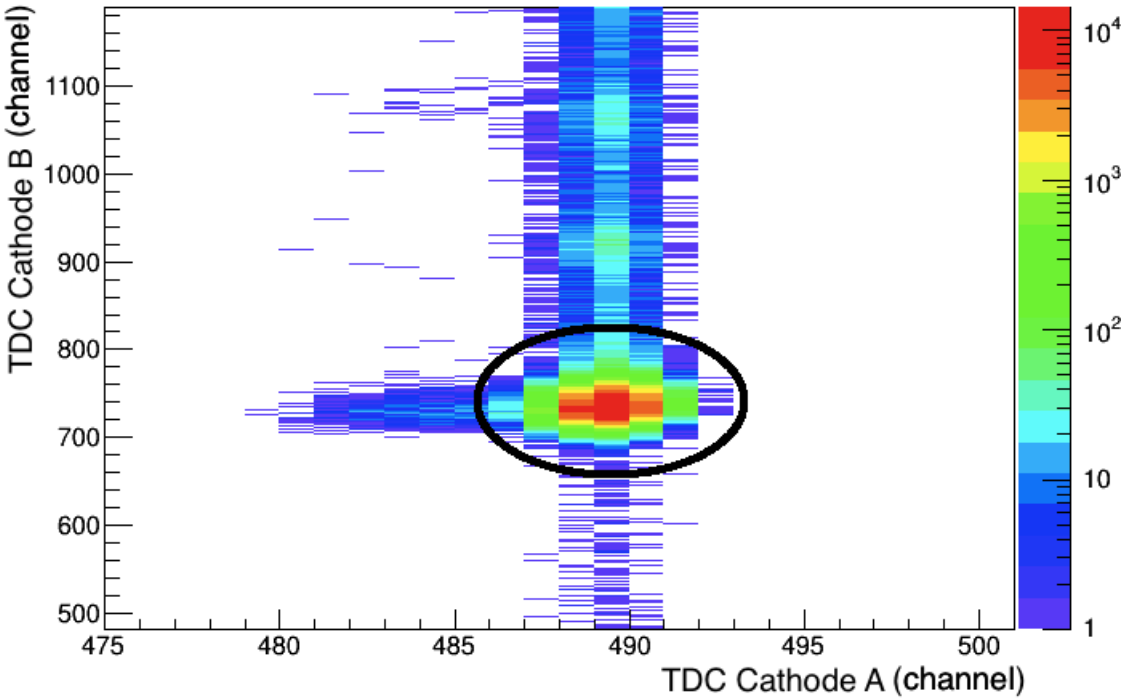

Figure 5.7: TDC cathode A vs TDC cathode B for the first energy (E_1). The gate has been put around the red dot, where we have indication of a physical correlation.

this condition does not prevent from collecting PULSER events because there is the possibility that a physical event triggers the acquisition (which is kept opened for $\Delta t = 1\ \mu s$) but at the same time a PULSER event occurs. The frequency of these random coincidences is given by

$$\nu_{rand} = \nu_{PULSER} \cdot \nu_{PPAC} \cdot 2 \cdot \Delta t = 300\ kHz \cdot 2\ kHz \cdot 2 \cdot 1\ \mu s = 1.2\ Hz$$

So the PULSER events must be removed in another way, by identifying them in a time-energy spectrum and setting a condition that excludes them, as we will see in section 5.5.1 (Fig. 5.14).

5.4.4 PPAC A coordinates

In Figs. 5.8-5.9 the spectra of the coordinates from the PPAC A have been reported. In the first one we can see clearly the 1 mm spacing of the wires. In the 2D plot the points lie on a line forming an angle of about $-45°$ with the x axis because the same physical signal is measured on the right side and on the left side after two delay lines, so the sum of these delays ΔT_{x1A} and ΔT_{x2A} must be constant ($= 150\ ns$).

Table 5.3 reports the efficiency values of the single coordinates for PPAC A.

coordinates	E_1 efficiency (%)	E_2 efficiency (%)
total events	166441	58090
x_{1A} left A	163242 (98.1%)	57384 (98.8%)
x_{2A} right A	159655 (95.5%)	56376 (97.0%)
x_A	156558 (94.1%)	55008 (94.7%)
y_{1A} up A	69243 (41.7%)	25413 (43.7%)
y_{2A} down A	59739 (35.9%)	21326 (36.7%)
y_A	53514 (32.2%)	19296 (33.2%)

Table 5.3: Efficiency values for the coordinates of PPAC A.

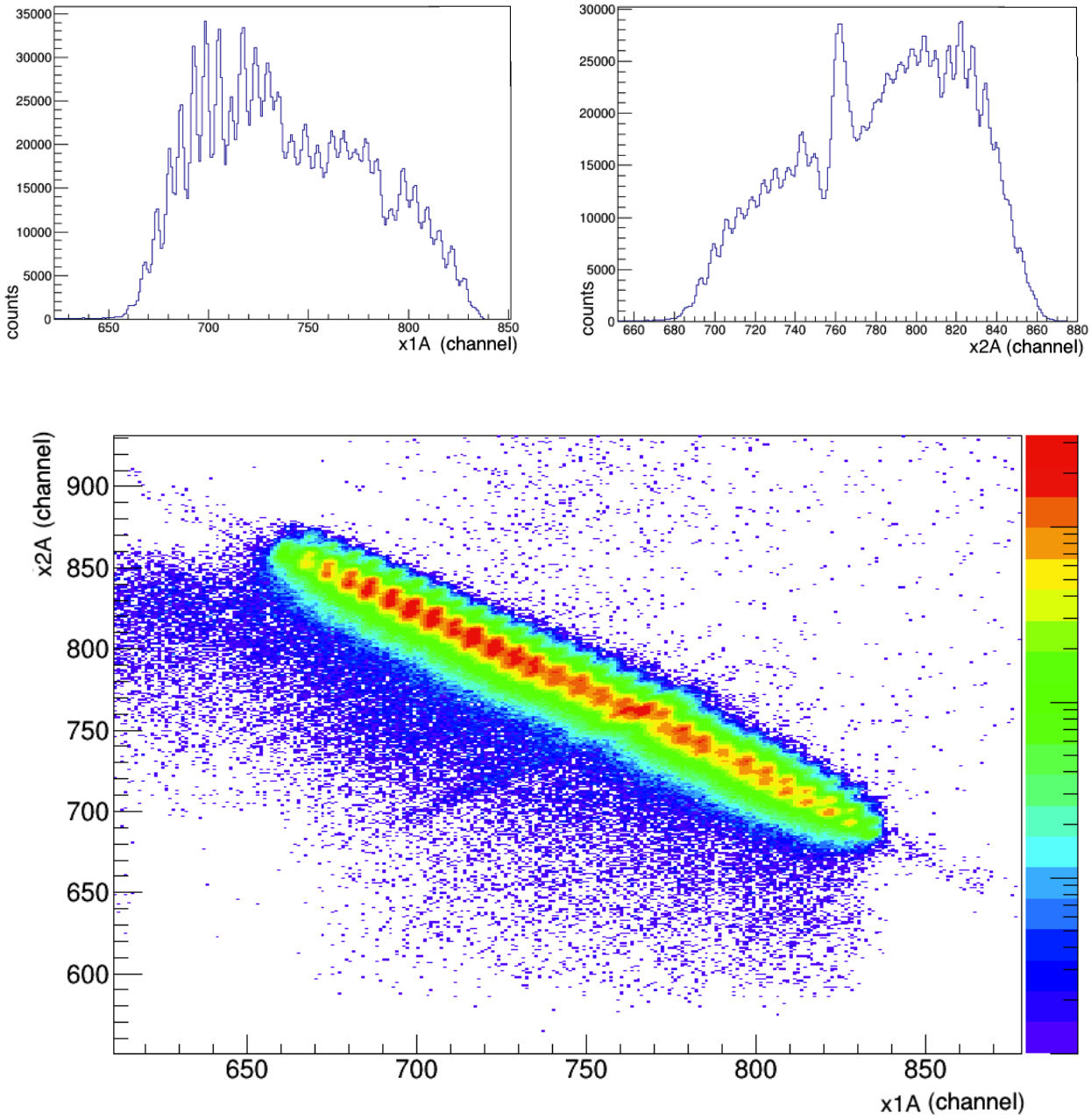

Figure 5.8: Spectra of the two horizontal coordinates of the PPAC A and the corresponding 2D plot (E_1).

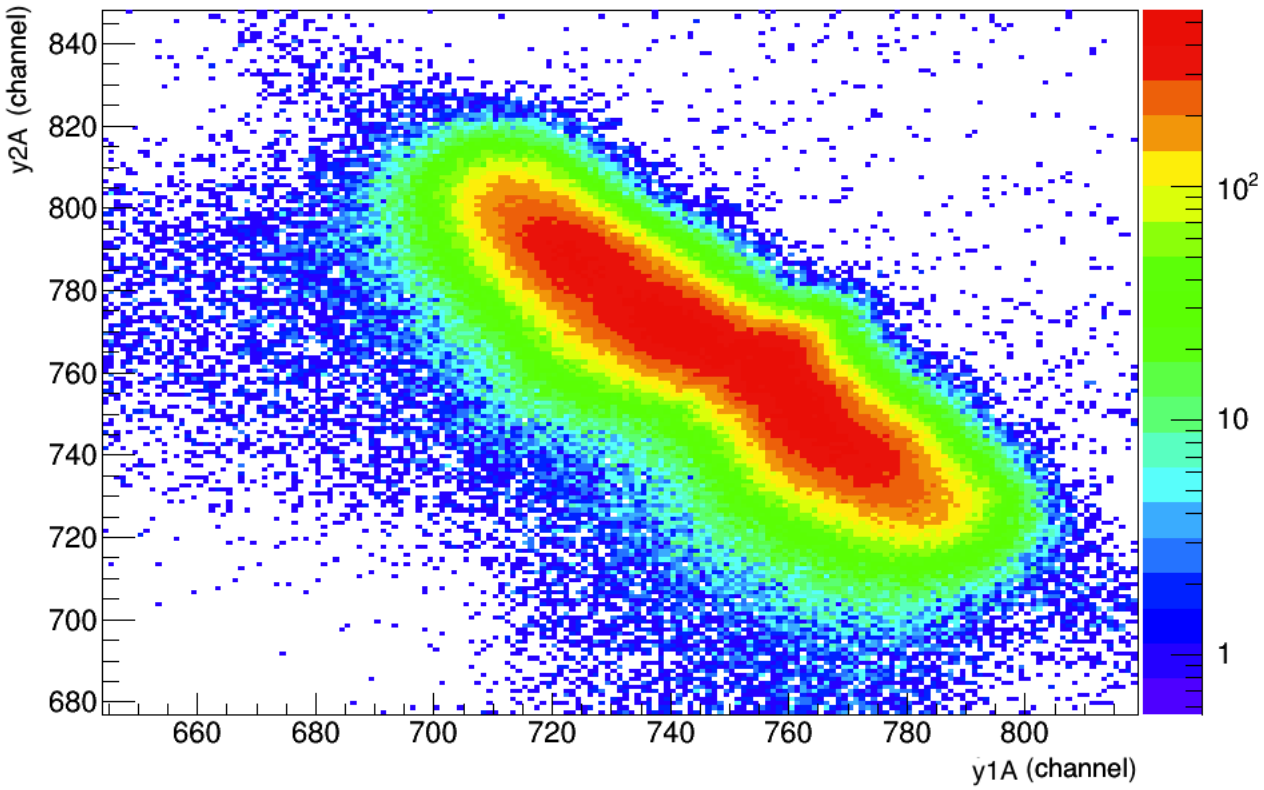

Figure 5.9: 2D plot of the two vertical coordinates of the PPAC A (E_1). In this case the single wires are not visible because of the bad resolution.

5.4.5 PPAC B coordinates

In Figs. 5.10-5.11 the spectra of the coordinates from the PPAC B have been reported.

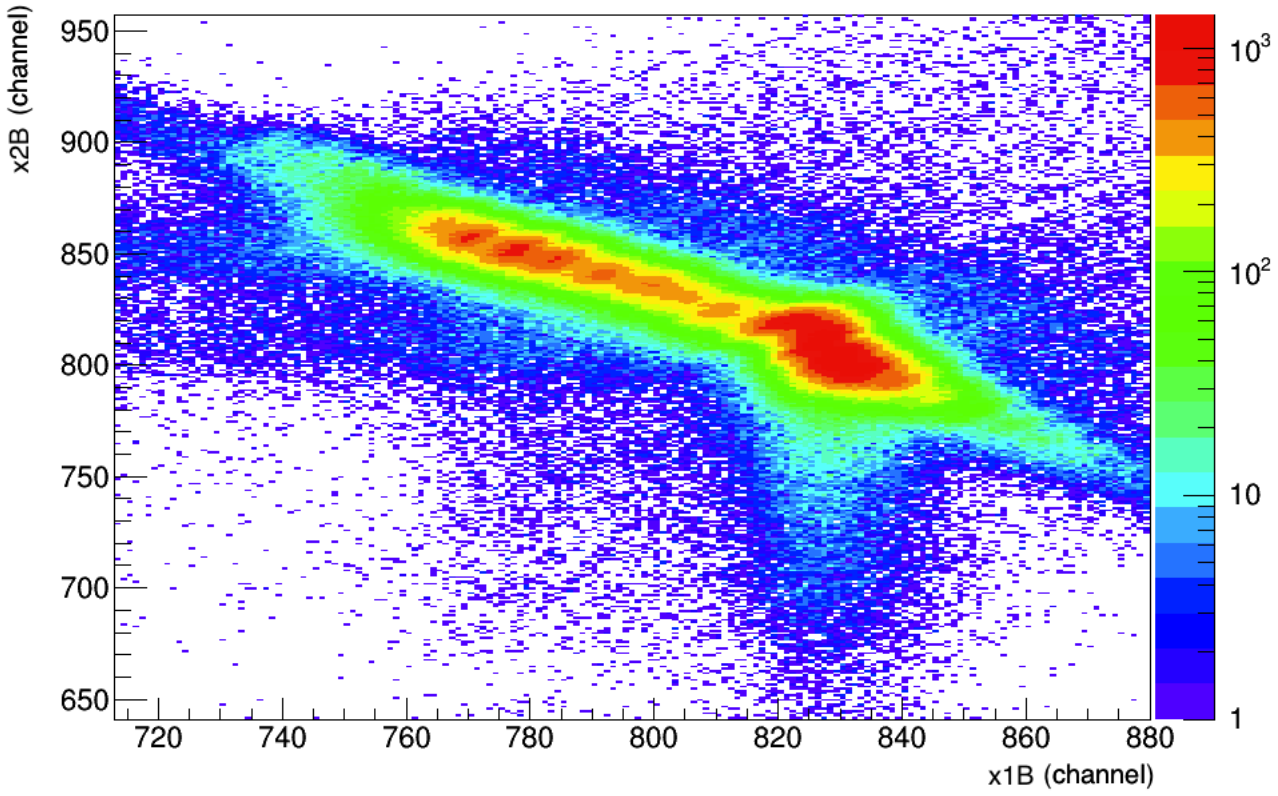

Figure 5.10: 2D plot of the two horizontal coordinates of the PPAC B (E_1).

Table 5.4 reports the efficiency values of the single coordinates for PPAC B. Since both PPACs showed limited efficiencies through the experiment, we decided not to use the tracking information provided by these detectors. This problem is probably related to the low Z, high velocity and high intensity of the ^{7}Be beam. We remark that this was the first experiment where the PPACs were used in these conditions. Earlier experiments were always performed with either heavier beams (^{8}B, ^{17}F) or lower energies (^{7}Be at 22.0 MeV) or lower intensities ($10^3 - 10^4$ pps).

coordinates	E_1 efficiency (%)	E_2 efficiency (%)
total events	166441	58090
x_{1B} left B	69980 (42.0%)	36464 (62.8%)
x_{2B} right B	81594 (49.0%)	40552 (69.8%)
x_B	64778 (38.9%)	34832 (60.0%)
y_{1B} up B	30875 (18.6%)	26138 (45.0%)
y_{2B} down B	59739 (48.9%)	21326 (79.5%)
y_B	30114 (18.1%)	25679 (44.2%)

Table 5.4: Efficiency values for the coordinates of PPAC B.

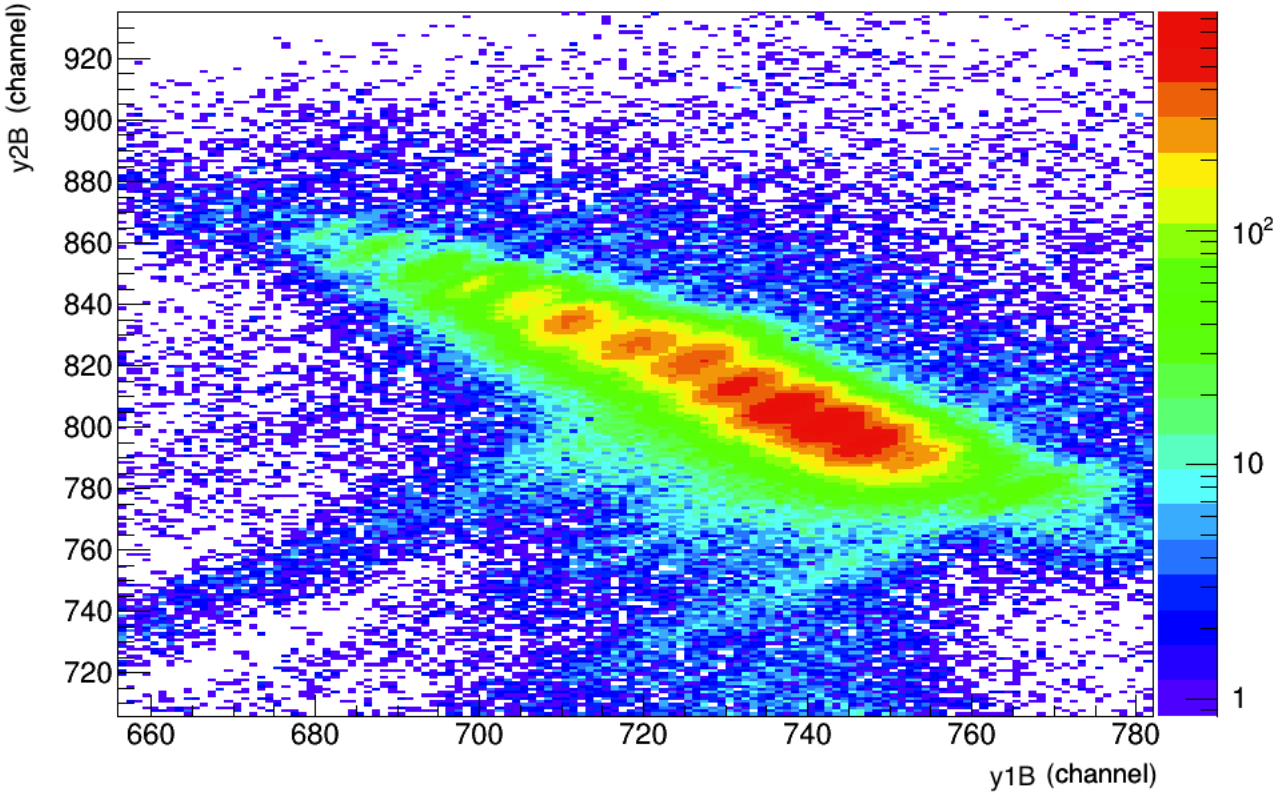

Figure 5.11: 2D plot of the two vertical coordinates of the PPAC B (E_1).

5.5 Selection gates

Now we will describe the sequence of selection gates applied to the collected data in order to remove all the non-physical events from the plots.

5.5.1 PULSER removal

The first step was the removal of PULSER events. To remove these events we applied a gate in the energy-rise time spectrum of a strip of the ΔE stage detector (see Fig. 5.12). Since the PULSER signal is sent simultaneously to all strips, in this way we remove almost all the PULSER signals.

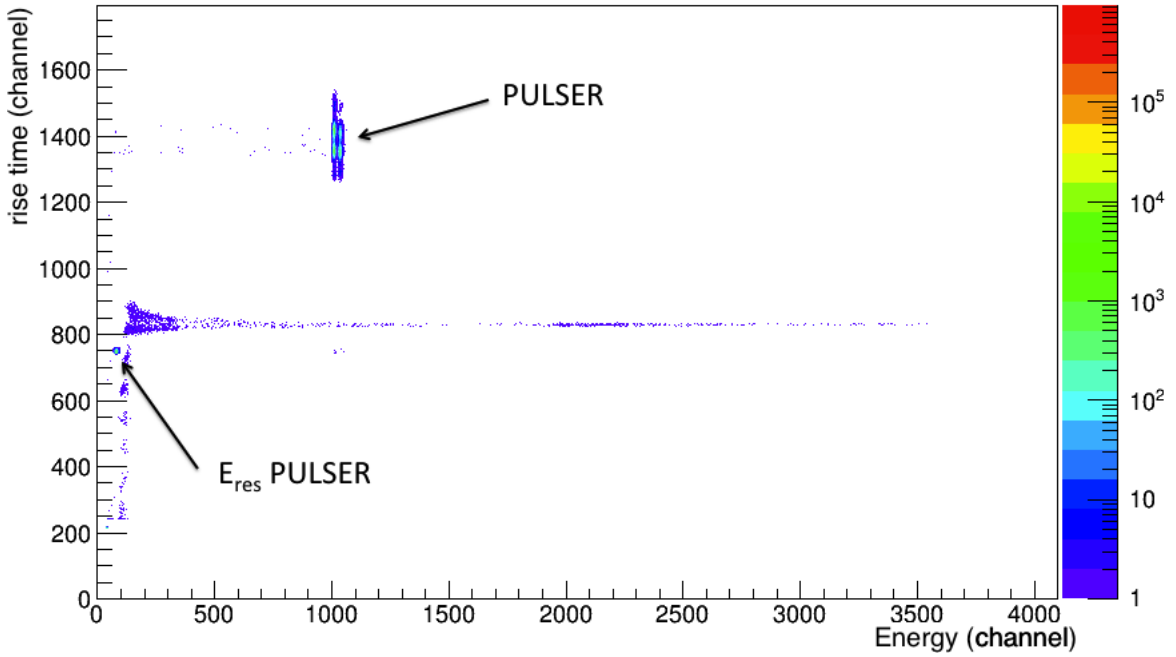

Figure 5.12: Exemple of energy-rise time matrix (E_1) from the ΔE stage. The PULSER and E_{res} PULSER events are indicated.

5.5.2 E_{res} PULSER removal

The E_{res} PULSER events can be seen in Fig. 5.12 concentrated in a small region on the left side of the plot. Similarly to the previous case, we applied a gate around these points and removed the corresponding events from all the strips.

5.5.3 Cathodes A-B selection

At this point we could put a gate for the events that showed a correlation between the time signal seen by the two PPACs as already described in Sec. 5.4.3.

While analyzing the data of the experiment we observed that almost 4/5 of the events seen by the B cathode were recorded as zeros. These signals are amplified twice and then sent to the MEGAMP, that has a certain threshold, and finally the signal, transformed from a negative pulse to a square logic signal positive shape, is collected by the TDC. This problem might be due to the fact that at high energies the ^{7}Be particles lose very little energy in the detector, so their signals could be below the

CDF threshold internal to the MEGAMP. Moreover, at the end of the experiment we realized that the PPAC B cathode got ruined, especially the thin aluminum layer deposited on the cathode. The resistivity of the place increased by more than 3 orders of magnitude, making it almost an insulating plate. This problem might be due to high intensity of the secondary beam or to insufficient gas flowing and has to be further investigated.

5.5.4 ΔE energy-time of flight selection

After removing the PULSER events and putting the condition on the cathodes of the PPACs, we considered only the events in the energy-time of flight plots associated to direct reactions. The events resulting from direct reactions are disposed in a narrow region (around the TOF channel 2700) since all these events occur in a short time interval (few ns, remember that 4096 channels correspond to 1 μs); the thick vertical band near the y axis in Fig. 5.13 is due to "baseline events" and the other events are evaporated protons, direct reaction products or ^{7}Be decay products.

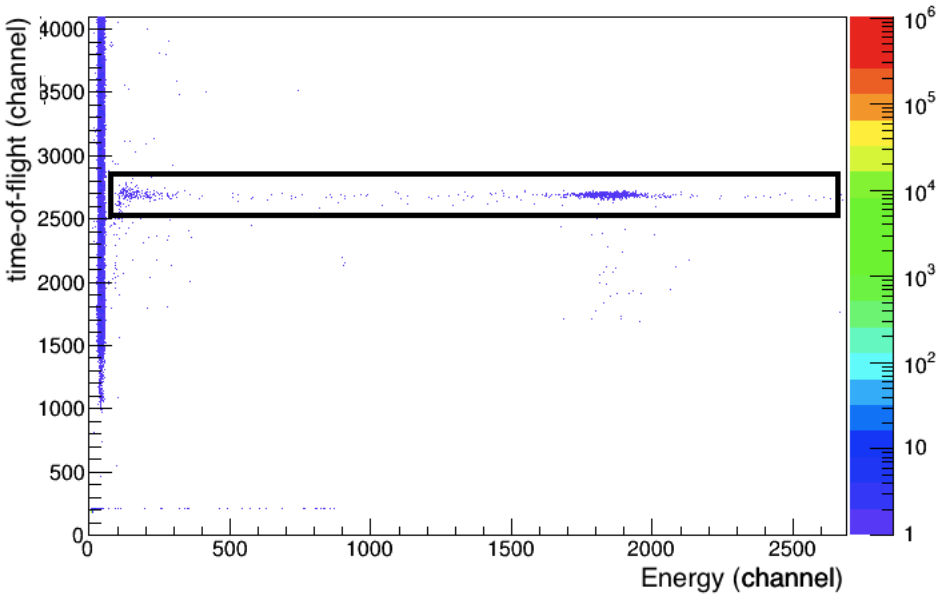

Figure 5.13: Example of energy-time of flight matrix (E_1) from the first two horizontal strips of the telescope A of the ΔE stage. We can distinguish the baseline (the thick band near the y axis), the protons (on the left side of the gate) and the elastic events (on the right side).

5.5.5 ΔE energy-rise time selection

Finally we considered only the good events in energy-rise time plots, i.e. the events indicated with a contour in Fig. 5.14

Applying these conditions step by step we calculated the percentages of elastic events, for the x strips, remained after each selection for each telescope. In Tables 5.5 and 5.6 we report the values obtained for E_1 and E_2, respectively. The efficiencies of the telescope F are lower than the others, probably because of some problems of the CFDs or its proximity to the beam. In the successive analysis we took into account this issue.

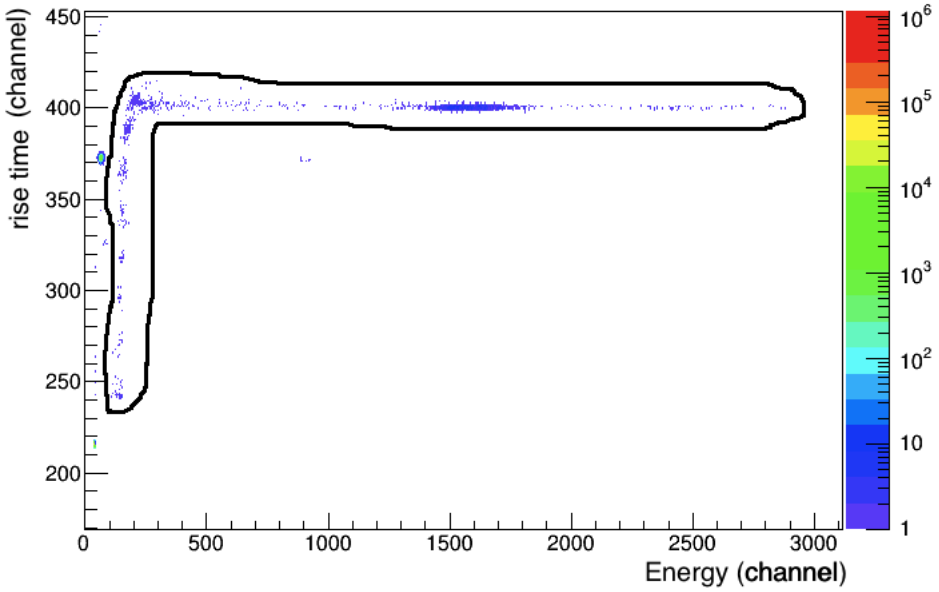

Figure 5.14: Example of energy-rise time 2D plot (E_1) from the first two vertical strips of the telescope A of the ΔE stage.

	No PULSER	No E_{res} PULSER and CAT A & CAT B selection	energy-time of flight selection	energy-rise time selection
A x	100.0%	95.9%	96.3%	100.0%
B x	100.0%	96.4%	95.8%	99.7%
C x	99.8%	95.6%	95.4%	100.0%
D x	100.0%	96.0%	95.9%	100.0%
E x	100.0%	95.6%	96.3%	100.0%
F x	100.0%	90.8%	90.4%	85.0%

Table 5.5: Percentages of elastic events, for the x strips, remained from each selection for each telescope (E_1). The percentages of each column are calculated with respect to the previous one.

	No PULSER	No E_{res} PULSER and CAT A & CAT B selection	energy-time of flight selection	energy-rise time selection
A x	100.0%	92.0%	96.3%	100.0%
B x	100.0%	93.8%	96.3%	99.5%
C x	100.0%	93.5%	94.5%	100.0%
D x	100.0%	92.4%	95.6%	100.0%
E x	100.0%	92.9%	96.9%	100.0%
F x	100.0%	87.5%	91.3%	87.5%

Table 5.6: As of Table 5.5 for E_2.

5.6 Multiplicity filters

Once the strips have been calibrated, we have to associate a *multiplicity* to each event, i.e. we have to determine the number of strips simultaneously fired. Considering, for example, a vertical (x) strips of the ΔE detectors of the A telescope, we can expect that the multiplicity $m_{Ax}^{\Delta E}$ associated to an event can range from 0 (no detection) to 1 (pure elastic scattering event), 2 (interstrip event or breakup process), ..., 16 (pulser event sent to all the strips at the same time). In this process, we set a threshold of 0.2 MeV in the spectra of the ΔE strips, which is considerably higher than the noise level, in order to avoid it.

We can associate a multiplicity to each side of the ΔE detectors:
$m_{Ax}^{\Delta E}$, $m_{Bx}^{\Delta E}$, $m_{Cx}^{\Delta E}$, $m_{Dx}^{\Delta E}$, $m_{Ex}^{\Delta E}$, $m_{Fx}^{\Delta E}$,
$m_{Ay}^{\Delta E}$, $m_{By}^{\Delta E}$, $m_{Cy}^{\Delta E}$, $m_{Dy}^{\Delta E}$, $m_{Ey}^{\Delta E}$, $m_{Fy}^{\Delta E}$

an identical procedure can be applied also to the E_{res} stage:
$m_{Ax}^{E_{res}}$, $m_{Bx}^{E_{res}}$, $m_{Cx}^{E_{res}}$, $m_{Dx}^{E_{res}}$, $m_{Ex}^{E_{res}}$, $m_{Fx}^{E_{res}}$,
$m_{Ay}^{E_{res}}$, $m_{By}^{E_{res}}$, $m_{Cy}^{E_{res}}$, $m_{Dy}^{E_{res}}$, $m_{Ey}^{E_{res}}$, $m_{Fy}^{E_{res}}$.

The multiplicities reported in these four lines can be added up to get the total multiplicity associated to each telescope or stage. For example, $m_{A}^{\Delta E}$ can be obtained as $m_{Ax}^{\Delta E} + m_{Ay}^{\Delta E}$, and similarly for the other telescopes and for the E_{res} stage; then $m_A = m_A^{\Delta E} + m_A^{E_{res}}$ (and so on), while $m^{\Delta E}$ and $m^{E_{res}}$ are multiplicities associated to the whole stages and m^{array} is the multiplicity associated to the whole EXPADES array:
$m_{A}^{\Delta E}$, $m_{B}^{\Delta E}$, $m_{C}^{\Delta E}$, $m_{D}^{\Delta E}$, $m_{E}^{\Delta E}$, $m_{F}^{\Delta E}$,
$m_{A}^{E_{res}}$, $m_{B}^{E_{res}}$, $m_{C}^{E_{res}}$, $m_{D}^{E_{res}}$, $m_{E}^{E_{res}}$, $m_{F}^{E_{res}}$,
m_A, m_B, m_C, m_D, m_E, m_F, $m^{\Delta E}$, $m^{E_{res}}$, m^{array}.

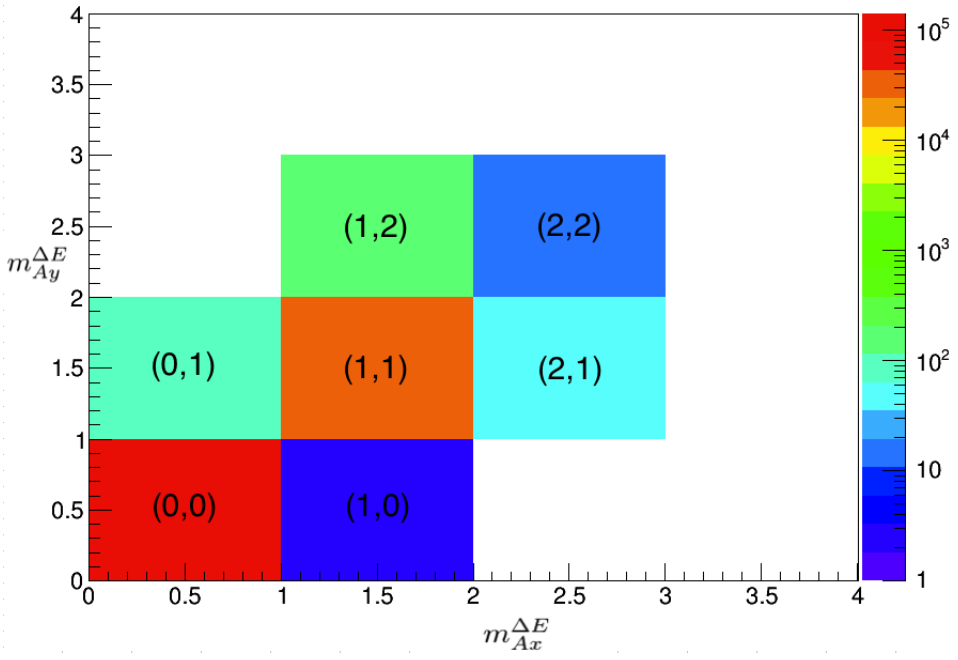

Figure 5.15: Example of multiplicity plot $m_{Ax}^{\Delta E}$-$m_{Ay}^{\Delta E}$.

The example reported in Fig. 5.15 shows a $m_{Ax}^{\Delta E}$-$m_{Ay}^{\Delta E}$ plot. The multiplicities filter that we applied retain only the events with multiplicities $(1,1)$, $(2,1)$, $(1,2)$, $(2,2)$; $(1,1)$ multiplicities are associated to particles that hit both the x and y side of the telescope, $(2,1)$, $(1,2)$ are interstrip events and $(2,2)$ are coincidence events, i.e. two particles were detected at the same time. In this work of thesis we considered only the $(1,1)$ events, which are more than 99% of the physical events, the other ones will be the subject of a successive analysis.

5.6.1 $E_x - E_y$ filters

Finally, for the ΔE stage the last filter was set on the $E_x - E_y$ plots to consider only the events with the same recorded energy on the x and y strips, i.e. the events lying along the diagonal of the plot shown in Fig. 5.16. In this way we retained the 97.3% of the events for E_1 and the 97.5% for E_2. Events off-diagonal are particles that hit the first x strip or y strip (points above or below the diagonal, respectively) and are affected by a phase-shift in the multiplexed signal read-out sequence. This bug was fixed in January 2015, but it is not a problem for our analysis because at least one of the energy signal is suitable for our analysis.

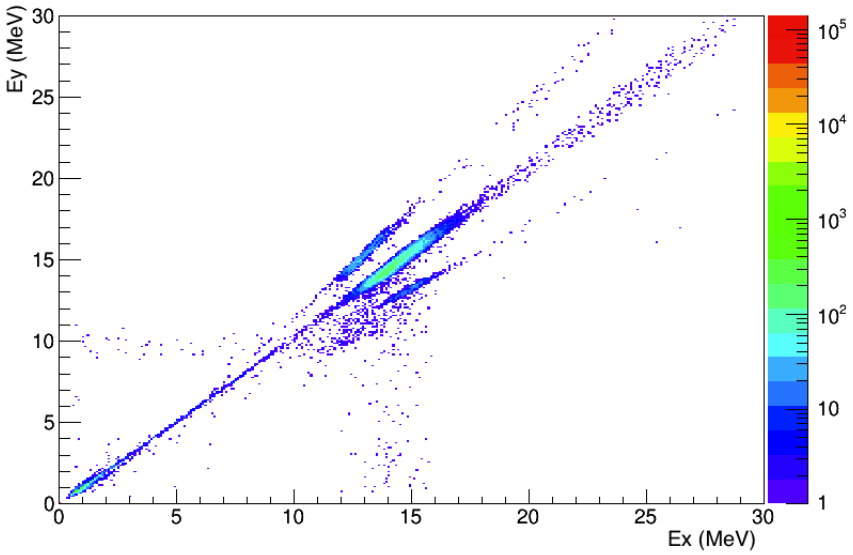

Figure 5.16: Example of $E_x - E_y$ plot. For the events off-diagonal, which have different x and y energy values, we used only one of the two energy signals.

5.6.2 Misalignment correction

To evaluate the overall efficiency of the experimental setup and to extract the quasielastic angular distribution, we developed an ad hoc Monte Carlo code. The code took into account: (i) the kinematics of the elastic scattering process, (ii) the Rutherford cross section, (iii) the geometry of the detector array EXPADES, (iv) the secondary beam energy spread (v) the secondary beam spot on target (vi) the energy loss within the whole target thickness, and (vii) the experimental energy resolution.

In the simulation a random interaction point along the whole target thickness was assumed event by event and the kinetic energy of the incoming particle was decreased according to the distance covered inside the target. The normalization of the simulated data was performed by requiring that the

integrated areas under the elastic peak corresponded to the experimental values at the most forward angles, where the differential cross section is expected to be purely Rutherford at both secondary beam energies.

We used this simulation program also to evaluate the alignment of the plate where the detectors were placed. The system was built in a symmetric configuration, however a small misalignment angle could be present. Observing how the ratio of the number of detected elastic events with respect to the simulated elastic events changes as a function of this tilting angle for the forward detectors A and D (Figs. 5.17- 5.18) we got the correct tilting angle observing where the intersection between the two lines occurs. The two lines in Figs. 5.17- 5.18 have different slope because what we did is rotating the plate where the detectors were placed, so the counts on the left and right side change according to the number of events predicted by the simulation for each strip.

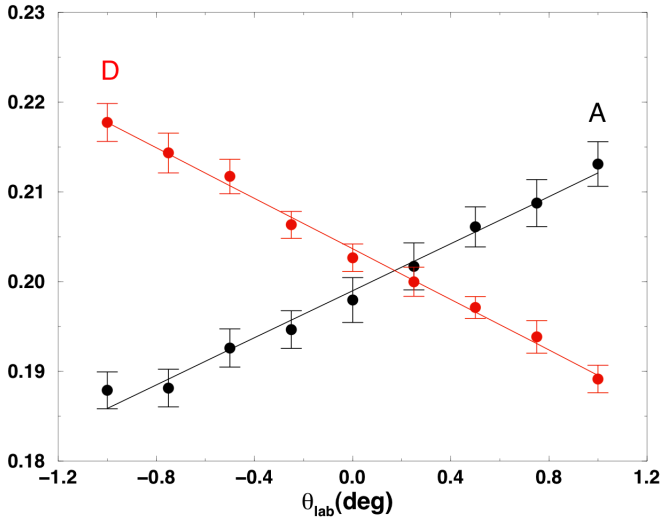

Figure 5.17: Ratio of the number of detected elastic events with respect to the simulated elastic as function of the tilting angle for telescope A (black) and D (red) for energy E_1; the intersection of the corresponding regression lines gives the correct tilting angle.

In this way we determined that the tilting angles, calculated for each energy of the beam, were:

$$\theta_{E_1} = 0.172^\circ \pm 0.017^\circ$$

$$\theta_{E_2} = 0.173^\circ \pm 0.013^\circ$$

The associated errors are only the statistical errors derived from the regression lines, the systematic errors should be probably one order of magnitude greater. In this calculations we did not consider the marginal strips that can suffer from some shadow effects. The first two angles are fully compatible with each other since the same beam was used; the only difference, to change the energy from E_1 to E_2, was the insertion of a aluminum beam degrader (13.77 mm thick).

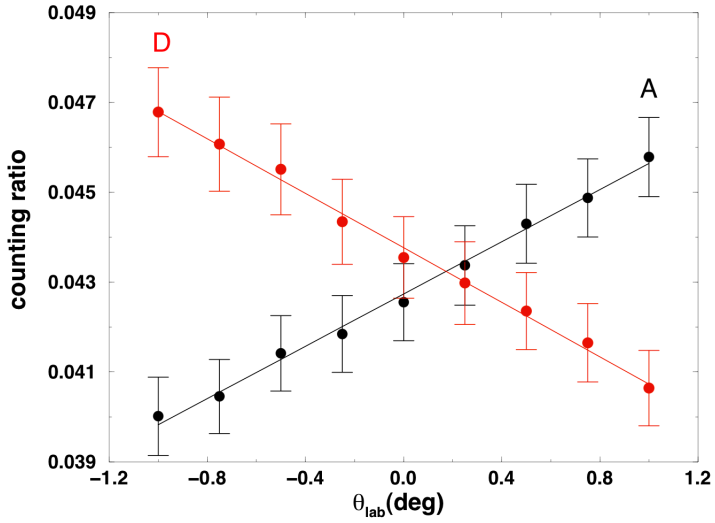

Figure 5.18: Same as Fig. 5.17 for energy E_2.

5.6.3 Correction of the target ladder thickness

Then we used the simulation program to find the correct value of the thickness of target ladder, which has a nominal value of 1 mm: for the two forward telescopes A and D we evaluated the ratios of the simulated and experimental elastic events with different values of the thickness and then we calculated the slope of these ratios for each strip with respect to the angles where the strips were.

In fact, particles scattered at angles around 90° could be intercepted by the target ladder, and this is more probable if they hit the target near the target frame. Therefore using the telescope A and D, where we expect to observe a ratio-to-Rutherfod near 1, we can determine the correct thickness by choosing the zero-slope curve. We performed these calculations for both beam energies and we found that the telescopes A and D exhibit different values of the thickness, maybe because of the tipping of the target ladder or because of the eccentric rotation of the plate where the detectors where placed (see Figs. 5.19-5.20).

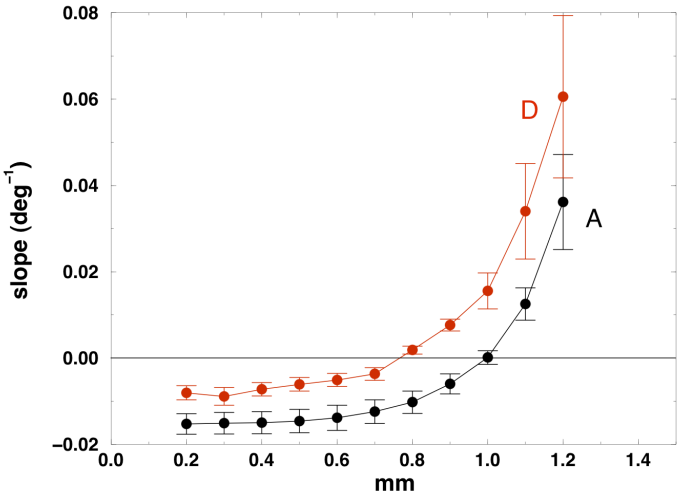

Figure 5.19: Slope of the ratios between simulated and experimental elastic events as a function of the target ladder thickness (E_1) for telescope A (black) and D (red). The intersections with zero give the correct values of the thicknesses as seen by the two telescopes.

These are the obtained values:

$$thickness_{A\ E_1} = 0.998 \pm 0.027\ mm$$

$$thickness_{D\ E_1} = 0.767 \pm 0.013\ mm$$

$$thickness_{A\ E_2} = 0.900 \pm 0.001\ mm$$

$$thickness_{D\ E_2} = 0.845 \pm 0.025\ mm$$

5.6.4 Evaluation of the energy of the beams

In order to evaluate the precise energies of the beams used in this experiment we used a monitor detector nominally placed at $\sim 27°$ with respect to the beam line. As we said in the previous section,

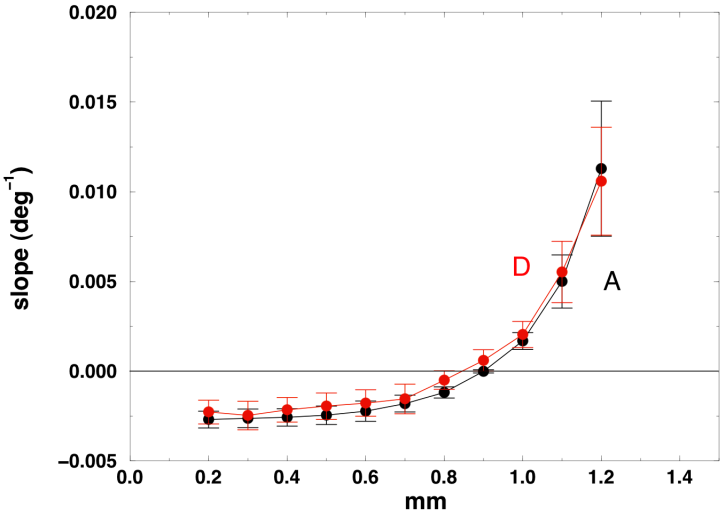

Figure 5.20: Same as Fig. 5.19 for energy E_2.

this angle must be corrected using the tilting values reported, depending on the energy of the beam. Using the α sources we performed a 3 points linear fit (with the baseline, the ^{241}Am and ^{244}Cm energy peaks). Since the target is 1 mg/cm^2 thick, we can deduce the energies of the beams emerging from the target considering the Rutherford scattering formula. Finally we assume that on average the scattering process occurs in the middle of the target, so the particles have to cross the second half target; using the simulation program LISE [8] we evaluated the energy losses. The values of the energy of the beams obtained through this process are the following:

$$E_1 = 40.65 \pm 0.36\ MeV$$

$$E_2 = 37.55 \pm 0.44\ MeV$$

5.7 ΔE $x-y$ correlation plots

We show in this section the ΔE $x-y$ correlation plots of strips x versus strips y, in this way we can immediately see the distribution of the elastic events in each telescope (Fig. 5.22-5.27); for the forward telescope A and D (Figs. 5.22 and 5.25) we can appreciate a hint of the Rutherford distribution, visible in the dropping of the number of events proceeding from left to right, that is from small to large scattering angles, while for the other telescopes no particular pattern is recognizable. The elastic events were selected putting a gate in the *strip* $y-E_y$ plots for each telescope (see an example in Fig. 5.21) where they form a narrow band located in the middle part.

In the plots we can see that there are some strips with very low counts compared to the others (i.e. the 15^{th} and 16^{th} y strips of telescope A, the 8^{th} y strip and the 16^{th} x strip of telescope B, the 14^{th} and 16^{th} x strips of telescope C, the 14^{th} and 16^{th} x strips and the 10^{th} y strip of telescope E, the 14^{th} x strip of telescope F). These strips are attenuated: the reason will be further investigated, maybe it depends on the strips themselves or on the preamplifier/amplifier.

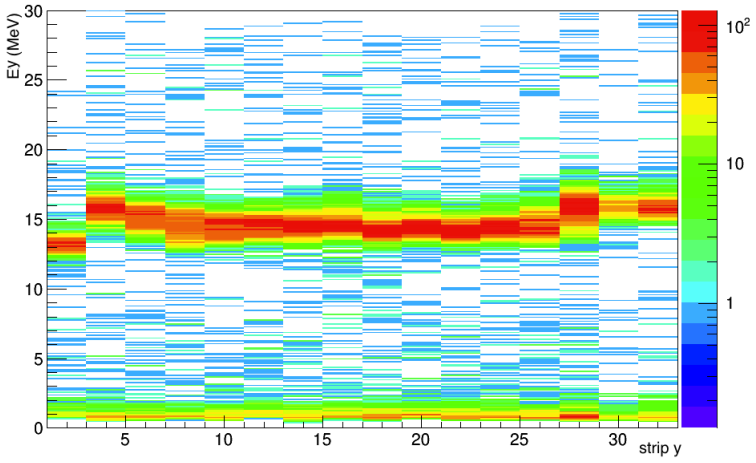

Figure 5.21: *strip* $y-E_y$ plot showing clearly the elastic events as a narrow band in the middle part of the image.

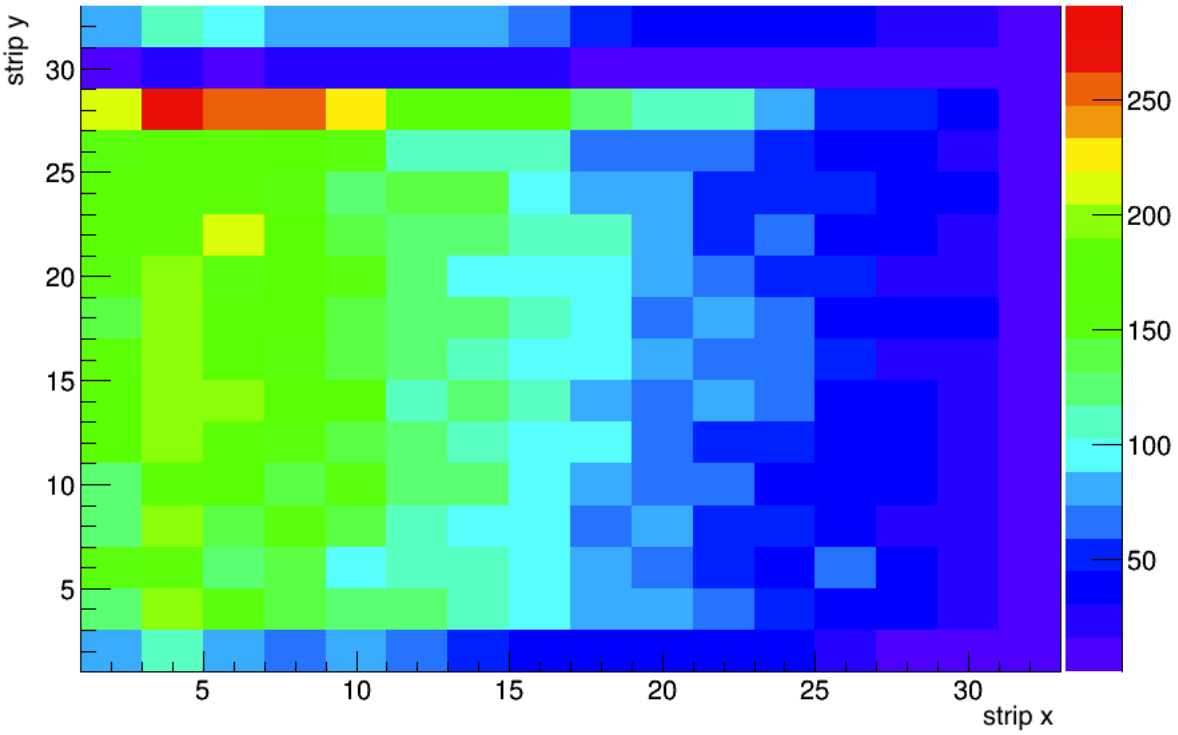

Figure 5.22: ΔE $x-y$ correlation plot of strips x vs strips y for telescope A.

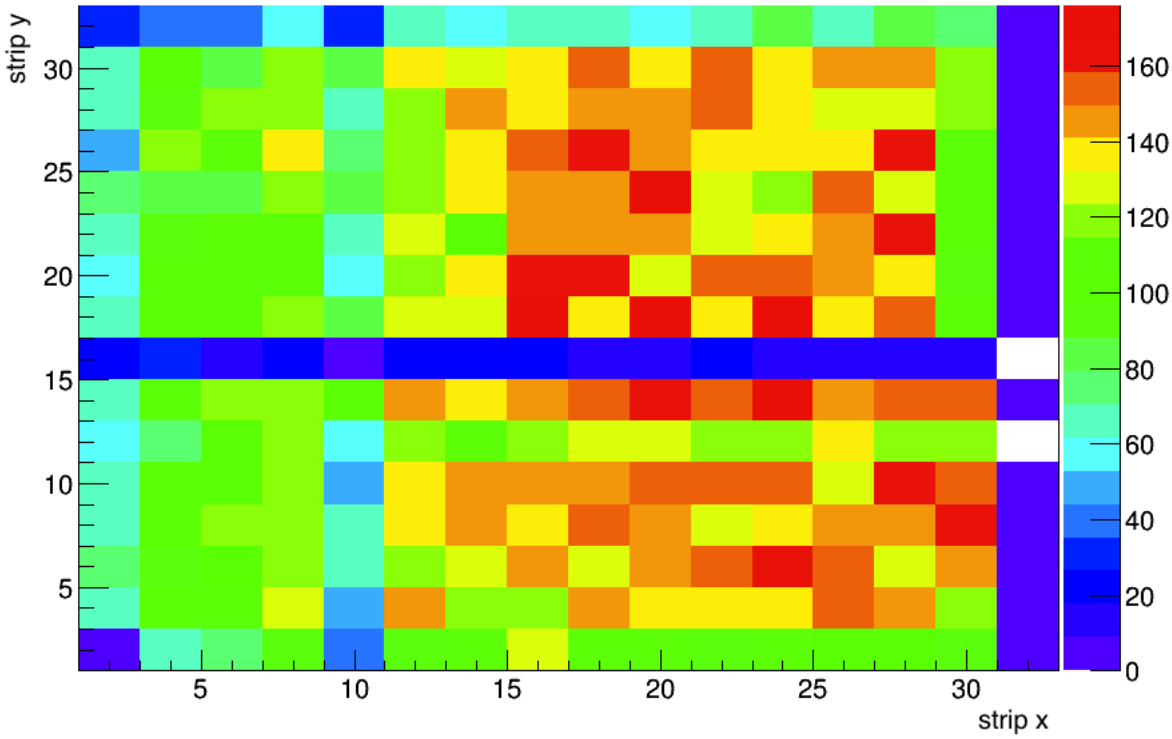

Figure 5.23: ΔE $x-y$ correlation plot of strips x vs strips y for telescope B.

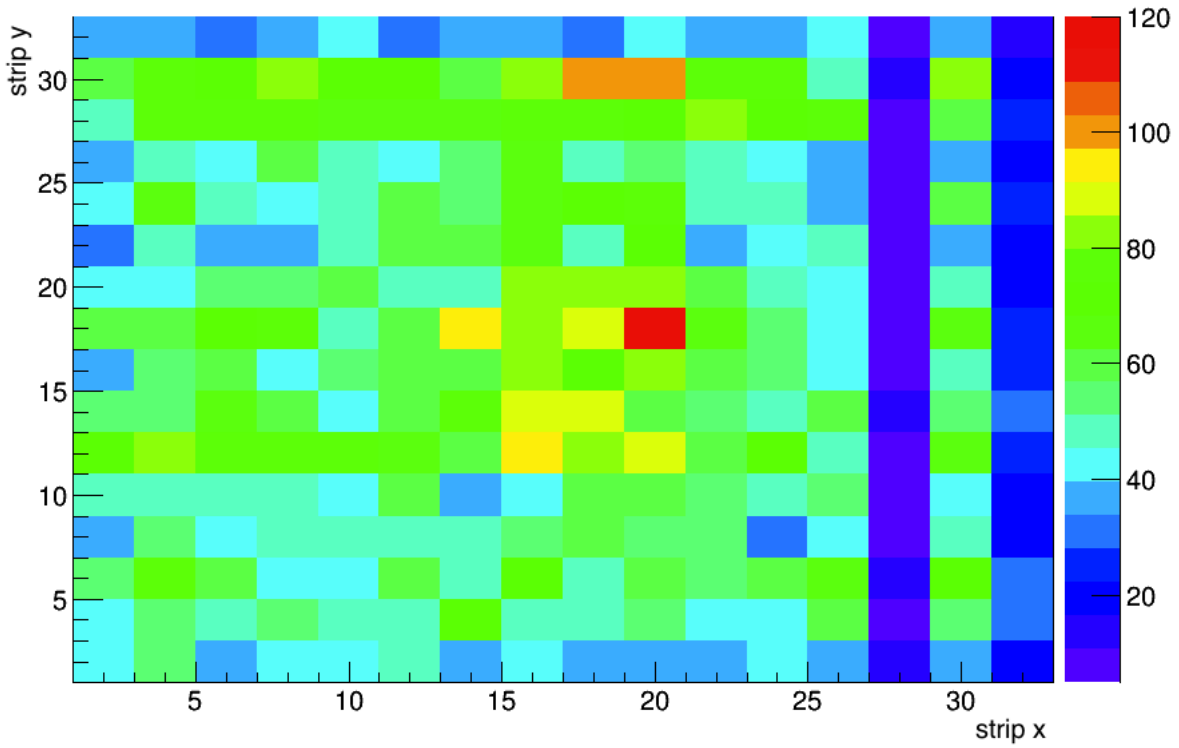

Figure 5.24: ΔE $x - y$ correlation plot of strips x vs strips y for telescope C.

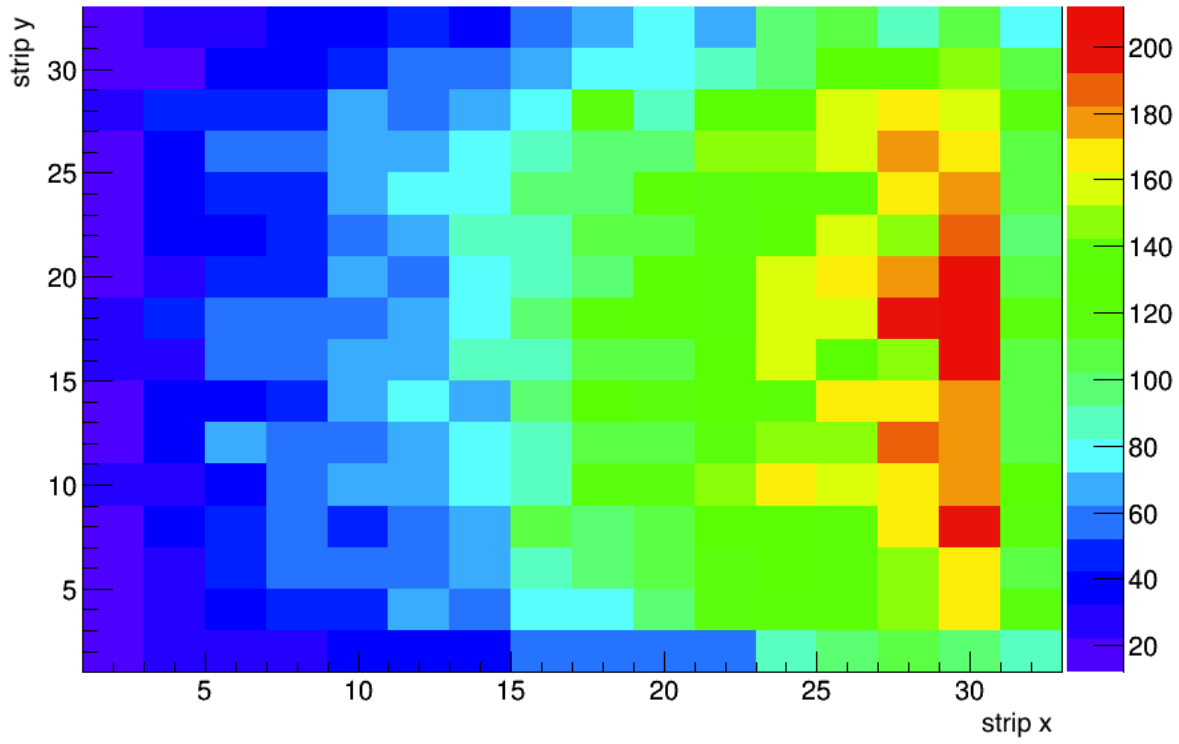

Figure 5.25: ΔE $x - y$ correlation plot of strips x vs strips y for telescope D.

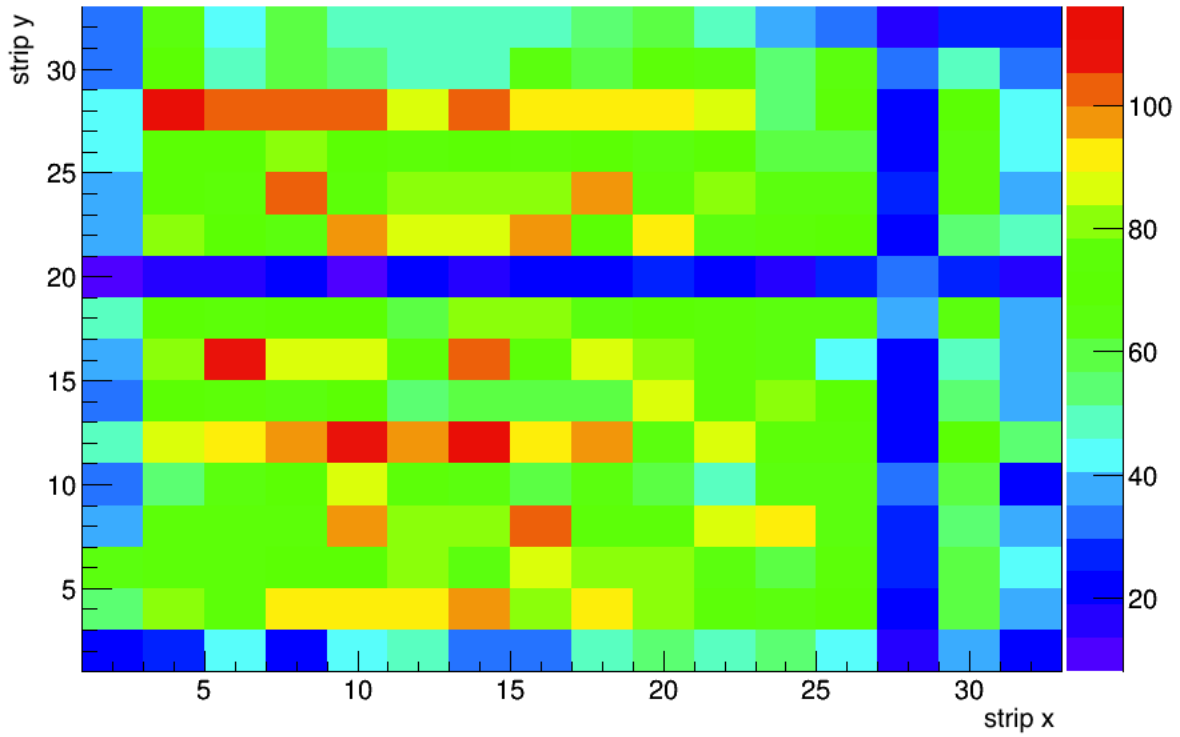

Figure 5.26: ΔE $x-y$ correlation plot of strips x vs strips y for telescope E.

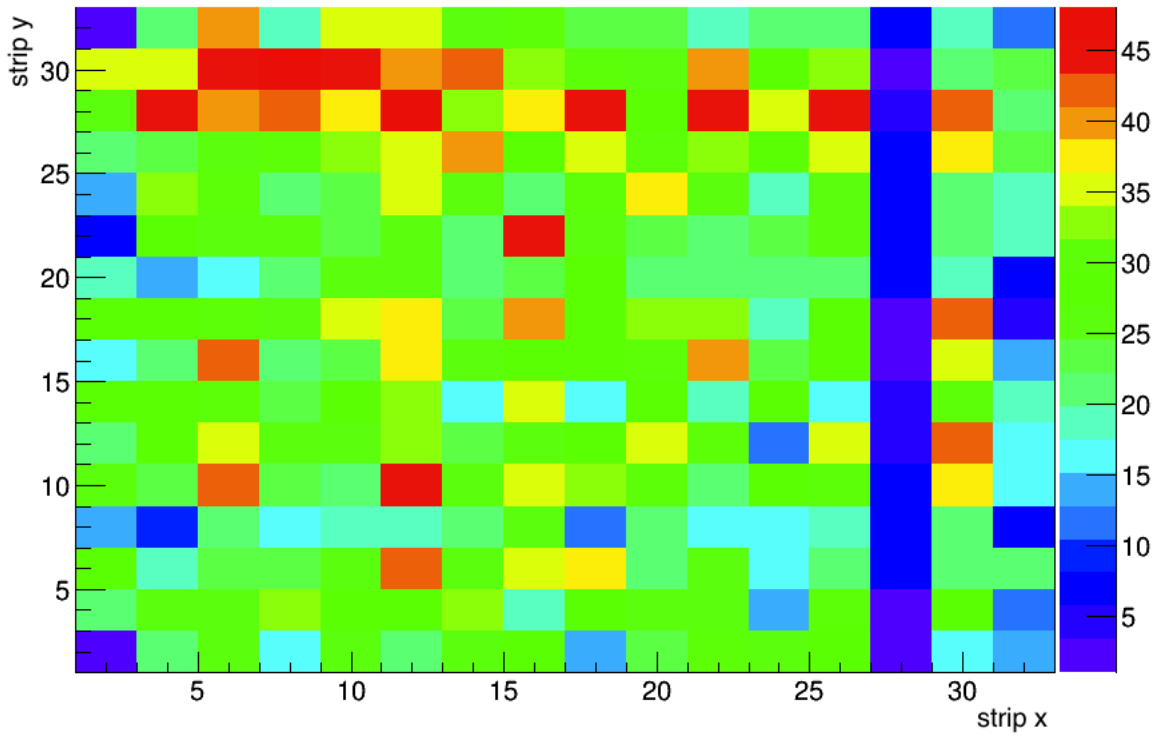

Figure 5.27: ΔE $x-y$ correlation plot of strips x vs strips y for telescope F.

5.8 Quasi-elastic scattering angular distribution (ΔE stage)

With the analysis of only the ΔE stage we were able to obtain a first evaluation of the angular distribution of quasi-elastic scattering events. We calculated the ratio to Rutherford for the different x strips of the ΔE detectors placed at different angles as the ratio between the number of measured elastic events and the simulated ones obtained using the simulation program and normalizing them with respect to the efficiencies of each telescope. For E_1 we obtained the angular distribution reported in Fig. 5.28; Fig. 5.29 report the same data but grouped into consecutive strips while in Fig. 5.30 data are also grouped averaging the ratios on the opposed side of the beam line. Figs. 5.31-5.33 report the same charts but for E_2.

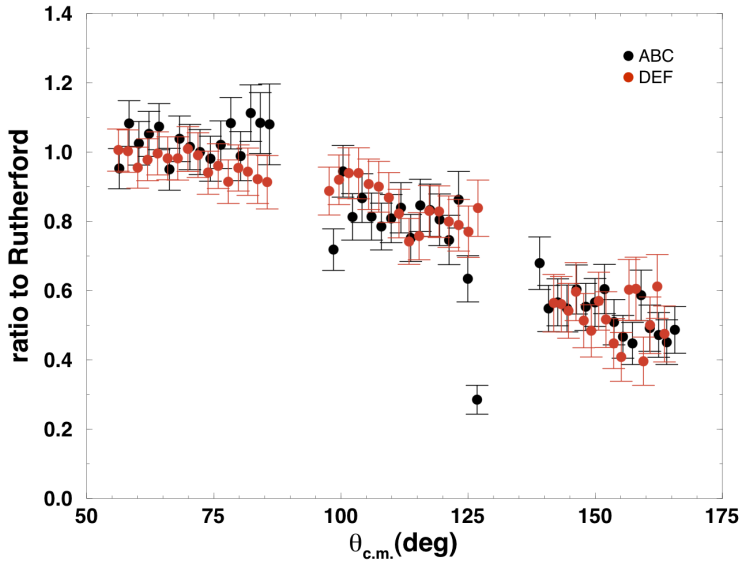

Figure 5.28: Quasi-elastic scattering angular distribution using the ΔE stage for E_1.

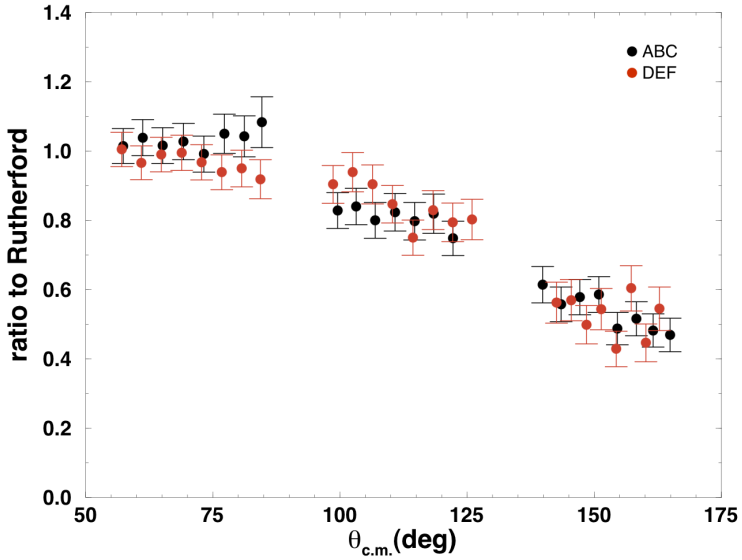

Figure 5.29: Quasi-elastic scattering angular distribution using the ΔE stage for E_1. Consecutive strips are grouped together.

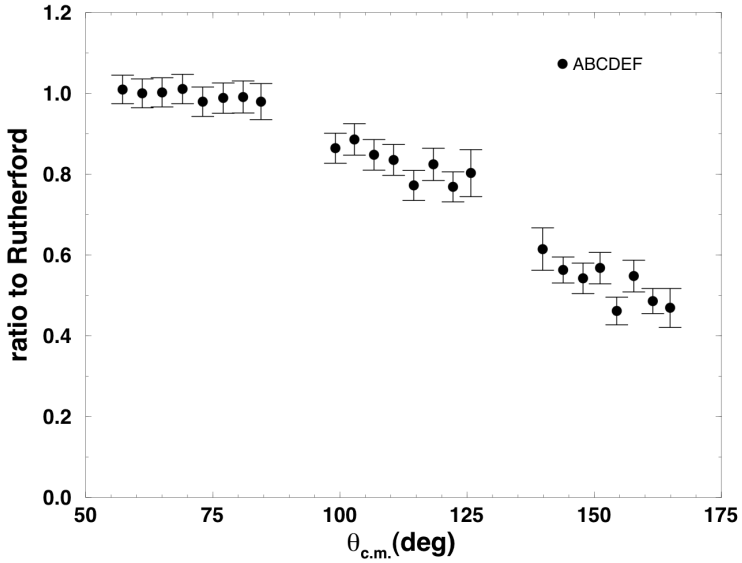

Figure 5.30: Quasi-elastic scattering angular distribution using the ΔE stage for E_1. Consecutive and opposed strips and grouped together.

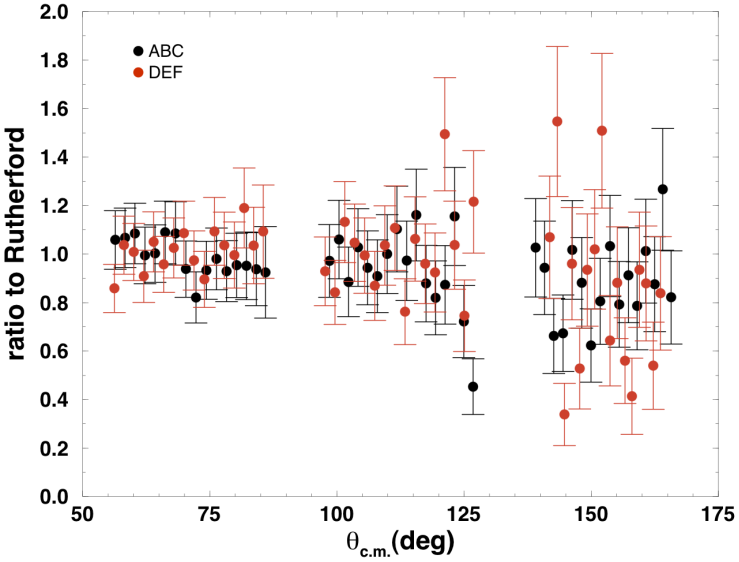

Figure 5.31: Quasi-elastic scattering angular distribution using the ΔE stage for E_2.

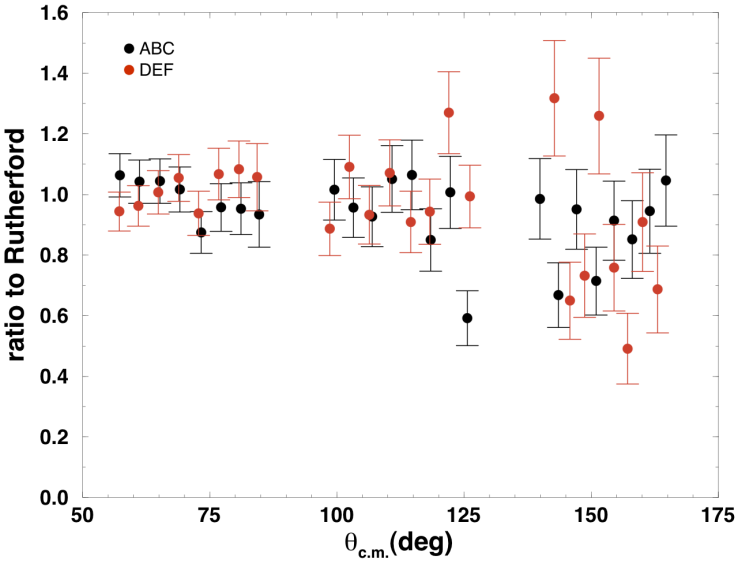

Figure 5.32: Quasi-elastic scattering angular distribution using the ΔE stage for E_2. Consecutive strips are grouped together.

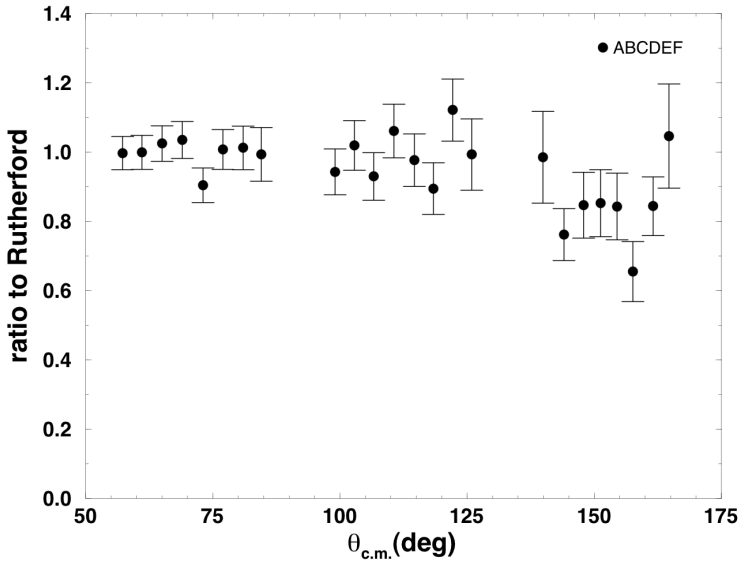

Figure 5.33: Quasi-elastic scattering angular distribution using the ΔE stage for E_2. Consecutive and opposed strips and grouped together.

5.9 $\Delta E - E_{res}$ analysis

In the last part of the data analysis we considered also the E_{res} stage, that let us identify unambiguously the different isotopes.

5.9.1 E_{res} multiplicity filter

Similarly to the multiplicity filter we applied to the ΔE stage, we discriminated the events with different multiplicities in the E_{res} stage. Then for each telescope we obtained the plots as the one reported in Fig. 5.34 where we have the y strips of the E_{res} stage vs the y strips of the ΔE stage, and we decided to remove all the events off-diagonal, i.e. the events that have uncorrelated positions in the ΔE and E_{res} stages. The diagonal is oriented at $-45°$ because the numbering of the strips of the ΔE stage and of the E_{res} stage are inverted.

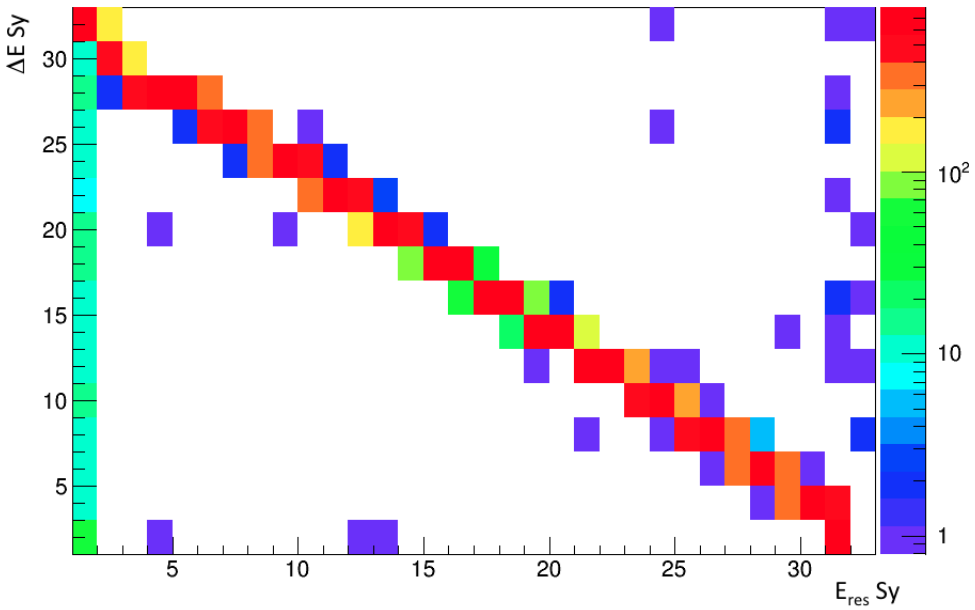

Figure 5.34: $E_{res} - \Delta E$ strips plot. Only the events on the diagonal were selected.

5.9.2 Baseline subtraction

The y strips in the E_{res} stage have opposed polarity with respect to the x strips, so for each strips we subtracted the position of the baseline, placed around the channel ~ 2000, the channel associated to each event. In this way the spectra of the E_{res} stage have the same orientation of the ΔE stage.

5.9.3 Not working strips removal

Some y strips of the E_{res} did not work during the experiment and they detected very few events or any at all. These strips have to be removed from the analysis in order to get the correct isotope selection and angular distribution (reported in the next sections). The not working strips are the following:
$Ay00$, $Ay13$, $Ay25$, $Ay26$, $Ay30$, $Ay31$,
$By00$, $By31$,

$Cy00$, $Cy01$, $Cy30$, $Cy31$,

$Dy00$, $Dy31$,

$Ey00$, $Ey31$,

$Fy00$, $Fy01$, $Fy07$, $Fy09$, $Fy31$.

All marginal strips ($Xy00$, $Xy31$, with X=A, ..., F) were removed because of incomplete charge collection and because they were also inducing noise in neighboring strips. Signals from strips $Ay13$, $Ay25$, $Ay26$, $Fy07$, $Fy09$ were absent while signals from the other removed strips were too noisy to be processed.

In total we had to remove only 21 vertical strips out of the 192 of the y E_{res} detector stage ($\sim 11\%$).

5.9.4 Isotope selection

At this point we can apply the $\Delta E - E_{res}$ correlation plot technique to identify the isotopes detected by the EXPADES array.

At the beginning of the experiment, the timing of the readout sequence for the E_{res} signal was optimized by changing the peak sampling time. This value was adjusted with alpha particles from standard calibration sources before the experiment, but needed to be modified according to the timing and shape of the ^{7}Be signals. As a consequence, we could not use the calibration parameters previously calculated (see Par. 5.3) for E_{res} strips in displaying the 2D ΔE vs. E_{res} plots. Nevertheless, isotopes could still be identify and we could obtain their angular distributions anyway. In Figs. 5.35-5.40 we present the 2D correlation plots $\Delta E - E_{res}$. As we can see we can easily recognize the ^{7}Be, some ^{6}Li, ^{4}He, ^{3}He, some ^{2}H and a very well-defined curve coming from ^{1}H of which we can even observe the punch through the E_{res} stage. (see Fig. 5.41).

The leakage current of the telescope C detectors increased continuously throughout the experiment (0.03 μA with respect a maximum value of 0.02 μA for other telescope for the ΔE stage and 4.15 μA with respect a maximum value of 1.72 μA for other telescope for the E_{res} stage) thus worsening the energy resolution of both detector stages. However this was still sufficient to discriminate at least the atomic number of the detected particles, ^{7}Be in particular (Fig. 5.37).

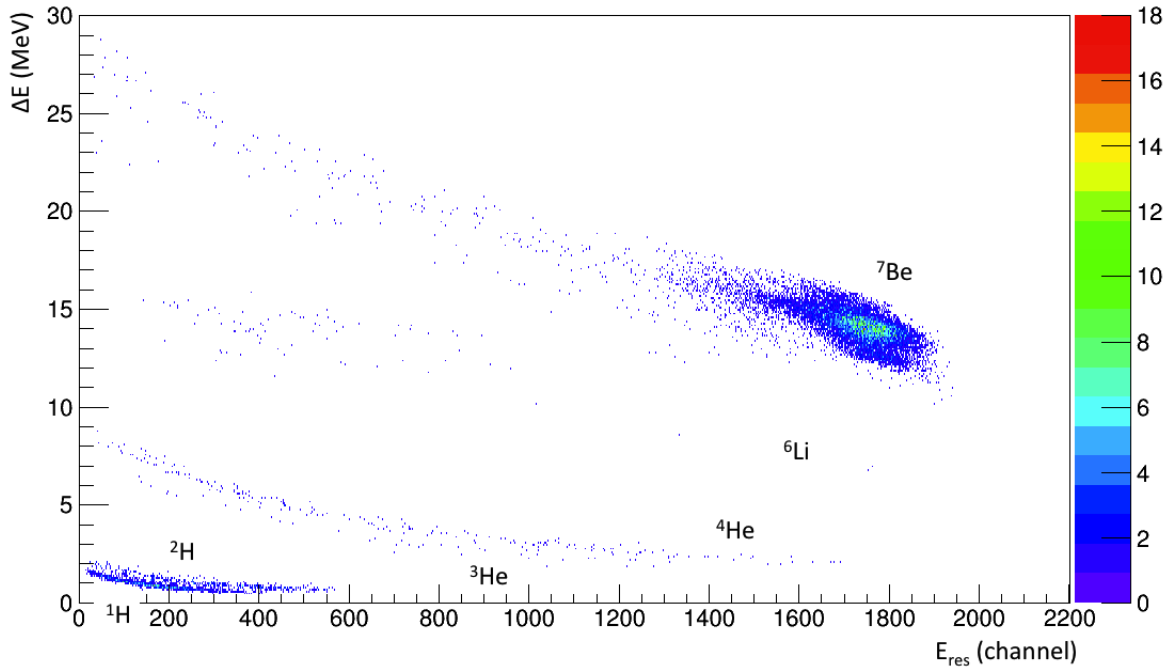

Figure 5.35: $\Delta E - E_{res}$ plot for telescope A.

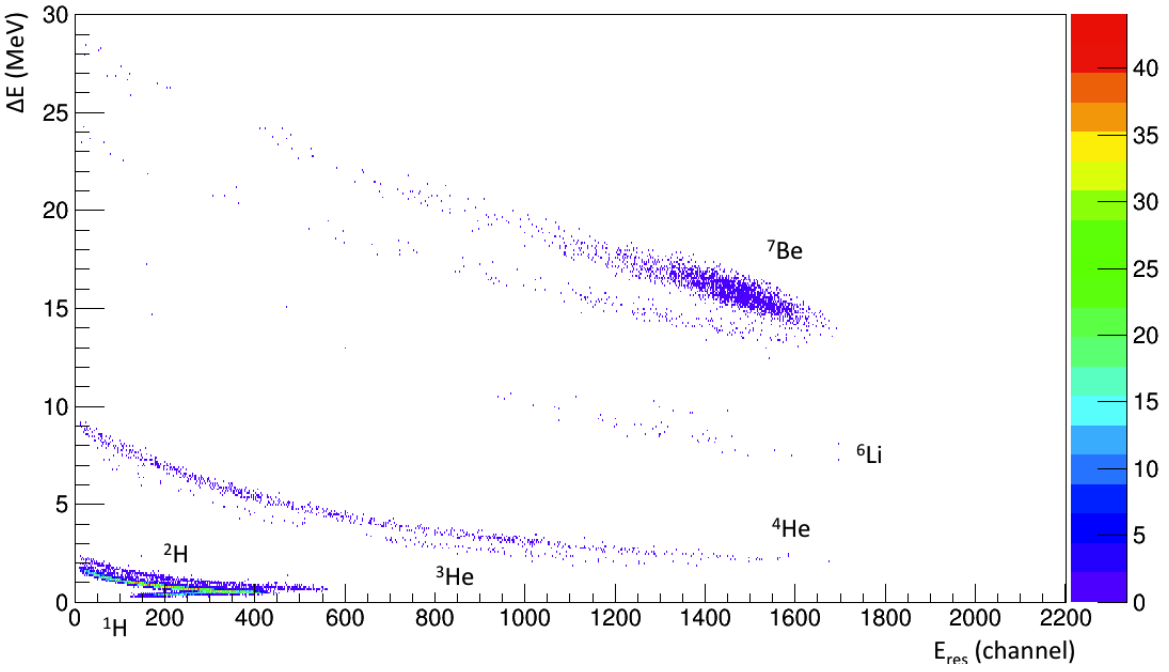

Figure 5.36: $\Delta E - E_{res}$ correlation plot for telescope B.

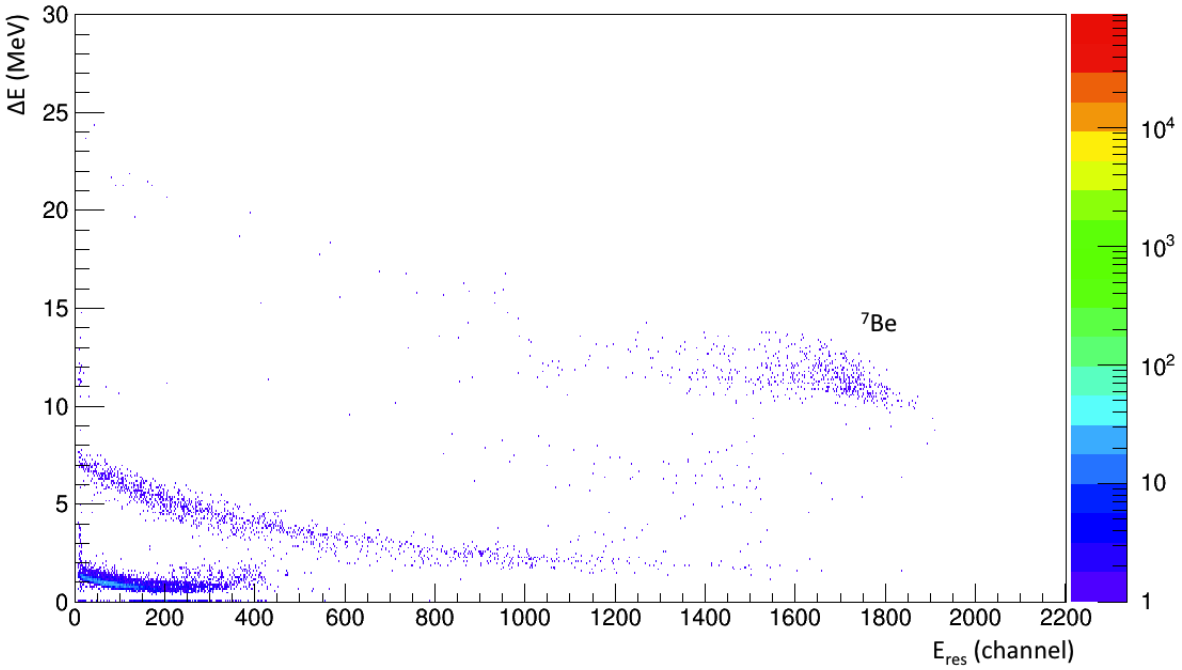

Figure 5.37: $\Delta E - E_{res}$ correlation plot for telescope C.

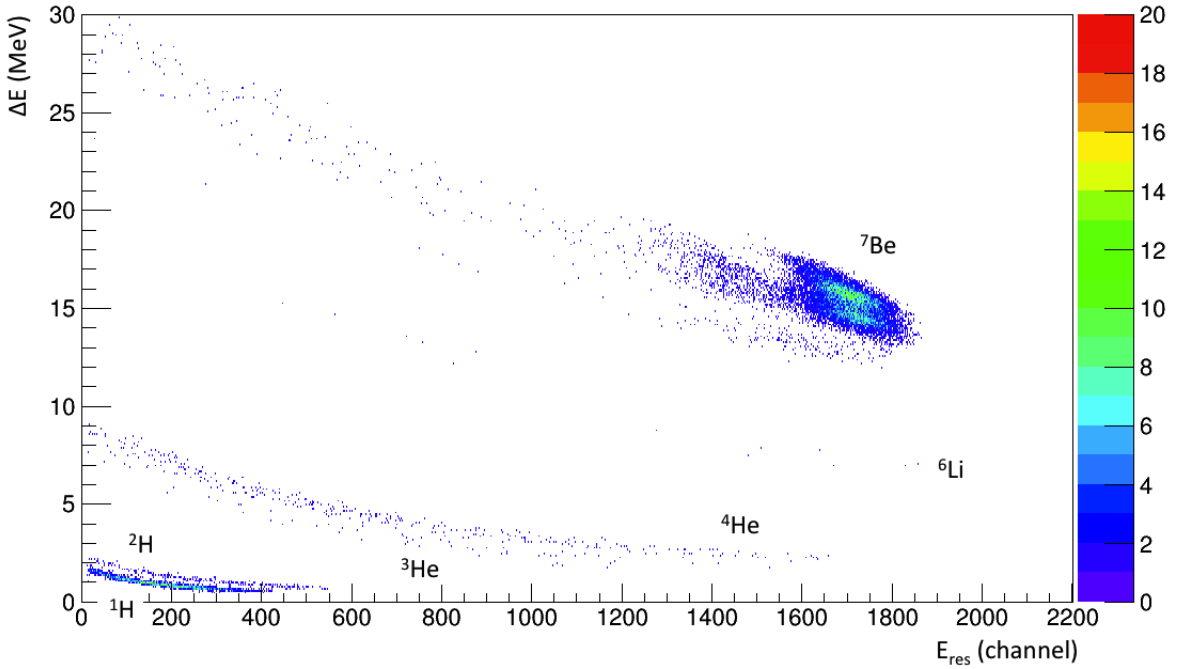

Figure 5.38: $\Delta E - E_{res}$ correlation plot for telescope D.

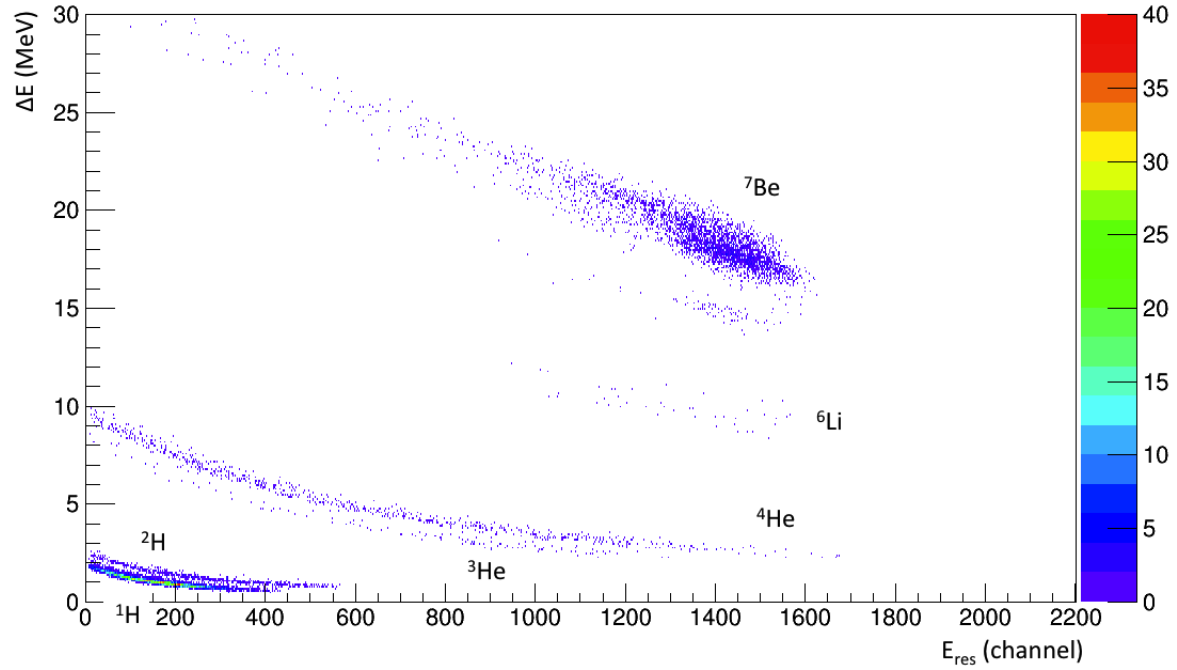

Figure 5.39: $\Delta E - E_{res}$ correlation plot for telescope E.

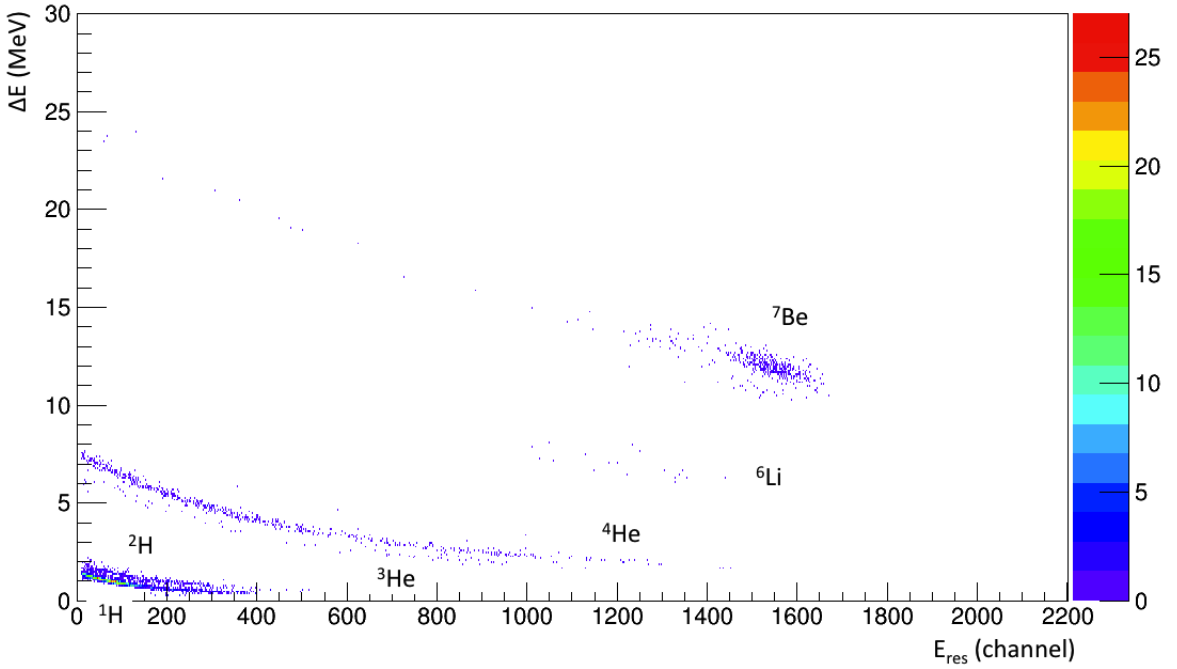

Figure 5.40: $\Delta E - E_{res}$ correlation plot for telescope F.

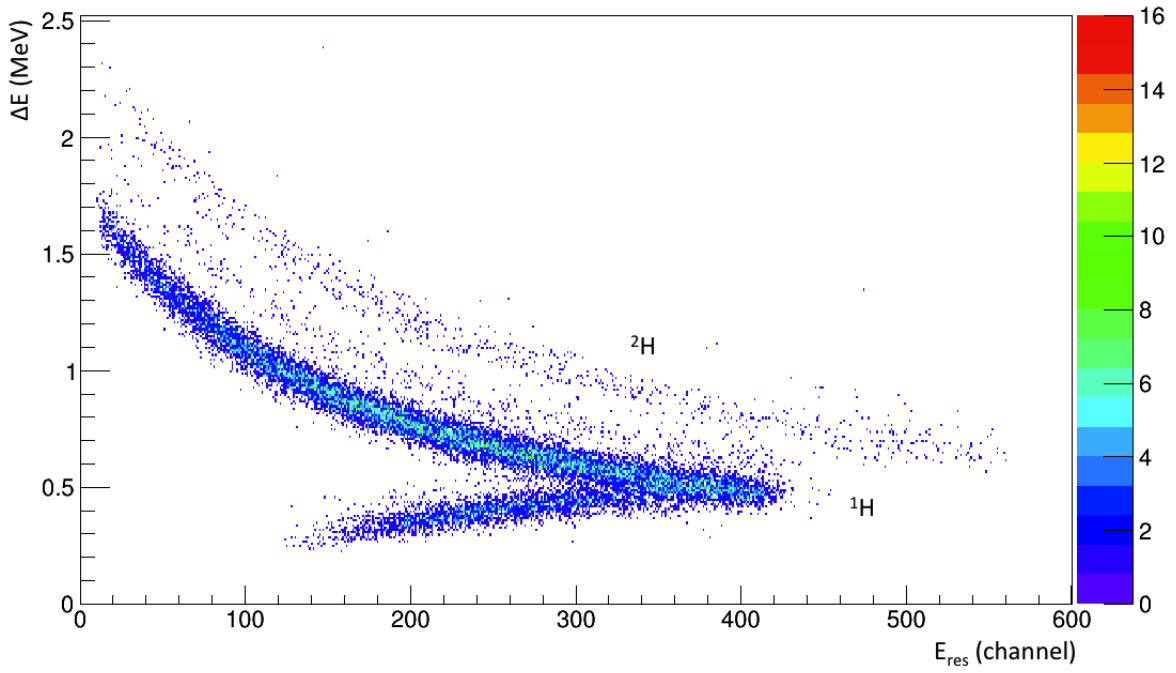

Figure 5.41: $\Delta E - E_{res}$ correlation plot for telescope B, zoomed at low energies. We can appreciate ^{1}H ions punching-through the E_{res}.

5.9.5 $\Delta E - E_{res}$ detection efficiency

Now we report the $\Delta E - E_{res}$ detection efficiency, i.e. the percentage of events that selected the different filters applied when we considered the E_{res} stage in the analysis with respect to the events that selected the different filters applied when we considered only the ΔE stage. Values are reported in Fig. 5.42. The mean efficiency is $\sim 0.8 - 0.9$ for all the telescopes, except for the C which had some problems in the E_{res} stage, as we already said; the error bars of the F strips are larger because of the lower statistics.

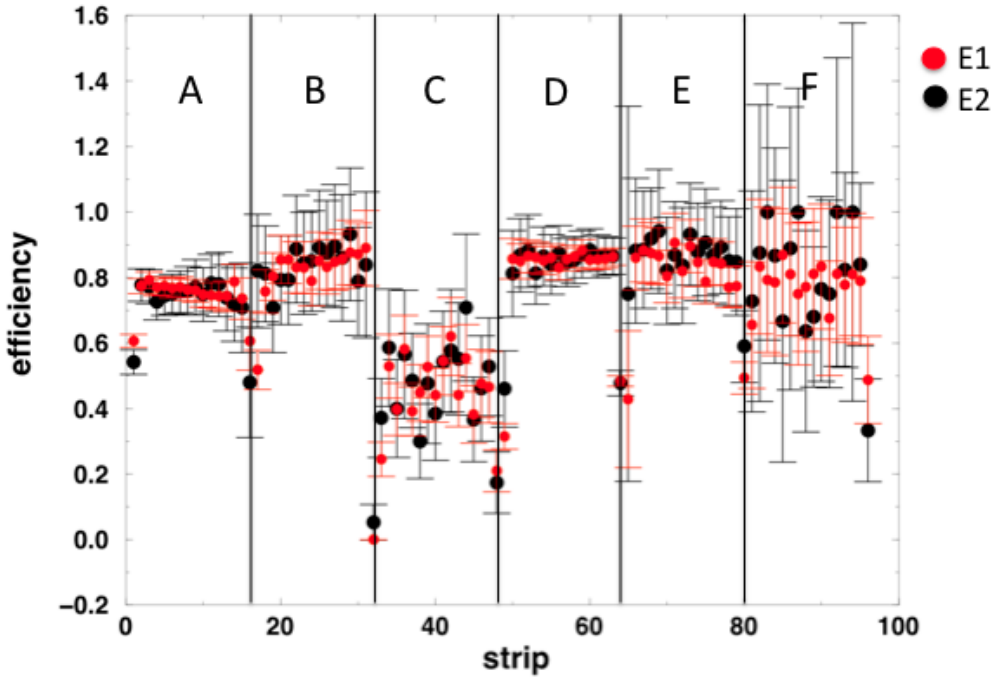

Figure 5.42: $\Delta E - E_{res}$ detection efficiency for x strips.

5.9.6 Angular distributions for ^{7}Be, ^{3}He, ^{4}He

Finally, we present the angular distributions obtained using the whole EXPADES array for ^{7}Be and the main reaction products ^{3}He and ^{4}He. For the moment we concentrated our study to these isotopes, the evaluation of the angular distributions for ^{6}Li, ^{1,2}H will be subject of a later analysis stage.

As in the previous similar plots, for each energy of the quasi-elastic scattering first we show (Figs. 5.43 and 5.46) the plot with all the 96 x strips at the various angles (in black those telescopes placed on the right side of the beam line and in red the telescopes placed on the left side), then, in order to eliminate the statistical fluctuations, consecutive strips were grouped together (Figs. 5.44 and 5.47) and finally we grouped together also the strips on the right and left sides. (Figs. 5.45 and 5.48). In these two passages we did not consider strips with counting statistics more than 3 standard deviations far from neighboring values.

In Figs. 5.49-5.54 we present the angular distributions for ^{3}He and ^{4}He for the two energies.

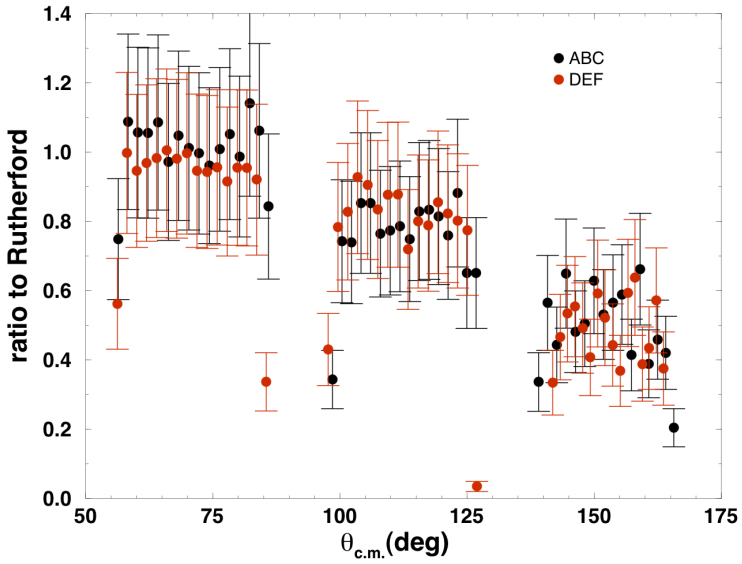

Figure 5.43: Angular distributions for ^{7}Be. Energy E_1.

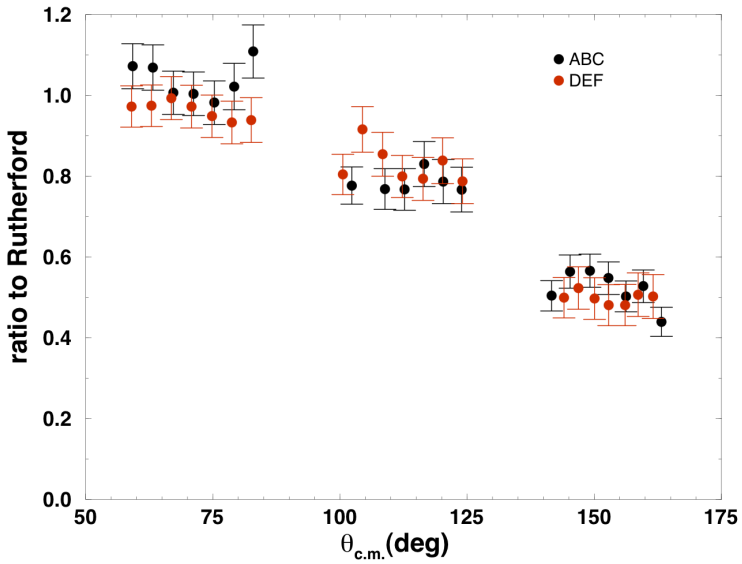

Figure 5.44: Angular distributions for ^{7}Be. Consecutive strips are grouped together. Energy E_1.

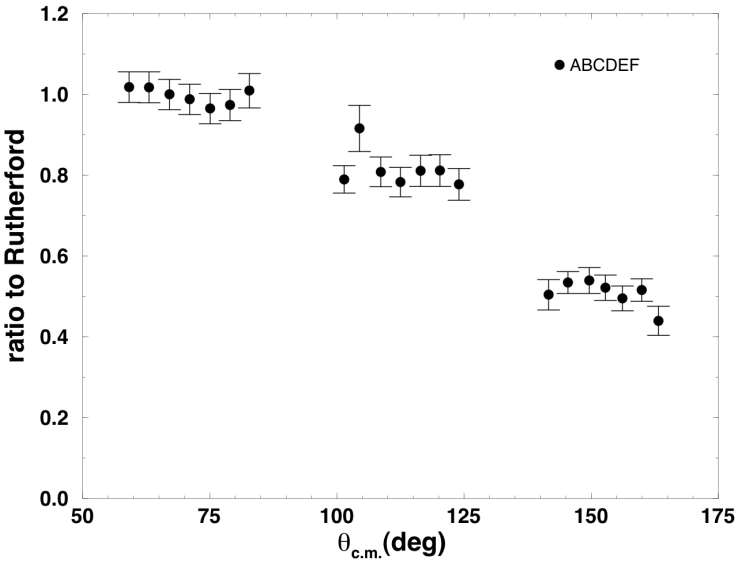

Figure 5.45: Angular distribution for ^{7}Be. Consecutive and opposed strips and grouped together. Energy E_1.

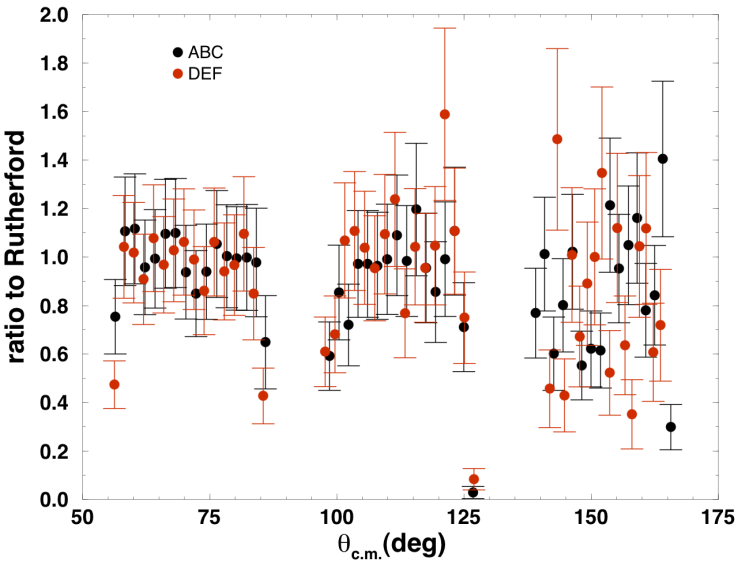

Figure 5.46: Angular distributions for ^{7}Be. Energy E_2.

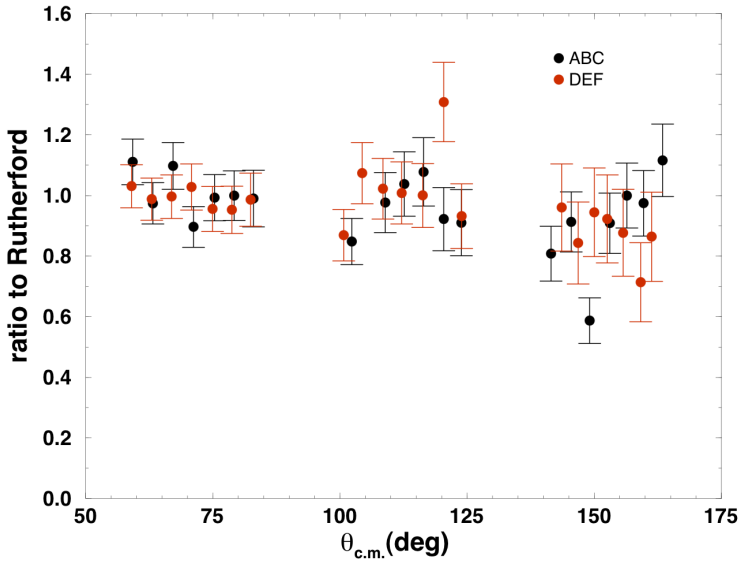

Figure 5.47: Angular distributions for ^{7}Be. Consecutive strips are grouped together. Energy E_2.

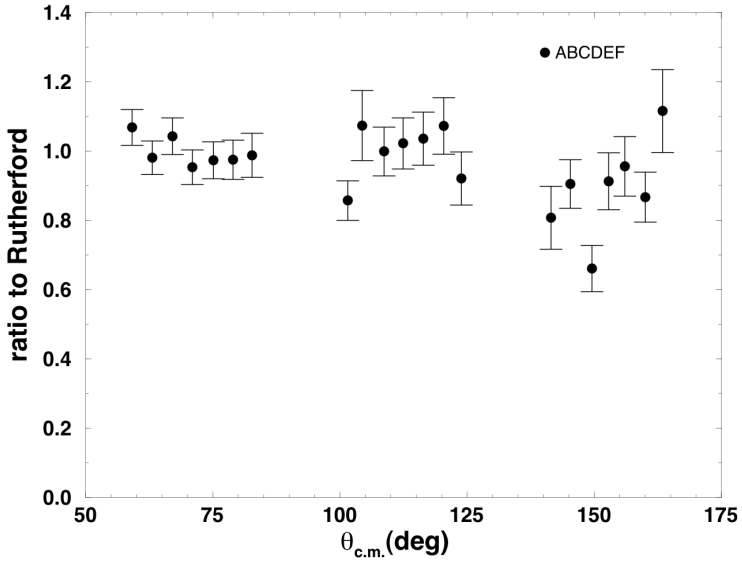

Figure 5.48: Angular distribution for ^{7}Be. Consecutive and opposed strips and grouped together. Energy E_2.

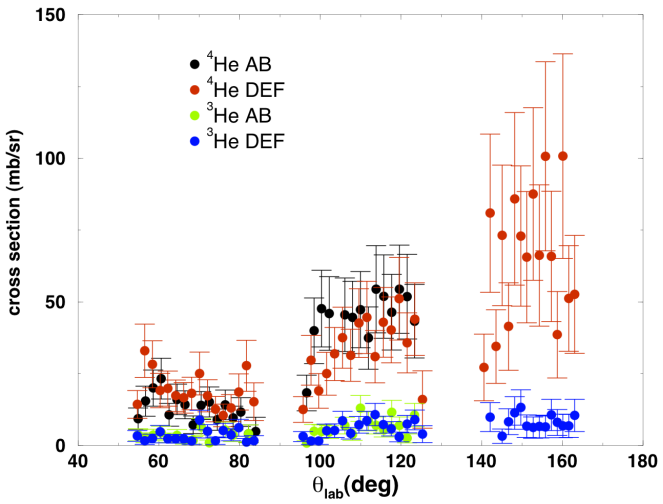

Figure 5.49: Angular distributions for ^{3}He and ^{4}He. Energy E_1.

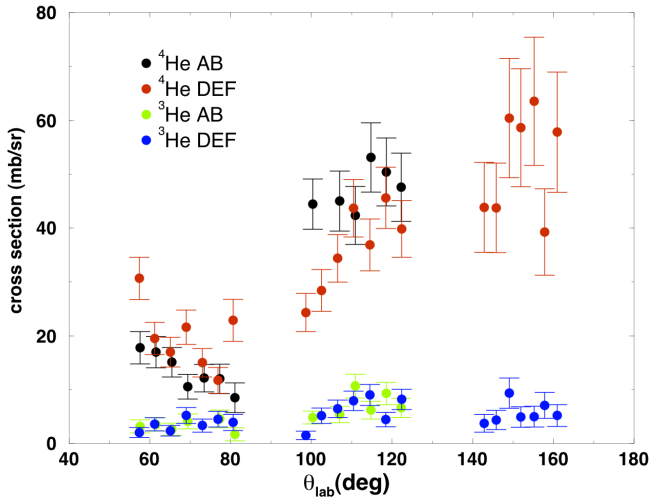

Figure 5.50: Angular distributions for ^{3}He and ^{4}He. Data of consecutive strips are grouped together. Energy E_1.

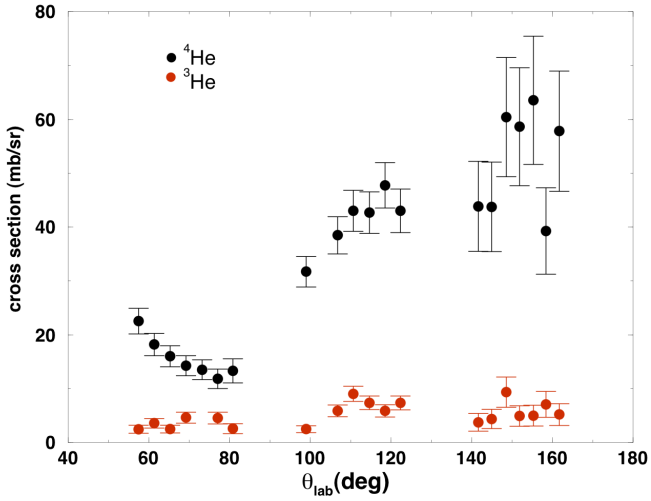

Figure 5.51: Angular distributions for ^{3}He and ^{4}He. Consecutive and opposed strips and grouped together. Energy E_1.

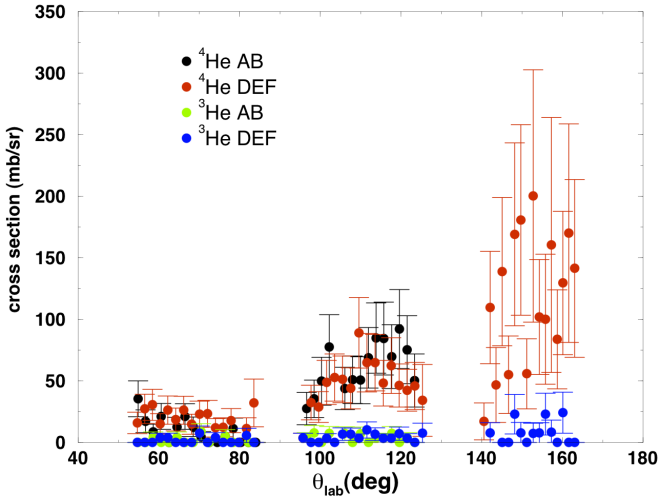

Figure 5.52: Angular distributions for ^{3}He and ^{4}He. Energy E_2.

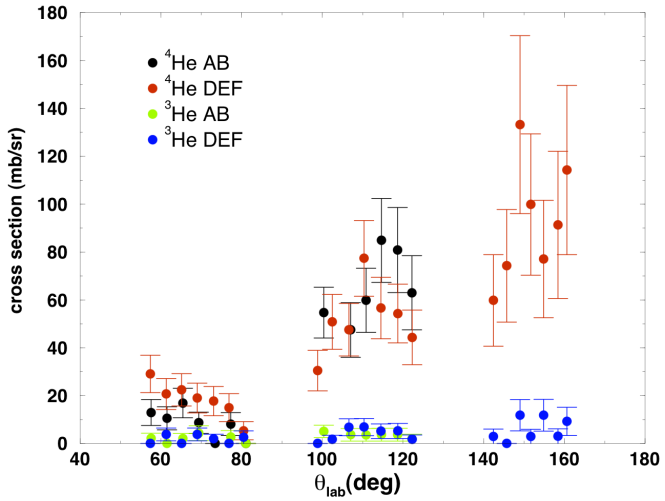

Figure 5.53: Angular distributions for ^{3}He and ^{4}He. Data of consecutive strips are grouped together. Energy E_2.

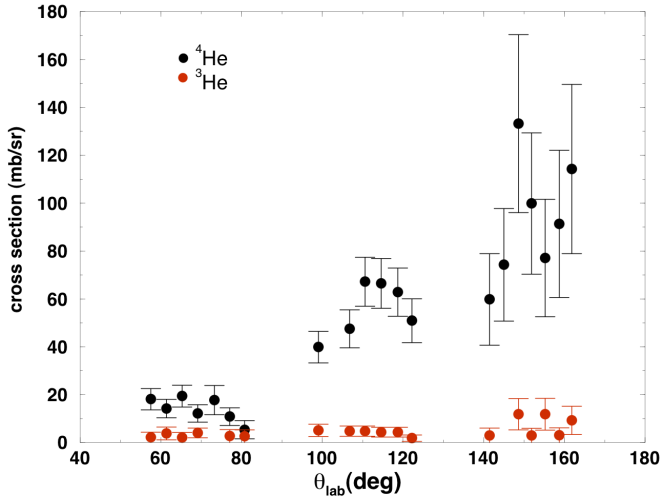

Figure 5.54: Angular distributions for ^{3}He and ^{4}He. Consecutive and opposed strips and grouped together. Energy E_2.

Chapter 6

Discussion

The scattering reaction of ^{7}Be nuclei from a ^{208}Pb target has been studied with the optical model, in order to obtain the reaction cross sections. The fitting procedure has been performed with the subroutines of the code FRESCO [31].

The nuclear interaction between the projectile and the target was described within the framework of the optical model with a Woods-Saxon well for both the real $V(r)$ and the imaginary part $W(r)$:

$$V(r) + iW(r) = -\left(\frac{V_0}{1 + e^{\left(\frac{r - r_{0v} A^{1/3}}{a_v}\right)}} + i \frac{W_0}{1 + e^{\left(\frac{r - r_{0w} A^{1/3}}{a_w}\right)}} \right) \tag{6.1}$$

Since we are dealing with peripheral reactions, we can not explore the inner part of the potential, i.e. the depth of the well, hence we have some ambiguities in the six parameters (V_0, r_{ov}, a_v, W_0, r_{0w}, a_w) of Eq. 6.1. As a starting point of the fitting procedure we followed the Broglia-Winther approach [35]. The depth of the real Woods-Saxon well is given by:

$$V_0 = 16\pi\gamma\bar{R}a_0 \tag{6.2}$$

where γ, $\bar{R}$ and the diffuseness a_0 are given by:

$$\bar{R} = \frac{R_P R_T}{R_P + R_T} \tag{6.3}$$

$$\gamma = \gamma_0 \left[1 - k \left(\frac{N_P - Z_P}{A_P} \right) \left(\frac{N_T - Z_T}{A_T} \right) \right] \tag{6.4}$$

$$a_0 = a_v = a_w = 0.63 \ fm \tag{6.5}$$

with $R_{P,T}$, $N_{P,T}$, $Z_{P,T}$ and $A_{P,T}$ being the radius, the neutron, the atomic and the mass number of the projectile and of the target, respectively, $\gamma_0 = 0.95 \ MeVfm^{-2}$ and $k = 1.8$. The radius parameter is given by:

$$r_0 = r_{w0} = r_{v0} = \frac{R_P + R_T + 0.29}{A_P^{1/3} + A_T^{1/3}} \tag{6.6}$$

Using the previous equations, we calculated, for the first energy E_1, the starting points for the potential parameters used in the optical model fit reported in Table 6.1.

When we used the FRESCO code, we left free all the parameters and we got the final values of the parameters reported in Table 6.2.

V_0	46.55 MeV
r_{v0}	1.183 fm
a_v	0.63 fm
W_0	46.55 MeV
r_{0w}	1.183 fm
a_w	0.63 fm

Table 6.1: Initial values of the potential parameters used in the optical model fit for the first energy.

V_0	71.24 MeV
r_0	1.15 fm
a_0	0.54 fm
W_0	23.69 MeV
r_w	1.06 fm
a_w	1.00 fm

Table 6.2: Final values of the potential parameters used in the optical model fit for the first energy.

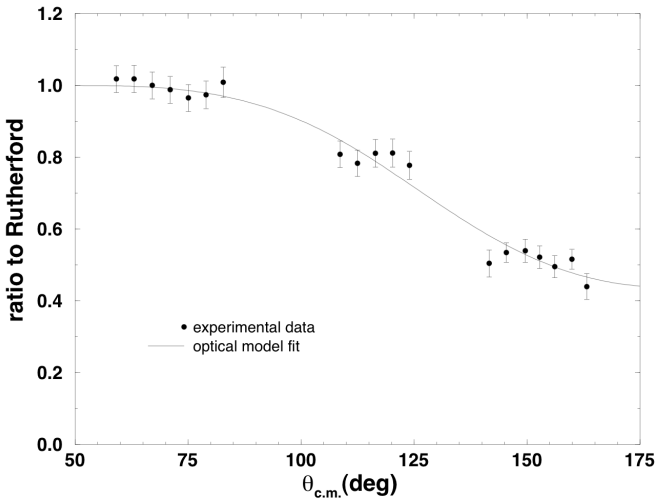

Figure 6.1: Experimental data and optical model fit obtained using the data the parameters of Table 6.2 for energy E_1. The 101° datum was excluded from the fit.

We obtained a reduced χ^2 of 0.813 and a reaction cross section $\sigma_R = 267.88\ mb$. The optical model fit is shown as a continuous line in Fig. 6.1.

For the second energy E_2, after some explorative trials we fixed all parameters with exception of $W(r)$ since we are dealing with the same system but a different energy, so at lower energy we can expect a shallower imaginary potential (see Table 6.3). Fig. 6.2 shows the fit obtained in this case.

We got a reduced χ^2 of 1.176 and $\sigma_R = 77.97\ mb$.

V_0	71.24 MeV
r_0	1.15 fm
a_0	0.54 fm
W_0	14.87 MeV
r_w	1.06 fm
a_w	1.00 fm

Table 6.3: Final values of the potential parameters used in the optical model fit for the second energy.

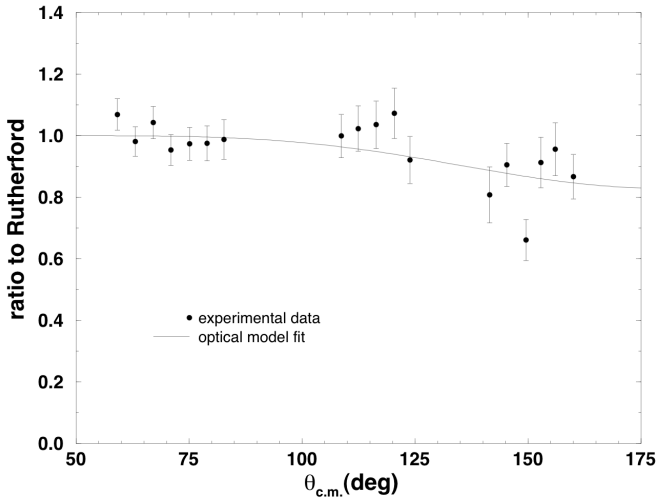

Figure 6.2: Experimental data and optical model fit obtained using the data the parameters of Table 6.3 for energy E_2. The 101° and 165° data were excluded from the fit.

Finally, we compared our data with two similar systems: ^{6}Li+^{208}Pb and ^{7}Li+^{208}Pb [34]. Table 6.4 reports the reaction cross sections for the different energies, the reduced energies E_{red} and the reduced cross sections σ_{red}. The latter two values are plotted in Fig. 6.3 and are obtained as [32]:

$$E_{red} = \frac{E}{\frac{Z_P Z_T}{A_P^{1/3} + A_T^{1/3}}} \tag{6.7}$$

$$\sigma_{red} = \frac{\sigma_R}{(A_P^{1/3} + A_T^{1/3})^2} \tag{6.8}$$

and these expression provide the best way to compare different systems, so that geometrical effects are removed and Coulomb barriers are normalized.

As we can see from Fig. 6.3, our data lie on the same line of that of the system ^{7}Li+^{208}Pb and the reason is that ^{7}Be and ^{7}Li are mirror nuclei, so we might except a similar behavior. In Fig. 6.4 (taken from [33]) we report a comparison with other systems for the same projectiles interacting with a ^{27}Al target. In the same range of reduced energy of our data ($0.9 - 1.0\ MeV$) we observe a similar pattern,

$E\ (MeV)$	$\sigma_R\ (mb)$	$E_{red}\ (MeV)$	$\sigma_{red}\ (mb)$
^{7}Be+^{208}Pb			
40.65	267.88	0.97	4.75
37.55	77.97	0.90	1.38
^{6}Li+^{208}Pb			
29	228	0.91	4.04
31	431	0.98	7.64
33	666	1.04	11.80
35	897	1.10	15.89
39	1303	1.23	23.09
^{7}Li+^{208}Pb			
29	138	0.92	2.45
31	327	0.99	5.79
33	572	1.05	10.14
35	787	1.12	13.94
39	1242	1.24	22.01

Table 6.4: Reaction cross sections for different energies of the systems ^{7}Be+^{208}Pb, ^{6}Li+^{208}Pb, ^{7}Li+^{208}Pb [34] and the corresponding reduced values.

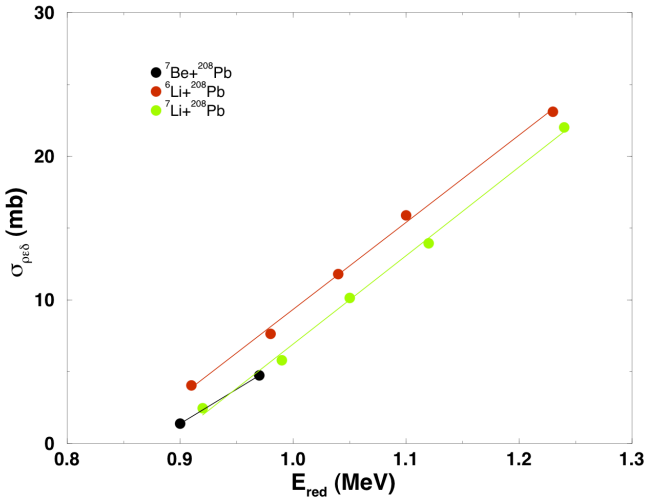

Figure 6.3: Reduced reaction cross section σ_{red} as a function of the reduced energy E_{red} for the systems ^{7}Be+^{208}Pb, ^{6}Li+^{208}Pb, ^{7}Li+^{208}Pb.

i.e. the curves referring to ^{7}Be and ^{7}Li are nearly coincident. But at higher energies we observe a change in the slopes, and the authors of [33] concluded that the total reaction cross section increases for weakly bound nuclei because for them we have a more dominant role of the breakup and transfer channels at above-barrier energies.

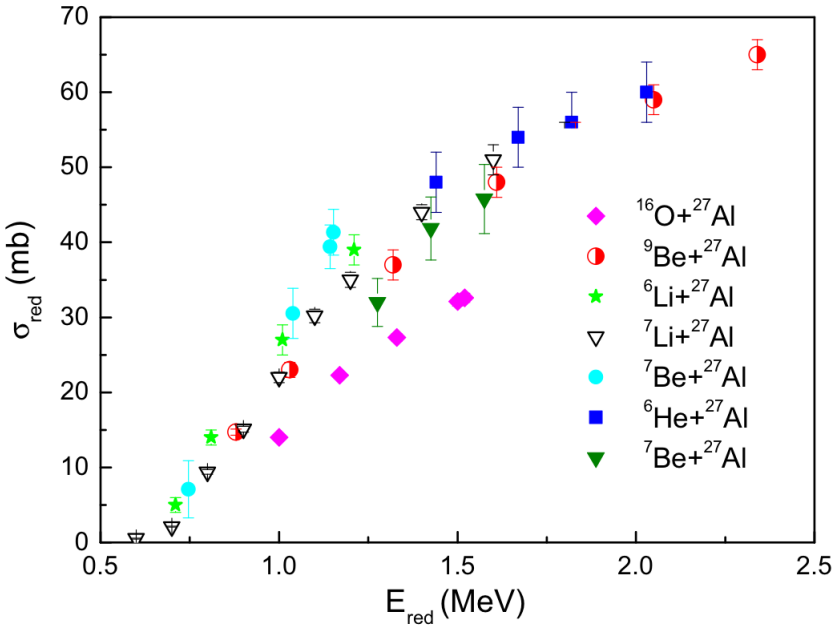

Figure 6.4: Reduced total reaction cross sections for several projectiles and the same ^{27}Al target. Figure taken from [33].

Chapter 7

Conclusions

In this thesis work we analyzed the system ^{7}Be+^{208}Pb at two energies around the Coulomb barrier. The reaction was performed with the EXOTIC facility at INFN-LNL and the ejectiles were detected by the EXPADES array.

Despite the lack of a calibration for the E_{res} stage, we identified the ^{7}Be and ^{3,4}He reaction products in the angular range $55° - 165°$ by means of the ΔE-E_{res} technique.

We evaluated the angular distributions for the quasi-elastically scattered particles at the energies $E_1 = 40.65\ MeV$ and $E_2 = 37.55\ MeV$ and we got the best-fit potential parameters within the optical model framework, that permitted us to extract the reaction cross sections: 267.88 m and 77.97 mb respectively. These values were compared to those measured of the systems ^{6}Li+^{208}Pb and ^{7}Li+^{208}Pb at similar energies and we observed a similitude of behavior between the mirror nuclei ^{7}Li and ^{7}Be as projectiles.

Further investigations are needed to establish whether the ^{7}Be total reaction cross section enhancement (with respect to the mirror nucleus ^{7}Li) observed at above-barrier energies for the interaction with a ^{27}Al target is present also for a ^{208}Pb, where we expect that the Coulomb field plays a more relevant role. Concerning ^{3,4}He, their angular distribution exhibit strong similarities to those observed for light charged particles emitted in coincidence with fission fragments for the systems ^{7,9}Be, ^{7}Li+^{238}U [25].

Finally, a future analysis of multiplicity 2 events, i.e. the coincidence of two particles, that despite their very limited number (less than tha 0.5% of the data) may contain very interesting information concerning the breakup process: $^{7}\text{Be} \rightarrow {}^{3}\text{He} + {}^{4}\text{He}$.

Bibliography

[1] E. Strano *et al.*, Nucl. Instrum. Methods Phys. Res. B **317**, 657 (2013).

[2] F. Farinon *et al.*, Nucl. Instrum. Methods Phys. Res. B **266**, 4097 (2008).

[3] G. F. Knoll, *Radiation Detection and Measurement*, John Wiley & Sons Inc, 2010.

[4] K. Krane, *Introductory Nuclear Physics*, John Wiley & Sons Inc, 1987.

[5] *The Euroschool Lectures on Physics with Exotic Beams, Vol. I*, J. Al-Khalili and E. Roeckl eds., Springer, 2004.

[6] M. Mazzocco *et al.*, Phys. Rev. C **82**, 054604 (2010).

[7] https://root.cern.ch/.

[8] lise.nscl.msu.edu/topics.html.

[9] D. M. Brink, Phys. Lett. B **40**, 37 (1972).

[10] M. Mazzocco *et al.*, Acta Phys. Pol. B **45**, 2 (2014).

[11] J.F. Liang and C. Signorini, Int. J. Mod. Phys. E **14**, 1121 (2005).

[12] L.F. Canto, P.R.S. Gomes, R. Donangelo and M.S. Hussein, Phys. Rep. **424**, 1 (2006).

[13] N. Keeley *et al.*, Prog. Part. Nucl. Phys. **59**, 579 (2007).

[14] M. Mazzocco, Int. J. Mod. Phys. E **19**, 977 (2010).

[15] J.P. Bychowski *et al.*, Phys. Lett. B **596**, 26 (2004).

[16] P.A. De Young *et al.*, Phys. Rev. C **71**, 051601(R) (2005).

[17] J.J. Kolata *et al.*, Phys. Rev C **75**, 031302(R) (2007).

[18] A. Navin *et al.*, Phys. Rev. C **70**, 044601 (2004).

[19] A. Chatterjee *et al.*, Phys. Rev. Lett. **101**, 032701 (2008).

[20] A. Lemasson *et al.*, Phys. Rev. Lett. **103**, 232701 (2009).

[21] E. Aguilera *et al.*, Phys. Rev. C **79**, 021601(R) (2009).

[22] E. Aguilera *et al.*, Phys. Rev. Lett. **107**, 092701 (2011).

[23] A. Di Pietro *et al.*, Phys. Rev. Lett. **105**, 022701 (2010).

[24] A. Di Pietro *et al.*, Phys. Rev. C **85**, 054607 (2012).

[25] R. Raabe *et al.*, Phys. Rev. C **74**, 044606 (2006).

[26] R.N. Sagaidak, A.V. Yeremin, Nucl. Instr. and Meth. B **93**, 103 (1994).

[27] http://www.micronsemiconductor.co.uk/pdf/cat.pdf.

[28] The XDAQ framework, http://www.cern.ch/xdaq-

[29] Run Control and Monitoring System, http://cmsdoc.cern.ch/cms/TRIDAS/RCMS/.

[30] J. Grebosz, Comp. Phys. Comm. **176**, 251 (2007).

[31] I.J. Thompson, Comput. Phys. Rep. **2**, 167 (1988).

[32] P.R.S. Gomes *et al.*, Phys. Rev. Lett. C **71**, 017601 (2005).

[33] V. Morcelle *et al.*, Phys. Rev. C **89**, 044611 (2014).

[34] N. Keeley *et al.*, Nucl. Phys. A **571**, 326 (1994).

[35] R.A. Broglia and A. Winther, *Heavy Ion Reactiosn*, vol. I., Addison-Wesley Publishing Company, Redwood City (1991).

List of Figures

List of Tables

Acknowledgments

In this section I would like to thank all the people that have supported me during these years and for simplicity's sake I will now switch to my mother language.

Per questo lavoro di tesi in particolare il mio primo ringraziamento va al mio relatore, Marco, per la guida precisa e costante durante questi mesi. Estendo poi il mio grazie al resto del gruppo di ricerca: Emanuele, per il prezioso aiuto nella programmazione; Tina, Ciro e Alfonso, per i piacevoli momenti passati a LNL; Jenny, per gli utili commenti e le spiegazioni sul funzionamento dei PPAC.

Per tutti questi anni universitari invece vorrei ringraziare innanzitutto la mia famiglia per l'appoggio, la pazienza e l'aiuto nei momenti di difficoltà.

Impossibile non ringraziare Ivan, Michele ed Elia per le divertentissime serate e le indimenticabili & lunghissime & improbabili discussioni su tutti i film e telefilm di fantascienza dal 1902 ad oggi!

Poi, in ordine sparso, ringrazio tantissimo gli staff di "Sperimentando" e del Museo di Storia della Fisica di Padova, per avermi accolto in un ambiente fantastico aprendomi alla possibilità di raccontare con passione e scioltezza ciò che ho imparato negli anni; Massimo, per i momenti di studio & corsa insieme; Angelo e lo staff di "meteoblue" per la bellissima esperienza di stage; il gruppo dell'ex-gabbiotto: Monica, Cecilia, Alberto, Checco, Dario, Carlo, Claudio, Tommaso; gli indimenticabili compagni di corso: Andrea, Francesca, Elena, Stefano, Andrea, Alma; Francesco, per avermi iniziato all'uso di R; il comitato scientifico di Meteonetwork; il mitico corso del *miglior laboratorio di sempre* a LNL: Marco, Michele, Giorgia; i *brombe*: Marco (bis), Elisa, Fabio, Matteo, Anna, Andrea Lupo, Andrea T8, Zaza, Cipe, Ulisse che hanno reso *bellissimi* e indimenticabili gli ultimi mesi.

Menzioni d'onore, i "dove":

- Pesaro, Treviso, Cencenighe Agordino, Teolo, Basilea
- il Nerocaffè, la pasticceria Alberini
- il collegio Don Bosco
- il Giselle
- INFN-LNL
- i tavoli dell'aula C e del Galivm
- il Cinecity
- il Monte san Bartolo
- il Montello

- il Club Casa di Caccia
- lo Shanghai
- il Re di Mezzo

i “chi”:

- Gene Roddenberry
- Luca Mercalli
- Robert Zemeckis, Michael J. Fox e Christopher Lloyd
- 883, Michael Jackson, U2, Freddie Mercury
- Chuck Jones
- Stephen Hawking
- Gioacchino Rossini

i “cosa”:

- la meteorologia
- Apple Inc.
- Star Trek e la birra romulana
- il latte con miele e cannella
- l’IKEA
- R
- il prix
- eBay e amazon

We all change. When you think about it,
we are all different people, all through our lives
and that’s okay, that’s good! You’ve gotta keep moving,
so long as you remember all the people that you used to be.

The Doctor